Modelling planet formation

— from dust to gas giant

Tommy Chi Ho Lau

SIGILL. UNIVERSITAT. LUDOVIC. MAXIM.

München 2024

Modelling planet formation

— from dust to gas giant

Tommy Chi Ho Lau

Dissertation
der Fakultät für Physik
der Ludwig-Maximilians-Universität
München

vorgelegt von
Tommy Chi Ho Lau
aus Hongkong

München, den 11. Oktober, 2024

Erstgutachter: Prof. Dr. Til Birnstiel
Zweitgutachter: Prof. Dr. Barbara Ercolano
Tag der mündlichen Prüfung: 26. November, 2024

Zusammenfassung

Planeten bilden sich aus interstellaren Staubteilchen von Submikrometer Größen bis hin zu Tausenden von Kilometern großen Gasriesen, die sich über zwölf Größenordnungen erstrecken. Der vorherrschende theoretische Weg beginnt mit der Koagulation von mikrometergroßem interstellarem Staub zu Kiesel. Die Streaming Instability kann dann dichte Filamente erzeugen und der anschließende Gravitationskollaps bildet Planetesimale. Da die Planetesimale gravitativ mit den Kiesel in der protoplanetare Scheibe interagieren, wachsen sie durch die Kiesel-Akkretion zu Planetenkernen, die schließlich Gas akkretieren und zu Gasriesen anwachsen. Obwohl jeder Schritt der Planetenentstehung im Detail untersucht wurde, bleiben viele Herausforderungen bestehen, wenn es darum geht, diese Schritte zu einem Modell der Entstehung des Sonnensystems oder der vielfältigen Population von Exoplanetensystemen zusammenzufügen. Diese Arbeit präsentiert die Entwicklung von Planetenbildungsmodellen, die die Scheibenentwicklung mit der N-Körper-Gravitation kombinieren, einschließlich der oben genannten Entstehungsprozesse in verschiedenen Stadien. Zunächst zeigt ein glattes Scheibenmodell mit anfänglichen Planetesimalen, dass Planetenkerne eine signifikante Migration nach innen erfahren werden, die die Entstehung von Riesenplaneten wie im Sonnensystem verhindert. Dieses Modell ging nicht auf das Problem ein, dass der Staub in der Scheibe möglicherweise nicht derart konzentriert ist, dass er das durch die Streaming Instability vorgegebene Kriterium zur Bildung von Planetesimalen erfüllt. Motiviert durch die jüngsten Beobachtungen von Staubringen in protoplanetaren Scheiben wird ein vollständiger Scheibenmodell einschließlich der Staubentwicklung entwickelt und eine anfängliche Scheibenunterstruktur festgelegt. In diesem Fall wird die Bildung von Planetesimalen durch das Modell erfasst, wobei der Staubring die erforderliche Voraussetzung für die Streaming Instability bietet. Das anschließende Wachstum durch Kiesel-Akkretion ist dank der erhöhten Staubdichte ebenfalls effizient. Das Migrationsproblem wird verhindert und Planetenkerne bleiben in der Nähe des durch die Scheibenunterstruktur verursachten Druckanhäufung. Am äußeren Rand der Lücke, die durch einen vollständig ausgebildeten Gasriesen geöffnet wird, wird eine ähnliche Umgebung reproduziert, die die Entstehung der nächsten Planetengeneration einleiten kann und somit ein Szenario der sequenziellen Planetenentstehung darstellt. Schließlich wird die Scheibenauflösung durch interne Photoevaporation in das Modell aufgenommen. Die vorläufigen Ergebnisse zeigen einen Weg zur Bildung kleiner Körper des Sonnensystems, wie sie im Kuiper Belt zu finden sind, während der Endphase der Scheibe. Zukünftige Erweiterungen des Modells werden ebenfalls am Ende dieser Arbeit diskutiert.

Abstract

Planets form from interstellar grains of sub-micron to gas giants of thousands of kilometres, which span over 12 orders of magnitude in size. The prevailing theoretical pathway starts from coagulation of micron-sized interstellar dust to form pebbles. The streaming instability can then induce dense filaments and the subsequent gravitational collapse forms planetesimals. As the planetesimals interact gravitationally with the pebbles in the planetary disc, pebble accretion grows them to form planetary cores, which finally accrete gas to form gas giants. Although each step of planet formation has been studied extensively, many challenges remain in assembling them to model the formation of the Solar System or the diverse population of exoplanetary systems. This thesis presents the development of planet formation models that combined disc evolution with the *N*-body gravity including the above formation processes at various stages. First, a smooth disc model with initial planetesimals shows that planetary cores shall experience significant inwards migration that prevent the formation of Solar-System like giant planets. And, this model did not address the problem that dust in the disc may not be concentrated to fulfil the criterion imposed by the streaming instability to form planetesimals. Motivated by the recent observations of dust rings in protoplanetary discs, a more complete disc model including dust evolution is adopted and an initial disc substructure is imposed. In this case, the formation of planetesimals is captured by the model, where the dust ring provides the required condition for the streaming instability. Subsequent growth by pebble accretion is also efficient thanks to the enhanced dust density. The migration problem is prevented and planetary cores remain near the pressure bump induced by the disc substructure. At the outer edge of the gap opened by a fully formed gas giants, similar environment is reproduced, which can induce the formation of the next generation of planet, demonstrating a scenario of sequential planet formation. Finally, the disc dispersal by internal photoevaporation is incorporated to the model. The preliminary results show a pathway to form solar system small bodies during the final stage of the disc. Future extensions of the model are discussed as well at the end of this thesis.

天之蒼蒼，其正色邪？其遠而無所至極邪？

《莊子·逍遙遊》（戰國）

Is its azure the proper colour of the sky? Or is it occasioned by its distance and illimitable extent?

Chuang Tzu: Enjoyment in Untroubled Ease, 350 BC–250 BC
Translation: *The Writings of Chuang Tzu*, James Legge, 1891

Contents

Chapter 1

Introduction

Since antiquity, continuous attempts have been made to explain the origin of the Solar System and its evolution. While the earliest theories typically have religious and philosophical roots, they marked the start of the understanding about our cosmic neighbourhood. Following the scientific revolution in the early modern period, Kant published ‘Universal Natural History and Theory of the Heavens’ in 1755. He proposed a general picture that stars and planets are formed in rotating and collapsing gaseous clouds, which is known the nebular hypothesis. Laplace, in 1796, elaborated further on this hypothesis by considering angular momentum conservation. In his model, the nebula begins as a rotating spherical cloud, which then collapses and flattens along the spin axis into a disc. Centuries later in 1969, Safronov published ‘Evolution of the Protoplanetary Cloud and Formation of the Earth and the Planets’, where he described the major processes, marked the broth of the modern planet formation theory.

The next chapter (Chapter 2) reviews the prevailing understanding of planet formation, which leads to the open questions that motivated this thesis. It is followed by three published works that attempted to build a planet formation model by combining these processes (Chapter 3 to 5), which are arranged logically. Afterwards, Chapter 6 presents the on-going work on the final stages of planet formation. Finally, Chapter 7 summarizes these works and presents an outlook on possible pathways for further progress in modelling planet formation.

Chapter 2

Theoretical Background

From the observations of extinction caused by the interstellar medium, Mathis et al. (1977) found a good fit of the particle size distribution, commonly known as the 'MRN distribution', where the maximum size is about 1 μm. Meanwhile, the radius of Jupiter is about 7×10^7 m. This implies that planet formation spans over 13 orders of magnitude in length, which can be divided into multiple stages. First, the next section introduces the current understanding of protoplanetary disc, the birth place of planets. Then, the subsequent sections present the current theories in each of the stages of planet formation respectively.

2.1 Protoplanetary disc

2.1.1 Young stellar objects

Well before protoplanetary discs were observationally resolved, the observations of the cores in molecular cloud are consistent with the existence of accreting discs around young stars. From the spectral energy distributions, the infra-red excess on top of the stars' blackbody radiation suggests heated dust near the star in the disc, while the ultra-violet excess indicates high-temperature regions on the stellar surface suggesting accretion. Lada & Wilking (1984) surveyed the ρ Ophiuchi dark cloud and grouped them into three classes of young stellar objects based on the slopes of the spectral energy distribution, or spectral indices, in the infra-red wavelengths, which can be defined as

$$\alpha_{\mathrm{IR}} \equiv \frac{\mathrm{d}\log(\lambda F_\lambda)}{\mathrm{d}\log\lambda} \tag{2.1}$$

for a wavelength λ between 10 and 1 μm, and F_λ is the flux per unit wavelength. The three classes include: Class 0, in which there is no flux in the near infra-red wavelengths and the distribution is effectively a reddened blackbody; Class I, in which α_{IR} is positive to zero; and, Class II: in which α_{IR} is negative and the classical T Tauri stars belongs to this class.

Adams et al. (1987) further interpreted this as a theoretical evolution sequence. As a cloud begins to collapse, the star and the protoplanetary disc are well embedded in a dust envelope with continuous infalls. The flux from the star cannot be observed directly and is reprocessed through heating of the dust in the cloud, which results in the observed spectral energy distributions for the Class 0 objects. As infall terminates due to stellar wind, the star becomes more apparent while the disc remains, which observationally evolves to a Class I object and then to a Class II one. Class III can be further defined for young stellar objects with little to no infra-red excess, which indicates the depletion of the disc.

The prevailing planet formation theories, as present in the following, typically starts with the Class II stage, where the protoplanetary disc is generally isolated from infalls. Nonetheless, there are suggestions that planet formation may begin also in the Class I stage while a consensus has yet been established.

2.1.2 Structure

The structure of the protoplanetary disc is crucial to planet formation. The following, the key physical features are reviewed.

Vertical structure

Let us consider a protoplanetary disc that have the mass $M_{\rm disc}$ which is much smaller than the stellar mass M_*. The disc is also symmetric about the midplane and thin, where the height above the midplane z is much smaller than the distance from the star r. Considering vertical hydrostatic equilibrium, the pressure gradient with respect to z is

$$\frac{\mathrm{d}P}{\mathrm{d}z} = -\rho_{\rm g} g_z, \tag{2.2}$$

where the gas density at z is $\rho_{\rm g}$. And, g_z is the vertical component of gravity at z, which is

$$g_z = \frac{GM_*}{(r^2+z^2)^{3/2}} z \approx \Omega_{\rm K}^2 z, \tag{2.3}$$

with the gravitational constant G and the Keplerian orbital frequency $\Omega_{\rm K} = \sqrt{GM_*/r^3}$. If we further assume that the gas is ideal and is vertically isothermal, we can apply the equation of state

$$P = \rho_{\rm g} c_{\rm s}^2 \tag{2.4}$$

with the speed of sound $c_{\rm s}$. Eliminating P in Eq. (2.2) yields the solution

$$\rho_{\rm g} = \rho_0 e^{-z^2/2H_{\rm g}^2}$$

with the vertical scale height

$$H_{\rm g} \equiv \frac{c_{\rm s}}{\Omega_{\rm K}}. \tag{2.5}$$

The gas density at midplane ρ_0 can also be expressed as

$$\rho_0 = \frac{1}{\sqrt{2\pi}} \frac{\Sigma_{\rm g}}{H_{\rm g}} \tag{2.6}$$

with the vertically integrated gas surface density Σ_g. From the definition of H_g, we can further express the aspect ratio, or the reduced scale height, as

$$\hat{h}_\mathrm{g} \equiv \frac{H_\mathrm{g}}{r} = \frac{c_\mathrm{s}}{v_\mathrm{K}} \tag{2.7}$$

with the local Keplerian velocity $v_\mathrm{K} = r\Omega_\mathrm{K}$. If the radial disc temperature profile is parameterized by $T \propto r^{-q_T}$, and $c_\mathrm{s} \propto T^{1/2}$ for ideal gas, then

$$\hat{h}_\mathrm{g} \propto r^{(1-q_T)/2}. \tag{2.8}$$

Therefore, for $q_T < 1$, the disc is flared, which is also the typical case as shown below on the temperature profile.

Temperature profile

Although it is oversimplifying, let us first assume that stellar irradiation dominates heating of the disc, which is also called a passive disc. For r much larger than the stellar radius R_*, it is also valid to assume that the star is a point source of radiation. Without a disc, the stellar flux at r is

$$F_* = \frac{L_*}{4\pi r^2}, \tag{2.9}$$

where the luminosity of the star given by

$$L_* = 4\pi R_*^2 \sigma_\mathrm{SB} T_*^4 \tag{2.10}$$

with the Stefan-Boltzmann constant σ_SB and the surface temperature of the star T_*. When a disc is considered, assuming the inner edge is close to the stellar surface, a disc surface element only receives half of this radiation since only half of the star is visible (Dullemond et al. 2001). Therefore, the flux received by a unit area of the disc surface inclined at a small angle ϕ is

$$Q_+ = \frac{1}{2}\phi F_*. \tag{2.11}$$

And, the blackbody radiation emitted by a unit area of the disc surface is

$$Q_- = \sigma_\mathrm{SB} T^4 \tag{2.12}$$

with the disc temperature T. By equating Q_+ and Q_-, it yields an expression for T that is

$$T = \left(\frac{\phi L_*}{8\pi r^2 \sigma_\mathrm{SB}}\right)^{1/4} \propto r^{-1/2}. \tag{2.13}$$

This is consistent with Eq. (2.8) for a flaring disc.

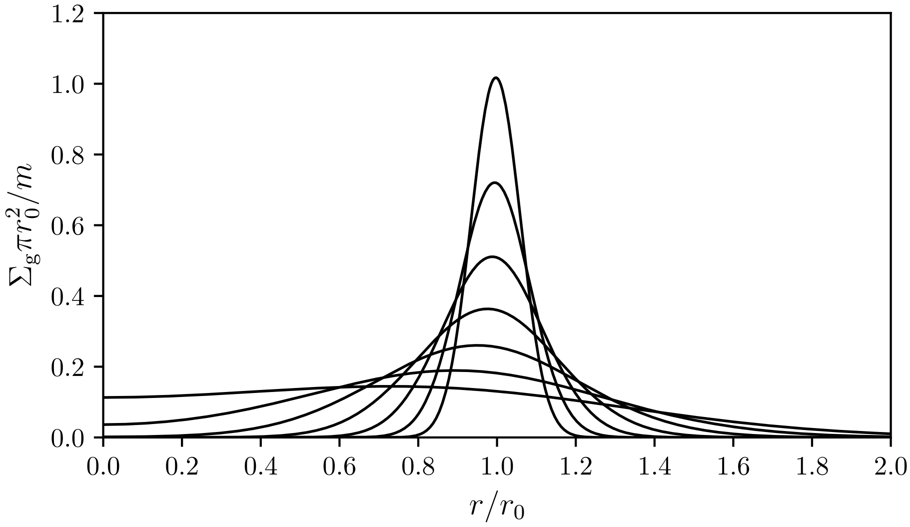

Figure 2.1: The evolution of the surface density $\Sigma_{\rm g}$ due to the viscous spreading of an annulus of mass m initially at $r = r_0$ according to the solution by Pringle (1981). Each line corresponds to the dimensionless time $\log_2 \tilde{t} = \{-7, -6, -5, -4, -3, -2, -1\}$ from the top down. The solutions show that mass flows inwards while the angular momentum is carried by an infinitesimal amount of mass outwards to infinity.

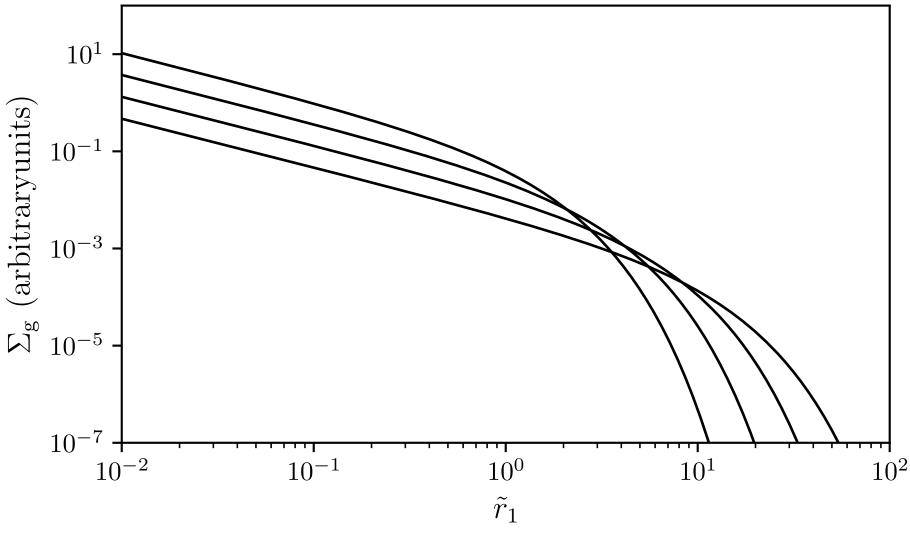

Figure 2.2: The self-similar solutions of a disc that initially has a characteristic size of $\tilde{r}_1$ and is evolving with the advection-diffusion equation. Each line corresponds to the dimensionless time $\tilde{t}_\nu = \{1, 2, 4, 8\}$ with a decreasing surface density at $\tilde{r}_1 = 1$.

2.1.3 Evolution

Solutions

The ultra-violet excess in the spectral energy distribution of young stellar objects implies accretion. For a parcel of gas in the disc, the radial forces are gravity, the radial pressure gradient force and the centrifugal force, which are balanced by

$$\frac{v_{\mathrm{g},\phi}^2}{r} = \frac{GM_*}{r^2} + \frac{1}{\rho_0}\frac{\mathrm{d}P_0}{\mathrm{d}r}. \tag{2.14}$$

In the case that the pressure in the midplane P_0 can be parameterized by $P_0 \propto r^k$, for some constant k,

$$\frac{\mathrm{d}P_0}{\mathrm{d}r} = -\frac{\mathrm{d}\log P_0}{\mathrm{d}\log r}\frac{P_0}{r} \tag{2.15}$$

with the azimuthal velocity of the gas $v_{\mathrm{g},\phi}$. With $P_0 = \rho_0 c_\mathrm{s}^2$, Eq. (2.14) can then be rewritten as

$$v_{\mathrm{g},\phi} = v_\mathrm{K}\sqrt{1-2\eta} \tag{2.16}$$

with the midplane pressure gradient parameter, or the sub-Keplerity of the gas, defined by

$$\eta \equiv -\frac{\hat{h}_\mathrm{g}^2}{2}\frac{\mathrm{d}\log P_0}{\mathrm{d}\log r}. \tag{2.17}$$

Although, typically, $\hat{h}_\mathrm{g} \ll 1$, the small deficit in the azimuthal velocity of the gas relative to the Keplerian velocity shall become significant when considering the motion of dust in the disc, which is discussed in the next section (Sec. 2.2). Limiting the discussion to the gas, the specific angular momentum of the gas is well-approximated by that of the local circular Keplerian orbit, which is

$$l = \sqrt{GM_* r}. \tag{2.18}$$

Since it increases with r, the gas has to lose angular momentum to be accreted. This can be achieved by the redistribution of angular momentum due to viscous torque.

Pringle (1981) provided a review on the steady accretion of discs and the analyses are summarized in the following. First, let us consider an axis-symmetric disc with the surface density $\Sigma_\mathrm{g}(r,t)$ and the radial velocity $v_r(r,t)$ that depend on time t. The continuity equation reads

$$r\frac{\partial \Sigma_\mathrm{g}}{\partial t} + \frac{\partial}{\partial r}(r\Sigma_\mathrm{g} v_r) = 0. \tag{2.19}$$

And, the conservation of angular momentum yields

$$r\frac{\partial(\Sigma_\mathrm{g} r^2\Omega)}{\partial t} + \frac{\partial}{\partial r}(r\Sigma_\mathrm{g} v_r \cdot r^2\Omega) = \frac{1}{2\pi}\frac{\partial G_\nu}{\partial r} \tag{2.20}$$

with the angular velocity of the disc Ω. The viscous torque acting on a disc annuli by the neighbouring outer one G_ν is given by

$$G_\nu = 2\pi r \cdot \nu \Sigma_{\rm g} r \frac{{\rm d}\Omega}{{\rm d}r} \cdot r \tag{2.21}$$

with the kinematic viscosity ν.

To evaluate the steady accretion rate, we can apply the condition that the partial time derivatives equal zero to the continuity equation and the angular momentum equation respectively. With Eq. (2.19), this yields a constant accretion rate given by

$$\dot{M}_{\rm disc} = -2\pi r \Sigma_{\rm g} v_r. \tag{2.22}$$

With Eq. (2.20), this yields

$$-\frac{\dot{M}_{\rm disc}}{2\pi} r^2 \Omega = \nu \Sigma_{\rm g} r^3 \frac{{\rm d}\Omega}{{\rm d}r} + k', \tag{2.23}$$

where k' is a constant. Close to the star, the angular velocity of the disc has to decrease from the Keplerian angular velocity to the spin angular velocity of the star. Therefore, there exists a location r_0 where ${\rm d}\Omega/{\rm d}r = 0$ that can be taken as a boundary condition. Assuming $\Omega \approx \Omega_{\rm K}$ at r_0,

$$k' = -\frac{\dot{M}_{\rm disc}}{2\pi} r_0^2 \sqrt{\frac{GM_*}{r_0^3}} \tag{2.24}$$

and Eq. (2.23) becomes

$$\Sigma_{\rm g} = \frac{\dot{M}_{\rm disc}}{3\pi\nu} \left(1 - \sqrt{\frac{r_0}{r}}\right). \tag{2.25}$$

Far away from r_0, this means a surface density is defined for a given accretion rate by $\Sigma_{\rm g} = \dot{M}_{\rm disc}/3\pi\nu$.

Eliminating G_ν and v_r and assuming $\Omega \approx \Omega_{\rm K}$ with Eq. (2.19) & (2.20), it yields the advection-diffusion equation, which is

$$\frac{\partial \Sigma_{\rm g}}{\partial t} = \frac{3}{r}\frac{\partial}{\partial r}\left[r^{1/2}\frac{\partial}{\partial r}(\nu \Sigma_{\rm g} r^{1/2})\right], \tag{2.26}$$

implying

$$v_r = -\frac{3}{\Sigma_{\rm g} r^{1/2}}\frac{\partial}{\partial r}(\Sigma_{\rm g} \nu r^{1/2}). \tag{2.27}$$

While ν likely depends on the local disc condition, or is a function of $\Sigma_{\rm g}$, t and r, the advection-diffusion equation can be solved analytically if ν is constant or is described by a power law in r. In the former case of constant ν, if we define

$$x \equiv 2r^{-1/2} \tag{2.28}$$

$$y \equiv \frac{3}{2}\Sigma_{\rm g} x, \tag{2.29}$$

then Eq. (2.26) can be rewritten as

$$\frac{\partial y}{\partial t} = \frac{12\nu}{x^2}\frac{\partial^2 y}{\partial x^2}. \tag{2.30}$$

It has the form of a diffusion equation with the diffusion coefficient

$$D = \frac{12\nu}{x^2}. \tag{2.31}$$

The diffusion timescale is given by x^2/D, which is, for a disc with length scale $r_{\rm disc}$,

$$\tau_{\rm disc} = \frac{r_{\rm disc}^2}{3\nu} \tag{2.32}$$

in physical quantities.

To illustrate the transportation of mass and momentum in the disc, Lynden-Bell & Pringle (1974) considered the solution corresponds to an annulus of mass m at $r = r_0$ initially, where the initial surface density is given by

$$\Sigma_{\rm g}(r, t = 0) = \frac{m\delta(r - r_0)}{2\pi r_0}. \tag{2.33}$$

In terms of

$$\tilde{r}_0 \equiv \frac{r}{r_0} \tag{2.34}$$

and

$$\tilde{t} \equiv \frac{12\nu}{r_0^2}t, \tag{2.35}$$

the solutions reads

$$\Sigma_{\rm g}(\tilde{r}_0, \tilde{t}) = \frac{m}{\pi r_0^2}\frac{1}{\tilde{t}}\tilde{r}_0^{-1/4}\exp\left(-\frac{1 + \tilde{r}_0^2}{\tilde{t}}\right)I_{1/4}\left(\frac{2\tilde{r}_0}{\tilde{t}}\right), \tag{2.36}$$

where $I_{1/4}(x)$ is the modified Bessel function of the first kind. Figure 2.1 shows the solutions for $\log_2\tilde{t} = \{-7, -6, -5, -4, -3, -2, -1\}$ with the peak decreases with increasing $\tilde{t}$. As the annulus evolves in time, its mass flows towards the star while the angular momentum is carried by an infinitesimal amount of mass towards infinity.

To illustrate the global evolution of a disc, the assumption of a kinematic viscosity is relaxed and described by

$$\nu \propto r^k \tag{2.37}$$

with a constant k. In the case that the disc initially has a characteristic size r_1 with a steady state accretion in the limit that $r < r_1$, a solutions at reads

$$\Sigma_{\rm g}(\tilde{r}_1, \tilde{t}_\nu) = \frac{C}{3\pi\nu_1\tilde{r}_1^k}\,\tilde{t}_\nu^{-(5/2-k)/(2-k)}\exp\left[-\frac{\tilde{r}_1^{2-k}}{\tilde{t}_\nu}\right] \tag{2.38}$$

where

$$\tilde{r}_1 \equiv \frac{r}{r_1}, \tag{2.39}$$

$$\tilde{t}_\nu \equiv \frac{t}{t_\mathrm{s}} + 1, \tag{2.40}$$

$$\nu_1 \equiv \nu(r_1) \tag{2.41}$$

and

$$t_\mathrm{s} \equiv \frac{1}{3(2-k)^2}\frac{r_1^2}{\nu_1}. \tag{2.42}$$

Here, C is a normalization constant. This solution is also self-similar as the form as shown in Eq. (2.38) can always be obtained at different times. Figure 2.2 shows the solutions for $\tilde{t}_\nu = \{1, 2, 4, 8\}$ with the surface density at $\tilde{r}_1 = 1$ decreases with increasing $\tilde{t}_\nu$.

For the case of $k = 1$, Eq. (2.38) can be rewritten as

$$\Sigma_\mathrm{g}(r, \tilde{t}_\nu) = \frac{C}{3\pi\nu_1}\tilde{t}_\nu^{-5/2}\left(\frac{r}{r_\mathrm{c}}\right)^{-1}\exp\left(-\frac{r}{r_\mathrm{c}}\right) \tag{2.43}$$

with the time-evolving characteristic radius $r_\mathrm{c} = r_1\tilde{t}_\nu$. Integrating $2\pi r\Sigma_\mathrm{g}$ with respect to r from 0 to ∞ gives the disc mass

$$M_\mathrm{disc} = \frac{2Cr_1^2}{3\nu_1}\tilde{t}_\nu^{-1/2}. \tag{2.44}$$

With the radial velocity given by Eq. (2.27) and the solution given by Eq. (2.43), the radial velocity of the gas in the disc can be expressed as

$$v_r = -\frac{3\nu}{r}\left(\frac{1}{2} - \frac{r}{r_\mathrm{c}}\right). \tag{2.45}$$

This shows that the mass is moving inwards for $r < r_\mathrm{c}/2$ and outwards otherwise. The location of transition also moves outwards as r_c increases with time.

The Shakura-Sunyaev α-disc model

The molecular viscosity in a typical disc can be shown to be too small to account for the observed evolution timescale. The kinematic viscosity of a gas with a mean free path λ can be estimated by

$$\nu = \lambda c_\mathrm{s}. \tag{2.46}$$

The mean free path is given by $\lambda = 1/n\sigma$ with the number density n and the cross-section σ. As an example, a disc around a Solar-type star typically has $\Sigma_\mathrm{g} = 10^3\mathrm{g\ cm^{-2}}$ and $\hat{h}_\mathrm{g} = 0.03$ at 1 au. The cross-section of a hydrogen molecule is about $10^{-15}\mathrm{cm}^2$. Assuming a mean molecular mass of 2.3 times of the mass of a proton, the above gives

$$\nu \sim 10^5\mathrm{cm^2\ s^{-1}}. \tag{2.47}$$

With Eq. (2.32), the corresponding evolution timescale is

$$\tau_\mathrm{disc} \sim 10^{12}\mathrm{yr}, \tag{2.48}$$

which is more than 10 times the age of the universe.

To account for the required viscosity, Shakura & Sunyaev (1973) suggested that the turbulence in the disc provides an effective viscosity. Since the maximum scale of turbulent cells is that of the local disc scale height h_g, and the maximum turbulent velocity is in the scale of c_s, the effective turbulent viscosity can be parameterized as

$$\nu = \alpha c_s h, \tag{2.49}$$

where α is a dimensionless parameter measuring the efficiency of the turbulence in transporting angular momentum. From observations of discs around T Tauri stars, Hartmann et al. (1998) estimated that $\alpha \sim 10^{-2}$ for the typical evolution timescale of 1 Myr and the typical disc size of 100 au.

2.1.4 Disc dispersal

The self-similar solution (Fig. 2.2) show that the disc becomes larger and thinner gradually in time. Meanwhile, Luhman et al. (2009) observed a disc population in the Taurus star formation region and showed that there is a clear distinction between the young discs and the evolved discs. Also, there are some discs that show a large cavity. Physically, this can be explained by photoevaporation caused by the ionization of the gas molecules (Bally & Scoville 1982; Shu et al. 1993; Hollenbach et al. 1994). Mass-loss occurs when the gas on the disc surface is heated to a sound speed $c_{\rm s,heat}$ that exceeds the local escape velocity, which occurs beyond the radius

$$r_g = \frac{2GM_*}{c_{\rm s,heat}^2}. \tag{2.50}$$

For example, the ionization due to extreme ultraviolet typically heats the disc surface to about 10^4 K resulting in a sounds speed $c_{\rm s,heat} \sim 10\,{\rm km\,s^{-1}}$. For a Solar-mass star, mass loss occurs beyond $r_g \approx 17$ au. Alexander et al. (2006) presented a physical picture that mass loss due to photoevaporation is not significant initially as the disc accretion rate is high. After a few million years, when the disc accretion rate drops and becomes comparable to the mass loss rate, a cavity is opened near r_g. As the gas supply from the outer disc is shut off, the inner disc is quickly accreted on the order of 0.1 Myr. When the inner disc is fully accreted, a large cavity is opened and the inner edge of the outer disc is directly heated by the star, which rapidly disperses the outer disc.

2.2 Dust

2.2.1 Radial drift

As discussed in Sect. 2.1.3, the azimuthal velocity of the gas in a disc has a slight deficit with respect to the local Keplerian velocity due to the radial pressure gradient. Meanwhile, dust in the disc is not supported by the gas pressure. Depending on the dust properties, it may experience a significant drag force from the gas. Weidenschilling (1977) evaluated this effect and the analyses are summarized below.

For a spherical dust particle with a radius a and a relative velocity Δv with respect to the gas, the aerodynamic drag force is given by

$$F_{\rm D} = -\frac{1}{2} C_{\rm D} \pi a^2 \rho_{\rm g} \Delta v^2. \tag{2.51}$$

The drag falls in the Epstein regime if the Knudsen number $\mathrm{Kn} \equiv \lambda/a > 4/9$. The form of the drag coefficient is given by

$$C_D = \frac{8}{3}\frac{\bar{v}}{v} \tag{2.52}$$

with the mean thermal velocity of the gas $\bar{v} = c_{\rm s}\sqrt{8/\pi}$. For larger particles, where $\mathrm{Kn} \leq 4/9$, the drag falls into the Stokes regime instead. The form of C_D is a piecewise function of the Reynolds number $\mathrm{Re} \equiv 2a\Delta v/\nu$ (Whipple 1972), which is

$$C_{\rm D} = \begin{cases} 24\mathrm{Re}^{-1} & \text{for Re} < 1; \\ 24\mathrm{Re}^{-0.6} & \text{for } 1 < \text{Re} < 800; \\ 0.44 & \text{for Re} > 800. \end{cases} \tag{2.53}$$

Nakagawa et al. (1986) provided the equations of motion of the dust and the gas in the inertial frame that read

$$\frac{\partial \boldsymbol{v}_{\rm d}}{\partial t} = -\frac{\boldsymbol{v}_{\rm d} - \boldsymbol{v}_{\rm g}}{t_{\rm stop}} - \Omega_{\rm K}^2 \mathbf{r} \tag{2.54}$$

$$\frac{\partial \boldsymbol{v}_{\rm g}}{\partial t} = -\epsilon\frac{\boldsymbol{v}_{\rm g} - \boldsymbol{v}_{\rm d}}{t_{\rm stop}} - \Omega_{\rm K}^2 \mathbf{r} - \frac{\nabla P}{\rho_{\rm g}}, \tag{2.55}$$

where the dust and gas velocities are $\boldsymbol{v}_{\rm d}$ and $\boldsymbol{v}_{\rm g}$ respectively, and the volumetric dust-to-gas ratio is $\epsilon \equiv \rho_{\rm d}/\rho_{\rm g}$. The stopping time of the dust is defined by

$$t_{\rm stop} \equiv |m_{\rm d}\Delta v/F_{\rm D}| \tag{2.56}$$

with the mass of a dust particle $m_{\rm d}$. In the limit of a steady state and the azimuthal velocities being close to the Keplerian velocity, the derivations yields the radial velocity of the dust that is

$$v_{{\rm d},r} = -\frac{2\eta v_{\rm K}}{\mathrm{St} + \mathrm{St}^{-1}(1+\epsilon)^2} \tag{2.57}$$

with the Stokes number $\mathrm{St} \equiv t_{\rm stop}\Omega_{\rm K}$. The radial drift is the fastest for dust with $\mathrm{St} = 1$. The dust that experiences significant drift has typically grown beyond the micron-size regime, which is also called pebble in the literature to emphasize its aerodynamical property. For example, in a disc around a Solar-type star at 10 au, the sub-Keplerity of the gas $\eta \sim 10^{-3}$, which translates to a radial drift velocity of 200 m s^{-1} or a decay timescale of 10^4 years.

2.2.2 Growth

Due to the relative velocity between dust particles, collisions occur, which can lead to growth, bouncing or fragmentation depending on the impact velocity and dust properties. From numerical modelling, Wada et al. (2013) found a relation for the critical relative velocity below which collision results in net growth. For icy dust particles, the critical relative velocity is

$$v_{\mathrm{frag}} \approx 80 \left(\frac{a}{0.1 \mu \mathrm{m}} \right)^{-5/6} \ \mathrm{m\ s^{-1}}, \tag{2.58}$$

and it is 10 times smaller for silicate dust particles. This is also in agreement with laboratory experiments by, for example, Wurm et al. (2005); Güttler et al. (2010); Schräpler & Blum (2011). The growth by coagulation is usually stopped at the centimetre- to metre-regime, which is also the same regime for peak radial drift of dust. These limits are collectively known as the metre-size barriers in the literature that prevents dust from growing in kilometre-sized planetesimals simply by coagulation. Detections of a substantial amount of millimeter- to centimeter-sized dust grains in discs (Testi et al. 2003; Wilner et al. 2005) is also consistent with such barriers.

To further quantify this, the barriers can be expressed as Stokes numbers. Typically, the relative velocity is dominated by turbulent velocity. In the Epstein regime of drag and small St, the turbulent fragmentation barrier is (Ormel & Cuzzi 2007)

$$\mathrm{St}_{\mathrm{frag}} = \frac{1}{3\alpha} \left(\frac{v_{\mathrm{frag}}}{c_{\mathrm{s}}} \right)^2 . \tag{2.59}$$

When the radial drift timescale is comparable to the growth timescale, the dust particle is readily removed. This condition gives the radial drift barrier (Birnstiel et al. 2012)

$$\mathrm{St}_{\mathrm{drift}} = \frac{Z}{2\eta} \tag{2.60}$$

with the surface dust-to-gas ratio Z.

2.3 Planetesimals

2.3.1 Formation

Although dust growth is limited by the the metre-size barriers, gravitational collapse models provide a leap from pebble to planetesimals. However, forming rocky planetesimals directly from a gravitationally-unstable dust disc, or through the Goldreich-Ward mechanism (Goldreich & Ward 1973), is unlikely in a typical disc environment. Such a dense dust disc shall trigger the Kelvin-Helmholtz instability at the boundary between the dust, which rotates nearly at the Keplerian velocity, and the gas above it, which rotates at a sub-Keplerian velocity (Cuzzi et al. 1993). The settling of a dense dust disc is prevented as a result.

The streaming instability (Youdin & Goodman 2005; Johansen & Youdin 2007) has been the prevailing mechanism for planetesimal formation. It leads to dense filaments of dust in the disc that subsequently collapse gravitationally into planetesimals. To trigger this process, a midplane dust-to-gas ratio of order unity is required. In support of this mechanism, Nesvorný et al. (2019) further showed that the streaming instability can also produce a distribution of binary orientations that is in good match to that of the cold classical binaries in the Kuiper belt.

Squire & Hopkins (2020) provided a physical picture, which is summarized in the following. As a dust clump drifts inwards, the back-reaction drags gas along with it. In the frame of the overall radial drift of the dust, the gas is then deflected azimuthally in the direction of disc rotation due to the Coriolis force, which also pushes the dust azimuthally causing outwards motion relative to the overall drift. This results in an enhanced dust density and the process repeats.

For the resulting planetesimals, Johansen et al. (2015) conducted a series of local shearing box simulations and fitted the mass distribution of planetesimals with a simple power law. The differential distribution of planetesimal mass m reads

$$\frac{\mathrm{d}N}{\mathrm{d}m} \propto m^{-p} \tag{2.61}$$

with $p \approx 1.6$. Simon et al. (2016, 2017) and Abod et al. (2019) further tested the effects of resolution, the Stokes number of the dust particles, the relative strength of self-gravity with respect to shear and the radial pressure gradient. They found similar fitting to the mass distribution of planetesimals, which is also independent of these factors. Nonetheless, Abod et al. (2019) also showed that a truncated power-law gives a better fit. In the cumulative form, the mass distribution is

$$N(> m) = Cm^{-p+1} \exp\left(-\frac{m}{m_0}\right) \tag{2.62}$$

with the normalization constant C and the characteristic mass m_0. In general, these works are successful in forming planetesimals of 10^2 to 10^3 km in size under typical disc conditions.

2.3.2 Growth

Planetesimal accretion

Formation of planets through planetesimal accretion is a long-standing topic in the field. Kokubo & Ida (1998, 2000) conducted a range of N-body simulations to study the evolution and growth of a swarm of planetesimals. Their results showed a stage of runaway growth at the beginning, where the more massive ones grow faster. As the protoplanets reach about 50 times the mass of the planetesimals, significant dynamical heating occurs to the nearby planetesimals increasing their velocity dispersion. This slows down accretion and the growth becomes oligarchic. Orbital repulsion further causes the massive protoplanets to be separated by 5 to 10 Hill radii, which is defined by

$$r_\mathrm{H} = \left(\frac{m}{3M_*}\right)^{1/3} a(1-e) \tag{2.63}$$

with the semimajor axis a and the eccentricity e of the orbit. This results in a bimodal distribution of bodies that consists of a few protoplanets and a swarm of planetesimals. Further estimation from the results shows that it requires ~ 40 Myr at 5 au to form a 5 $M_\oplus$ core. As a core of about 10 $M_\oplus$ is required by the core accretion model to form giant planets, planetesimal accretion cannot form such core within the disc lifetime to accrete gas. While the formation of terrestrial planets is not constrained by disc dispersal, an alternative path to grow planetesimals efficiently is required to form giant planet.

Pebble accretion

Instead of pair-wise accretion of planetesimals, Ormel & Klahr (2010) and Lambrechts & Johansen (2012) considered the scenario that the planetesimals co-exist with the leftover dust in the disc. They showed that the growth is significantly more efficient than planetesimal accretion and this mechanism is referred to as pebble accretion in the literature (see Johansen & Lambrechts 2017; Ormel 2017, for review). Physically, a dust particle in the disc experiences both gas drag and the gravitational force during an encounter with a planetesimal. When the encounter is strong, the dust particle is deflected significantly from the gas streamline. As a result, the particle experiences strong gas resistance, which then loses kinetic energy and settles onto the planetesimal.

To quantify this, let us consider the three relevant timescales: a) the encounter time $t_{\rm enc}$ between the planetesimal and the dust particle; b) the settling time $t_{\rm set}$ required by the dust particle to settle onto the planetesimal, and; c) the stopping time $t_{\rm stop}$ that describes the strength of aerodynamics for the dust particle. For a dust particle approaching a planetesimal of mass m along the gas streamline with impact parameter b and the approach velocity v_∞,

$$t_{\rm enc} = \frac{2b}{v_\infty}, \tag{2.64}$$

and

$$t_{\rm set} = \frac{b^3}{Gmt_{\rm stop}}. \tag{2.65}$$

As it is more fundamental describe the dust particle with its aerodynamical size, or the Stokes number, the stopping time is expressed as

$$t_{\rm stop} = \frac{\rm St}{\Omega_{\rm K}}. \tag{2.66}$$

For pebble accretion, the conditions of $t_{\rm stop} < t_{\rm enc}$ and $t_{\rm set} < t_{\rm enc}$ are required.

In the limit that the planetesimal is in a circular Keplerian orbit and the dust is initially following the gas streamline, the approach velocity v_∞ of a pebble is given by

$$v_\infty \approx \eta v_{\rm K} + \frac{3}{2}\Omega_{\rm K} b. \tag{2.67}$$

Depending on the relative magnitude of the two terms, this can be divided into two regime. For large b or small m, the approach velocity is dominated by the Keplerian shear, which is referred to as the shear or the Hill limit. For small b or large m, the approach velocity is dominated by the sub-Keplerity of the gas instead, which is referred to as the headwind or the Bondi limit.

In the shear limit, t_{enc} is smaller than $1/\Omega_{\mathrm{K}}$. Therefore, for dust particles with $\mathrm{St} < 1$, the requirement of $t_{\mathrm{stop}} < t_{\mathrm{enc}}$ is always satisfied. With $t_{\mathrm{enc}} \sim 1/\Omega_{\mathrm{K}}$ and $t_{\mathrm{set}} = t_{\mathrm{enc}}$, this yields an accretion cross section

$$b_{\mathrm{sh}} \sim \mathrm{St}^{1/3} r_{\mathrm{H}}, \tag{2.68}$$

which is about 22% of r_{H} for St of 10^{-2} and is much larger than the planetesimal's physical radius.

In the headwind limit, with $v_\infty = \eta v_{\mathrm{K}}$, the requirement of $t_{\mathrm{stop}} < t_{\mathrm{enc}}$ is not always fulfilled. However, we have to use the second requirement of $t_{\mathrm{set}} < t_{\mathrm{enc}}$ to retrieve the accretion cross section b_{hw}, which is given by

$$b_{\mathrm{hw}} \sim a\sqrt{\frac{2\mathrm{St}}{\eta}\frac{m}{M_*}}. \tag{2.69}$$

Returning to the first requirement, it results in a critical planetesimal mass, or the pebble accretion onset mass, $m_{\mathrm{PA,hw}}$, which is given by

$$m_{\mathrm{PA,hw}} = \frac{1}{8}\mathrm{St}\eta^3 M_*. \tag{2.70}$$

For $\mathrm{St} = 10^{-1}$, $\eta = 10^{-3}$ and a Solar-mass star, $m_{\mathrm{PA,hw}} \sim 10^{-5} M_\oplus$.

While the simple analysis above assumes that the planetesimal is in a circular orbit, which may not be true in a swarm of planetesimals due to dynamical heating. The prescription by Liu & Ormel (2018) and Ormel & Liu (2018) further relaxed such assumption. The consequences are investigated and discussed in Chapter 3 (Lau et al. 2024b) and Chapter 4 (Lau et al. 2022).

As the planetesimal grows into a planetary core of substantial mass, a gap shall open in the disc that causes a radial pressure maxima externally when $r_{\mathrm{H}} \gtrsim H_{\mathrm{g}}$ (Lin & Papaloizou 1986). The supply of pebble from the outer disc is then interrupted and pebble accretion stops, which is referred to as pebble isolation in the literature. From the gap opening condition that is approximated by $m/M_* > \hat{h}_{\mathrm{g}}$, the pebble isolation mass is

$$m_{\mathrm{iso}} \approx 40\left(\frac{M_*}{M_\odot}\right)\left(\frac{\hat{h}_{\mathrm{g}}}{0.05}\right)^3 M_\oplus. \tag{2.71}$$

Lambrechts et al. (2014) and Bitsch et al. (2015a) further suggested a factor of 0.5 to m_{iso} based on radiative hydrodynamical simulations. As pebble accretion terminates, gas can cool around the planetary core and become gravitationally bound.

2.4 Planets

2.4.1 Gas accretion

To form giant planets, there are two prevailing theories: the core accretion model (Mizuno 1980; Bodenheimer & Pollack 1986; Pollack et al. 1996), and the gravitational collapse model (Kuiper 1951; Cameron 1978; Boss 1997). In the context of the Solar system, the giants planets are very likely formed through core accretion due to their masses. In the disc, a planetary core of about $10M_\oplus$, which mainly consists of solid, is required to start accreting a gas envelope. At the beginning, hydrostatic equilibrium is maintained in the envelope by the energy released by solid accretion and the Kelvin-Helmholtz contraction envelope. This stage is also referred to as the thermal contraction phase. When the core reaches a critical mass, the hydrostatic equilibrium can no longer be maintained and the runaway gas accretion phase starts, where the envelop contracts on its Kelvin-Helmholtz timescale. As it is a runaway process, gas accretion stops only when a deep gap is opened in the disc, which limits the gas supply, or when the gas disc itself disperses.

The calculations by Bodenheimer & Pollack (1986) shows that the critical core mass equals the envelope mass assuming a constant core growth rate. In a more detailed calculation by Ikoma et al. (2000), they showed that there is no clear distinction, but a gradual transition between the two phases as shown by the growth rates of the core mass and the envelope mass. They further shows that the critical core mass depends on the core growth rate and the opacity of the envelope, which is roughly a few times larger than the envelope mass for the adopted parameters. Nonetheless, they also considered the case of halted core growth, which is applicable when both pebble accretion and planetesimal accretion stop. And, they arrived at a similar critical core mass as that in Bodenheimer & Pollack (1986).

For the gas accretion rate in the thermal contraction phase $\dot{m}_{\rm cool}$, Bitsch et al. (2015b) extracted the calculation results in Piso & Youdin (2014) as

$$\begin{aligned}\dot{m}_{\rm cool} \approx 4.375\times10^{-9}\left(\frac{\kappa}{\rm cm^2\ g^{-1}}\right)^{-1}\left(\frac{\rho_{\rm c}}{5.5\ \rm g\ cm^{-3}}\right)^{-1/6}\times \\ \left(\frac{m_{\rm c}}{M_\oplus}\right)^{11/3}\left(\frac{m_{\rm env}}{M_\oplus}\right)^{-1}\left(\frac{T}{81\rm K}\right)^{-1/2} M_\oplus {\rm yr}^{-1},\end{aligned} \tag{2.72}$$

with the opacity of the gas envelope κ, the density of the core $\rho_{\rm c}$, the core mass $m_{\rm c}$ and the envelope mass $m_{\rm env}$. As $\dot{m}_{\rm cool} \propto 1/m_{\rm env}$, the growth of the envelope is orderly.

In the runaway gas accretion phase, where $m_{\rm env} > m_{\rm c}$, the envelope grows at the Kelvin-Helmholtz timescale, which is (Ikoma et al. 2000)

$$\tau_{\rm KH} = 10^b\left(\frac{m}{M_\oplus}\right)^{-c}\left(\frac{\kappa}{1\ \rm cm^2\ g^{-1}}\right){\rm yr} \tag{2.73}$$

with $b \approx 8$ and $c \approx 2.5$. Meanwhile, in the literature, Bryden et al. (2000) gave $b \approx 10$ and $c \approx 3.0$, and Ida & Lin (2004) adopted $b = 9$ and $c = 3$. The mass accretion rate is then given by

$$\dot{m}_{\rm runaway} = \frac{m}{\tau_{\rm KH}}. \tag{2.74}$$

As $\dot{m}_{\rm runaway} \propto m^c$ with $c \approx 2.5$ or 3, the growth is runaway.

The gas accretion rates in both cases are proportional to the opacity envelope. In general, it depends on the disc conditions and the dust processes within the envelope. This is still an active field of research (e.g. Szulágyi et al. 2016; Lambrechts et al. 2019; Schulik et al. 2019; Ormel et al. 2021; Brouwers et al. 2021) and the adopted values in the current planet formation models span over a wide range, from $\sim 10^{-2}$ to $1\ \rm cm^2\ g^{-1}$.

The above analyses only consider the ability of the planet in accreting gas, however, the supply of gas may become a limiting factor especially when the planet becomes massive. With two-dimensional hydrodynamical simulations, Tanigawa & Watanabe (2002) studied the accretion flow fed to the planet providing an additional limit, which is

$$\dot{m}_{\rm hydro} = 0.29\Sigma_{\rm g} r^2 \Omega_{\rm K} \left(\frac{m}{M_*}\right)^{4/3} \hat{h}_{\rm g}^{-2}. \tag{2.75}$$

In addition, with a semi-analytical model, Lubow & D'Angelo (2006) suggested that the gas accretion rate should be limited at 0.75 to 0.9 of the disc accretion rate. Finally, the numerical simulations in Dobbs-Dixon et al. (2007) showed that the planet would approach an asymptotic mass at which $r_{\rm H} \sim H_{\rm g}$ due to gap opening, which is discussed in the next subsection (Sect. 2.4.2).

2.4.2 Planet-disc interactions

Planet migration

A planet shall interact with the disc gravitationally and exchange torques. The effects on the planet's orbit are generally called planet migration in the literature (see Kley & Nelson 2012, for review), which is first studied by Goldreich & Tremaine (1979, 1980) and Lin & Papaloizou (1986). In general, the gas external to the planet orbits at a lower angular velocity and receives angular momentum from the planet. Meanwhile, the gas internal to the planet orbits at a higher angular velocity and loses angular momentum to the planet.

For a low-mass planet in a vertically isothermal disc, the torque can be evaluated through a linear analysis of the perturbations in the disc Goldreich & Tremaine (1979, 1980) and Tanaka et al. (2002). Assuming circular and planar orbit of the planet, the gravitational potential $\psi_{\rm p}$ is azimuthally periodic and can be expanded into a Fourier series, which is

$$\psi_{\rm p}(r, \phi, t) = -\frac{G}{|\mathbf{r}_{\rm p}(t) - \mathbf{r}|} \tag{2.76}$$

$$= \sum_{k=0}^{\infty} \psi_k(r) \cos k[\phi - \phi_{\rm p}(t)] \tag{2.77}$$

in the polar coordinate (r, ϕ) and at time t. The position of the planet is $(r_{\rm p}, \phi_{\rm p})$ and the coefficient ψ_k corresponds to the k-th mode. The total torque exerted on the planet is then

$$\Gamma_{\rm tot} = -\int \Sigma(\mathbf{r} \times -\nabla\psi_{\rm p}) {\rm d}A \tag{2.78}$$

$$= \int \Sigma \frac{\partial \psi_{\rm p}}{\partial \phi} {\rm d}A \tag{2.79}$$

with a element of the disc surface dA. In the disc, waves are excited at locations where resonance occurs between the orbital frequency of the planet and the epicyclic frequency, which is the local Keplerian frequency assuming the gas rotates at the Keplerian velocity. At these locations, angular momentum exchange occurs. This includes the co-rotation resonance, which occurs in the planet's radial location, and the Lindblad resonances, which are at

$$r_{\mathrm{L}} = \left(1 \pm \frac{1}{k}\right)^{2/3} r_{\mathrm{p}} \tag{2.80}$$

for all integers k. The Lindblad resonances occur external to the planet are also called the outer Lindblad resonances. And, those occur internal to the planet are called the inner Lindblad resonances. If the radial gas pressure gradient is considered for the epicyclic frequency, Artymowicz (1993) further showed that the total torque converges. For large k, the Lindblad resonance occurs at $r_{\mathrm{p}} \pm 2H_{\mathrm{g}}/3$, which is also generally where the torque density peaks. Through the linear analysis, Tanaka et al. (2002) and Tanaka & Ward (2004) derived a characteristic time of planet migration

$$t_{\mathrm{wa}v} = \left(\frac{M_*}{m}\right)\left(\frac{M_*}{\Sigma_{\mathrm{g}} r^2}\right)\left(\frac{\hat{h}_{\mathrm{g}}^4}{\Omega_{\mathrm{K}}}\right). \tag{2.81}$$

However, Paardekooper & Papaloizou (2008) showed that if the disc is not locally isothermal, which occurs if heat is not dissipated efficiently, the co-rotation torque becomes non-linear and breaks the above analysis. Due to a finite width of the co-orbital region, there are gas that travels in the horseshoe orbit around the planet that is not considered in the linear theory. Since there exists an asymmetry in the change in density when the gas makes the two horseshoe turns adiabatically, a net angular momentum exchange occurs. As the gas circulates in the co-orbital region on the libration timescale, if the thermal diffusion timescale is longer than the libration timescale, the co-rotation torque saturates eventually after some libration timescales. Otherwise, a quasi-steady occurs that the co-rotation torque is saturated and can lead to a positive total torque in a longer timescale. Paardekooper et al. (2010, 2011) provided a set of formulae describing total torque Γ_{tot} exerted on the planet that is a sum of the Lindblad torque and the co-rotation torque. The key parameters that determine the sign of the total torque are the surface density gradient and the temperature gradient. Cresswell & Nelson (2008) and Coleman & Nelson (2014) further modified the torque formulae considering the torque reductions due to finite eccentricity and inclination of the planet's orbit.

For the effects on the planet's orbit, it is more insightful to describe planet migration with timescales. Tanaka et al. (2002) defined a migration timescale as

$$\tau \equiv -\frac{r_{\mathrm{p}}}{\dot{r}_{\mathrm{p}}}, \tag{2.82}$$

where inwards migration has a positive timescale. The rate of change of r_{p} is given by

$$\dot{r}_{\mathrm{p}} = \dot{L}_{\mathrm{p}} \frac{\mathrm{d}r_{\mathrm{p}}}{\mathrm{d}L_{\mathrm{p}}} \tag{2.83}$$

$$= \frac{2 r_{\mathrm{p}} \Gamma_{\mathrm{tot}}}{L_{\mathrm{p}}}, \tag{2.84}$$

with the angular momentum of the planet L_p. However, Muto et al. (2011) noted that, for non-zero eccentricity of the planet's orbit

$$L_\mathrm{p} = \sqrt{a(1-e^2)}, \tag{2.85}$$

with the semimajor axis a and the eccentricity e, the migration timescale is, instead,

$$\begin{aligned} \tau_\mathrm{m} &\equiv -\frac{L_\mathrm{p}}{\dot{L}_\mathrm{p}} \qquad (2.86) \\ &= \left(\frac{1}{2\tau_a} - \frac{e^2}{1-e^2}\frac{1}{\tau_e}\right)^{-1}. \qquad (2.87) \end{aligned}$$

This can be rearranged as

$$\tau_a = \frac{1}{2}\left(\frac{1}{\tau_m} + \frac{e^2}{1-e^2}\frac{1}{\tau_e}\right)^{-1}. \tag{2.88}$$

The timescales for the rate of change in the semimajor axis and eccentricity are defined respectively by $\tau_a \equiv -a/\dot{a}$ and $\tau_e \equiv -e/\dot{e}$.

Tanaka & Ward (2004) provided the expressions for τ_e, as well as the timescale for the rate of change in the inclination $\tau_i \equiv -i/\dot{i}$. Combining the results of torque reduction by Cresswell & Nelson (2008) and Coleman & Nelson (2014), these timescales are

$$\begin{aligned} \tau_e &= 1.282 t_\mathrm{wav}(1 - 0.14\hat{e}^2 + 0.06\hat{e}^3 + 0.18\hat{e}^2\hat{i}^2) \qquad (2.89) \\ \tau_i &= 1.838 t_\mathrm{wav}(1 - 0.30\hat{i}^2 + 0.24\hat{i}^3 + 0.14\hat{e}^2\hat{i}^2) \qquad (2.90) \end{aligned}$$

with the reduced eccentricity $\hat{e} \equiv e/\hat{h}_\mathrm{g}$ and the reduced inclination $\hat{i} \equiv \sin i/\hat{h}_\mathrm{g}$.

To apply these timescales as a force exerted on a planet, a set of equations of motion is required. More recently, Ida et al. (2020) noted that there exist discrepancies among the torque formalisms and the equations of motion by different works in the literature and attempted to unify these formalisms. They proposed that the acceleration experienced by the planet is

$$\boldsymbol{a} = -\frac{v_\mathrm{K}}{2\tau_a}\boldsymbol{e}_\theta - \frac{v_r}{\tau_e}\boldsymbol{e}_r - \frac{v_\theta - v_\mathrm{K}}{\tau_e}\boldsymbol{e}_\theta - \frac{v_z}{\tau_i}\boldsymbol{e}_z \tag{2.91}$$

in the cylindrical coordinates (r, θ, z) and the velocity of the planet is $\boldsymbol{v} = (v_r, v_\theta, v_z)$.

As mentioned in Sect. 2.3.2, when a planet is massive enough, the tidal interactions with the disc causes the gas being pushed away from the planet and a gap is opened in this disc. In the literature, the low-mass and the high-mass regimes are often referred to as Type-I migration and the Type-II migration regimes respectively. By analytical modelling, Ward (1997) suggested that the migration of the planet is in the viscous evolution timescale of the disc, where the Type-II migration migration timescale is given by

$$\tau_{a,\mathrm{II}} = \frac{2}{3}\frac{a^2}{\nu}. \tag{2.92}$$

Similarly with analytical methods, Hasegawa & Ida (2013) further suggested that there is a planet-dominated regime when the planet's mass is high and its migration is limited by inertia.

To transit from the Type-I to the Type-II migration regime, Bate et al. (2003) provided an empirical formula that the migration timescale for a general mass is given by

$$\tau_{a,\mathrm{I,II}} = \frac{\tau_a}{1 + (m/M_\mathrm{t})^3} + \frac{\tau_{a,\mathrm{II}}}{1 + (M_\mathrm{t}/m)^3}. \tag{2.93}$$

The transition mass M_t is

$$M_\mathrm{t} = \frac{3}{5M_\mathrm{H}} \tag{2.94}$$

and the mass at which the Hill radius equals the local disc scale height is

$$M_\mathrm{H} = 3M_* \hat{h}_\mathrm{g}^3. \tag{2.95}$$

However, recent hydrodynamic simulations by Dürmann & Kley (2015) and Duffell et al. (2014) shows that a substantial amount of gas can pass through the planetary gap, where the planet is not locked to the viscous accretion of the disc. Through a broad parameter study, Kanagawa et al. (2018) proposed that the magnitude of the torque depends directly on the surface density at the bottom of the gap. This treatment also implies a smooth transition between the Type-I and the Type-II migration regimes.

Gap opening

Due to the importance of gap opening on planet migration, multiple works (e.g. Duffell & MacFadyen 2013; Fung et al. 2014; Kanagawa et al. 2015a, 2016; Fung & Chiang 2016; Duffell 2020) have studied the relation between the gap structure and the planet mass. Empirically, Kanagawa et al. (2015b) suggested that the ratio between the surface density at the bottom of the gap $\Sigma_\mathrm{g,min}$ and the unperturbed value $\Sigma_\mathrm{g,0}$ can be described by

$$\frac{\Sigma_\mathrm{g,min}}{\Sigma_\mathrm{g,0}} = \frac{1}{1 + 0.04K}, \tag{2.96}$$

where the gap opening factor K is

$$K = \left(\frac{m}{M_*}\right)^2 \hat{h}_\mathrm{g}^{-5} \alpha^{-1}. \tag{2.97}$$

While they focused on the depth and the width of the gap, the recent work by Duffell (2020) further improved the empirical formula for the overall gap shape. Figure 2.3 shows the gap shapes for planets in a disc with $\hat{h}_\mathrm{g} = 0.05$ and $\alpha = 10^{-3}$. The ratios of the planet mass to the central star's $m/M_* = \{0.1, 0.2, 0.5, 1, 2\} \times M_\mathrm{J}/M_\odot$ and the surface density decreases with increasing planet mass.

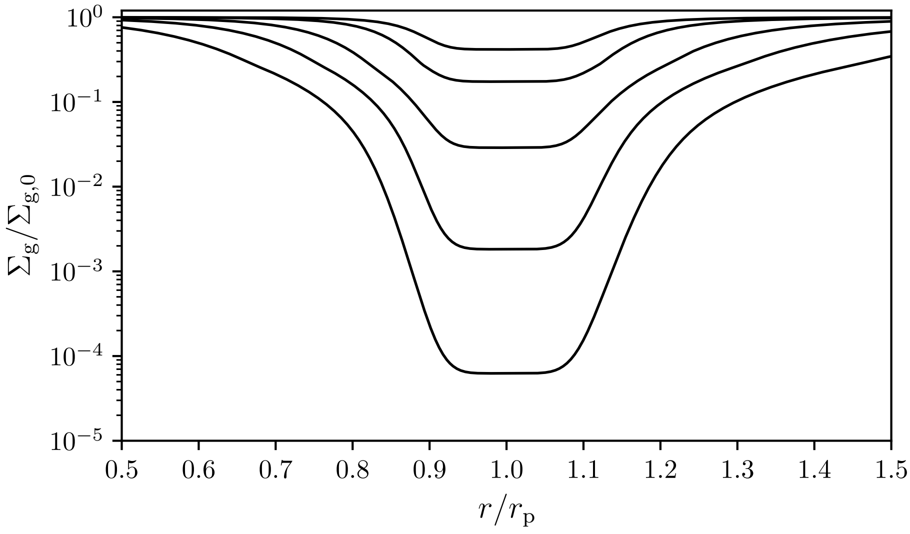

Figure 2.3: The radial planetary gap profiles according to the empirical formula by Duffell (2020) shown in terms of the ratio of the perturbed surface density to the unperturbed one $\Sigma_{\rm g}/\Sigma_{\rm g,0}$. The planet is at $r_{\rm p}$ and each line corresponds to the planet-mass to stellar mass ratio $m/M_* = \{0.1, 0.2, 0.5, 1, 2\} \times M_{\rm J}/M_\odot$ from the top down.

2.5 Motivation

2.5.1 Substructure in protoplanetary discs

In the planet formation theories reviewed above, the protoplanetary discs in the Class II stage are generally assumed to be smooth. With the recent high-resolution interferometry observations by the Atacama Large Millimeter/submillimeter Array (ALMA), substructure is likely common. Multiple large surveys (e.g. Andrews et al. 2018; Long et al. 2018; Dullemond & Penzlin 2018; Cieza et al. 2021) showed that most of the substructures are axisymmetric. Although the resolved discs are general the large and bright ones, theoretical models and disc population synthesis studies (Toci et al. 2021; Zormpas et al. 2022; Delussu et al. 2024) suggested that dust trapping by substructures is required to explain the observations of the unresolved discs. Furthermore, Teague et al. (2018a,b) showed that the dust rings coincide with the local pressure maxima in the kinematic studies with ALMA. These observations have greatly changed planet formation theory (see Drążkowska et al. 2023, for a recent review).

From the theoretical point of view, substructure in the disc also provides a favourable environment for planet formation. Streaming instability, which forms planetesimal from the subsequent gravitational collapse, requires a significant enhanced midplane dust-to-gas ratio relative to the Solar metallicity (Sect. 2.3.1), which is likely achievable in a dust ring (e.g. Drążkowska et al. 2016). In the meantime, planet migration is likely efficient for planetary cores of 1 to 10 $M_\oplus$ in typical disc environment just before the transition to the Type-II or the high mass regime (Sect. 2.4.2). This poses the migration problem in explaining the location of Jupiter (e.g. Matsumura et al. 2017; Liu et al. 2019; Bitsch et al. 2019), and these models assume a smooth disc in general. When a substructured disc is considered (e.g. Coleman & Nelson 2016a; Morbidelli 2020; Guilera et al. 2020; Chambers 2021; Andama et al. 2022), the planetary cores can be retained near the pressure bump due to the change in the slope of the surface density that causes a zero-net torque region.

Based on these, Chapter 3 presents a published work (Lau et al. 2024b) in attempting forming the Solar System's giant planets in a smooth disc. This work further emphasizes the difficulty in retaining planetary cores in a smooth disc. Although this work has failed the original attempt, it explicitly compares two pebble accretion prescriptions: the one by Ida et al. (2016) and, the one by Liu & Ormel (2018) and Ormel & Liu (2018). The former one assumed the eccentricity of the planet is small when evaluating the pebble approach velocity, while the latter relaxed this assumption that causes planetesimals that are stirred by early-grown planetary cores inefficient in accreting pebbles.

Considering disc substructure, Chapter 4 presents a published work (Lau et al. 2022) that studies the consequence of the presence of a pressure bump in the disc. This work combined a disc model with dust evolution and an N-body code to start from micron-sized dust. The key planet formation processes reviewed are also included up to the point that pebble isolation occurs. This work found that planetesimals formed at the substructure can grow by pebble accretion rapidly as the dust-rich environment required to form planetesimals is also a favourable environment for pebble accretion. The planetary cores produced are also retained from migration and trapped near the pressure bump. When gas accretion and gap opening are further built into the model, it becomes more involved in the recent observations and open questions about the Solar System as discussed below.

2.5.2 The Solar System

Meteoritic dichotomy

The non-carbonaceous (NC) and carbonaceous (CC) dichotomy in the meteoritic records (see Kleine et al. 2020, for review) shows that the inner Solar System (NC) reservoir had no significant influx of outer Solar System (CC) reservoir for about 1.5 Myr. This also shows that planetesimal formation spanned over a long period of time, likely until disc dispersal. Due to the rapid inwards drift of pebbles due to aerodynamic drag in protoplanetary discs, as discussed in Sect. 2.2, Kruijer et al. (2017) proposed that a significant exchange of the NC-CC reservoirs can be achieved if Jupiter's core formed rapidly and interrupted the inward drift of dust.

Architecture

In the meantime, the prevailing models that explains different aspects of the Solar System's architecture generally require the giant planet in a compact configuration initially. This includes the Nice model and its variants (e.g. Tsiganis et al. 2005; Morbidelli et al. 2005), and the early instability model (e.g. Clement & Kaib 2017; Deienno et al. 2018)

As a continuation of Lau et al. (2022), Chapter 5 presents a published work (Lau et al. 2024a) that studied the formation of giant planets initiated by a substructure in the disc. This work shows that gas giant can form rapidly at a pressure bump that effectively prevents dust from the outer disc from drifting through. The remaining dust is then accumulated at the outer edge of the planetary gap and triggers the formation of the next generation of planets. A scenario of sequential planet formation is demonstrated. The second generation of planets are formed significantly later, which can explain the masses of the ice giants of the Solar System. Also, the giant planets are in a compact configuration, which supports the initial conditions of the models on the Solar System's architecture from a formation point of view.

The Kuiper belt

As discussed in Sect. 2.3.1, the cold classical Kuiper belt objects are likely the direct product of planetesimal formation. Since an enhanced dust-to-gas ratio is required by the streaming instability, they should have formed in a dust-rich environment that also favours the growth by pebble accretion. Therefore, other physical processes or conditions are required to prevent their growth. Chapter 6 presents an on-going work that includes internal photoevaporation to disperse the disc. Early results show that a ring of planetesimals can form from the expanding cavity in the disc, where growth is prevented as the gas disperses rapidly near the end of the disc lifetime.

The planet formation model developed through these works connects the key planet formation processes. At the current stage, it is still quite limited in terms of the parameter space due to the computational cost. Also, the source of the substructure has not been studied in detail. These are further discussed in Chapter 7 on the future outlook of this model to achieve a more complete picture of planet formation.

Chapter 3

Can the giant planets of the Solar System form via pebble accretion in a smooth protoplanetary disc?

Tommy Chi Ho Lau, Man Hoi Lee, Ramon Brasser, and Soko Matsumura

This chapter was published in Astronomy & Astrophysics, 683, A204 (2024). A part of this chapter was submitted in partial fulfilment of the requirements for the degree of Master of Philosophy at The University of Hong Kong in June 2021 while a substantial amount of work was conducted in the course of this thesis.

Abstract: Prevailing N-body planet formation models typically start with lunar-mass embryos and show a general trend of rapid migration of massive planetary cores to the inner Solar System in the absence of a migration trap. This setup cannot capture the evolution from a planetesimal to embryo, which is crucial to the final architecture of the system. We aim to model planet formation with planet migration starting with planetesimals of $\sim 10^{-6} - 10^{-4} M_{\oplus}$ and reproduce the giant planets of the Solar System. We simulated a population of 1,000 – 5,000 planetesimals in a smooth protoplanetary disc, which was evolved under the effects of their mutual gravity, pebble accretion, gas accretion, and planet migration, employing the parallelized N-body code SyMBAp. We find that the dynamical interactions among growing planetesimals are vigorous and can halt pebble accretion for excited bodies. While a set of results without planet migration produces one to two gas giants and one to two ice giants beyond 6 au, massive planetary cores readily move to the inner Solar System once planet migration is in effect. Dynamical heating is important in a planetesimal disc and the reduced pebble encounter time should be considered in similar models. Planet migration remains a challenge to form cold giant planets in a smooth protoplanetary disc, which suggests an alternative mechanism is required to stop them at wide orbits.

3.1 Introduction

Planet formation involves the growth from interstellar grains of sub-micron sizes to planets of thousands of kilometres in diameter, which is a process through at least 12 orders of magnitude in length scale. Details of the involved processes are still under ongoing research. Particularly, the formation of solid cores which subsequently accrete gas is a crucial yet still unclear step. This has been an active field of research for decades and requires further investigations.

Weidenschilling (1977) presented a classic problem in planet formation that, due to aerodynamic drag in protoplanetary discs, solids of 10 cm to 1 m in size typically have a radial drift timescale of $\sim$ 100 years, which is much shorter than the typical disc lifetime of $1-10$ Myr. Furthermore, laboratory experiments of collisions (e.g. Wurm et al. 2005; Güttler et al. 2010) also show a general behaviour that millimetre-sized grains require extremely small relative velocities to grow, so that fragmentation and bouncing are avoided. These barriers of particle growth are often summarized as the ‘metre-size barrier’ in the literature. This implies that planetesimals of a kilometre in size have to form rapidly through the metre-sized scale from dust via an alternative process.

The Goldreich-Ward mechanism suggests the formation of planetesimals through gravitational collapse of a very dense dust disc as a result of dust settling (Goldreich & Ward 1973), where the dust disc needs to be $\sim 10^4$ times thinner than the gas disc. However, Cuzzi et al. (1993) showed that this cannot occur in a protoplanetary disc. The dense dust disc at the midplane, along with the gas in it, rotates at the Keplerian velocity; however, the gas disc immediately above rotates at a sub-Keplerian velocity due to the radial pressure gradient. This results in a steep vertical velocity gradient at the dust-gas interface, which induces the Kelvin-Helmholtz instability, preventing the dust disc from settling and collapsing gravitationally.

However, settling a dust disc with a solid density comparable to the gas density is possible without triggering the Kelvin-Helmholtz instability. Analyses in multiple works (e.g. Youdin & Goodman 2005; Youdin & Lithwick 2007; Johansen et al. 2007, 2009; Bai & Stone 2010) suggest this can induce non-gravitational clumping of dusts due to disc turbulence or streaming instability. The over-densities of dust can subsequently collapse through gravity on an orbital timescale. Recent hydrodynamic numerical simulations (e.g. Johansen et al. 2012, 2015; Simon et al. 2016, 2017) further show that dense filaments of solid particles undergo gravitational collapse and planetesimals up to about the size of Ceres are almost instantly formed. This process is a viable pathway for planetesimal formation.

The classical core accretion model of gas giant formation (Mizuno 1980; Pollack et al. 1996) requires a solid core of $\sim 10M_\oplus$. Beyond the critical mass, hydrostatic equilibrium in the gas envelope cannot be maintained, resulting in runaway gas accretion. The growth ends as the supply of gas is terminated due to gap opening in the disc or gas dispersal as the disc evolves.

Through N-body simulations, Kokubo & Ida (1998, 2000) showed that pairwise accretion of planetesimals results in runaway growth, where more massive bodies grow faster. As protoplanets grow massive enough to interact with each other gravitationally, their orbital separations remain larger than $\sim$ 5 Hill radii and growth becomes oligarchic, where the growth rate is slower for more massive bodies. This results in a bimodal system of a few protoplanets and a population of small planetesimals. Their extrapolation estimates that the growth timescale to reach

$5 - 10\ M_\oplus$ is of the order of $10 - 100$ Myr beyond 5 au, which is much longer than the typical disc lifetime. Since a solid core of $\sim 10 M_\oplus$ has to be formed before disc dispersal in order to accrete gas, a more efficient planetesimal growth mechanism is required.

Large populations of grains ranging from millimetres to tens of centimetres in radius, or pebbles, have been detected in protoplanetary discs by millimetre to centimetre observations (e.g. Testi et al. 2003; Wilner et al. 2005). These observations are consistent with the metre-size barrier mentioned above. The growth of these small particles is stalled and they remain throughout most of the lifetime of the discs (Cleeves et al. 2016). This lays the foundation for the notion of pebble accretion. In this scenario, a large population of pebbles, as leftover solids, co-exists with planetesimals, in contrast to the classical scenario where pebbles are neglected for the growth of planetesimals of the order of a kilometre and beyond. Planetesimals that are massive enough to gravitationally deflect pebbles from the gas streamline and have a long enough encounter time can accrete a significant fraction of the drifting pebbles. This emerges as a mechanism for efficient planetesimal growth commonly called 'pebble accretion' (Ormel & Klahr 2010; Lambrechts & Johansen 2012; Guillot et al. 2014; see Johansen & Lambrechts 2017; Ormel 2017, for review).

Kretke & Levison (2014) conducted a series of numerical simulations incorporating pebble accretion with an initial mass spectrum of $\sim 10^6$ planetesimals. The Lagrangian Integrator for Planetary Accretion and Dynamics (LIPAD) (Levison et al. 2012), an N-body code, was deployed, which utilizes statistical algorithms to follow a large number of particles represented by tracers. As a result of oligarchic growth, the simulations generally form hundreds of $\sim M_\oplus$ bodies at $4 - 10$ au but further growth is halted due to gravitational scattering. The scattered oligarchs also pollute the inner Solar System with water and disrupt the outer Solar System.

To produce a Solar System analogue, the later work by Levison et al. (2015) modifies the pebble formation model that the pebble formation timescale is lengthened to ~ 1 Myr. This allows viscous stirring among planetesimals, which is on a shorter timescale compared to the growth timescale through pebble accretion. The less massive planetesimals are excited to orbit with higher inclinations. As the pebble density is lower farther away from the midplane of the disc, these inclined planetesimals are then starved of pebbles. This scenario yielded $1-4$ planets at $5 - 15$ au from the Sun without a stage of oligarchic growth. However, as noted in their work, gas accretion was cut off arbitrarily once the planet reaches the Jupiter mass M_J, instead of employing physical laws to stall the growth. Also, the embryos started to accrete gas in the simulations at around 8 Myr. The adopted gas accretion rate is likely unrealistically high as the disc has only $\sim 4\%$ of its initial surface density at this age in their model, which results in a generous gas accretion rate. Finally, planet migration, which puts a critical time constraint on planet formation, was not considered in the model either.

Matsumura et al. (2017), in turn, employed the Symplectic Massive Body Algorithm (SyMBA) (Duncan et al. 1998), a direct N-body code, with modifications to include pebble accretion, planet migration and gas accretion. They explored the dependence on stellar metallicity, stellar accretion rate and the viscosity parameter of the disc. Without migration, $1 - 3$ gas giants are formed at a few au in younger and less viscous discs. However, at the end of their 50 Myr simulations with migration, none of the results is consistent with the Solar System, as there are no giant planets left beyond 1 au. This shows that planet migration plays a crucial role in planet formation. Another major difference between the works by Levison et al. (2015) and Matsumura et al. (2017) is the number of particles simulated. Levison et al. (2015) use LIPAD, which simulates a large population of particles employing a statistical algorithm making viscous stirring among planetesimals possible. They also focused on growing gas giant analogous to the Solar System, and the domain of simulation is 4 – 15 au. In contrast, Matsumura et al. (2017) focus on the production of the observed exoplanetary systems, and the domain of simulation is 0.3 – 5 au instead.

More recently, Bitsch et al. (2019) adopt the slower migration prescription in the high-mass regime by Kanagawa et al. (2018). They employ the pebble and N-body code FLINTSTONE that also includes planet migration, eccentricity and inclination damping, as well as disc evolution. Their results show that with higher pebble mass flux and reduced planet migration rate, gas giants can indeed survive at wide orbits; with the final semimajor axes sensitive to the pebble mass flux and planet migration rate. Also, some of the resulting gas giants undergo scattering close to the Sun and end at a few au from the Sun. However, in these simulations, there are also other planets of a few to tens of $M_\oplus$ that migrate into the inner disc with less than 1 au, in contrast to the Solar System. Similarly, Matsumura et al. (2021) is able to form cold giant planets but cannot simultaneously avoid massive planetary cores migrating into the inner Solar System.

These works incorporating pebble accretion into global N-body simulations show intriguing results that the formation of gas accreting cores is possible through pebble accretion. Yet, further investigations are required to produce results that are consistent with the Solar System. The present study aims at assembling the giant planets analogous to those in the Solar System. In contrast to previous N-body planet formation models (e.g. Matsumura et al. 2017; Bitsch et al. 2019; Matsumura et al. 2021) that focus on a small number of lunar-mass embryos, we assume an initial planetesimal disc with planetesimal sizes comparable to those formed via the gravitational collapse induced by streaming instability. This is made computationally possible by employing SyMBA parallelized (SyMBAp) (Lau & Lee 2023), which is a parallelized version of SyMBA. In the following, Sect. 3.2 presents the methodology adopted in this work and the results are presented in Sect. 3.3. The discussion of the results, the implications and caveats are in Sect. 3.4.

3.2 Method

We generally follow the model by Matsumura et al. (2017) where additional subroutines are coupled with the symplectic direct N-body algorithm SyMBA (Duncan et al. 1998) to study planet formation in a protoplanetary disc. To facilitate the integration of a self-gravitating planetesimal disc in this work, we instead employ SyMBAp (Lau & Lee 2023). Further improvements are also made on the models of pebble accretion, gas accretion and the transition to the high-mass regime of planet migration. The following includes a summary of various parts of the model and the modifications made in this work are described in detail.

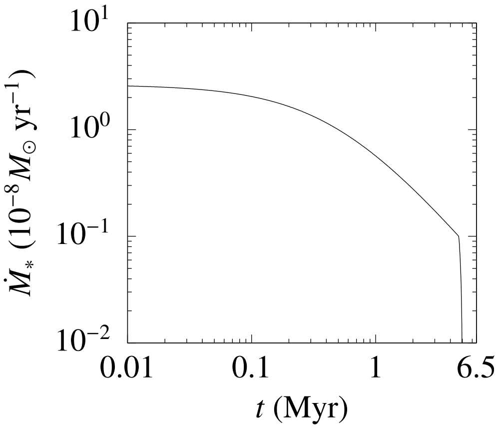

Figure 3.1: Time evolution of $\dot{M}_*$ with the initial age of the disc $t_0 = 0.5$ Myr. The value of $\dot{M}_*$ is turned down linearly when it drops below $10^{-9} M_\odot\,\mathrm{yr}^{-1}$ to mimic the effect of photoevaporation.

3.2.1 Disc model

We consider an axisymmetric protoplanetary disc around a Solar-type star of $1 M_\odot$ in mass and $1 L_\odot$ in luminosity undergoing steady gas accretion. The gas accretion rate can be expressed as

$$\dot{M}_* = 3\pi\Sigma_\mathrm{g}\nu \tag{3.1}$$

with Σ_g the gas surface density. For the viscosity ν, the Shakura & Sunyaev (1973) α-parametrization is adopted such that

$$\nu = \alpha_\mathrm{acc} c_\mathrm{s} H_\mathrm{g} \tag{3.2}$$

with the viscosity parameter $\alpha_\mathrm{acc} = 10^{-3}$ set in this work. The isothermal sound speed is used and given by $c_\mathrm{s} = \sqrt{k_\mathrm{B} T/\mu}$ with the Boltzmann constant k_B, the disc midplane temperature T, the mean molecular weight of the gas $\mu = 2.34 m_\mathrm{H}$, and the hydrogen mass $m_\mathrm{H} = 1.67 \times 10^{-27}$ kg. The gas disc scale height H_g is defined by $H_\mathrm{g} \equiv c_\mathrm{s}/\Omega_\mathrm{K}$, where the local Keplerian orbital frequency $\Omega_\mathrm{K} = \sqrt{GM_*/r^3}$ with the gravitational constant G, the mass of the central star M_*, and the distance from the star r. Following Hartmann et al. (1998), the evolution of the disc is propagated from the modulation of the stellar accretion rate by

$$\log\left(\frac{\dot{M}_*}{10^{-8} M_\odot\ \mathrm{yr}^{-1}}\right) = -1.4 \log\left(\frac{t + t_0}{\mathrm{Myr}}\right) \tag{3.3}$$

with the time since the start of the simulation t and the initial age of the disc $t_0 = 0.5$ Myr. Fig. 3.1 shows the time evolution of $\dot{M}_*$. When $\dot{M}_*$ drops below $10^{-9} M_\odot\,\mathrm{yr}^{-1}$, $\dot{M}_*$ is linearly turned down to zero at $t + t_0 = 5.5$ Myr to mimic the effect of photoevaporation following Matsumura et al. (2017). With this setup, the initial stellar accretion rate is about $2.64 \times 10^{-8} M_\odot$ yr^{-1} and reaches $10^{-9} M_\odot\,\mathrm{yr}^{-1}$ when $t \approx 4.68$ Myr.

In general, the inner part of the disc is dominated by viscous heating and the outer part is dominated by radiative heating. Since this work focuses on the formation of the giant planets in the Solar System, only radiative heating is considered for the disc, in contrast to the disc

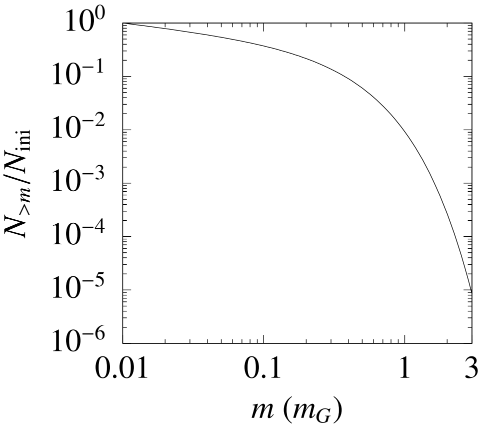

Figure 3.2: Adopted truncated power law initial planetesimal mass function as described by Eq. (3.8) based on Abod et al. (2019). It is presented in the unit of the planetesimal gravitational mass m_G.

model in Matsumura et al. (2017, 2021) where viscous heating is also considered. The midplane temperature profile of the disc T is given by (Oka et al. 2011)

$$T = 150 \left(\frac{r}{\rm au}\right)^{-3/7} \text{K}. \tag{3.4}$$

This setup yields the reduced disc scale height profile

$$\hat{h}_{\rm g} \equiv \frac{H_{\rm g}}{r} \approx 0.024 \left(\frac{r}{\rm au}\right)^{2/7}. \tag{3.5}$$

With Eq. (3.1) for the gas accretion rate, Eq. (3.2) for the α-parametrization, and Eq. (3.3) for the evolution of the stellar accretion rate, Eqs. (3.4) and (3.5) yield the gas surface density in the radiatively heated region

$$\Sigma_{\rm g} \approx 2.7 \times 10^3 \left(\frac{\alpha_{\rm acc}}{10^{-3}}\right)^{-1} \frac{\dot{M}_*}{10^{-8} M_\odot \text{ yr}^{-1}} \left(\frac{r}{\rm au}\right)^{-15/14} \text{g cm}^{-2}. \tag{3.6}$$

This disc model yields a profile of the midplane pressure gradient parameter, where P is the midplane gas pressure,

$$\begin{aligned} \eta &\equiv -\frac{\hat{h}_{\rm g}^2}{2} \frac{\partial \ln P}{\partial \ln r} \\ &\approx 8.02 \times 10^{-4} \left(\frac{r}{\rm au}\right)^{4/7}. \end{aligned} \tag{3.7}$$

3.2.2 Planetesimal disc

Instead of starting with lunar mass embryos as in Matsumura et al. (2017), a planetesimal disc is generated from 5−20 au initially with an initial mass function implemented in a manner similar to

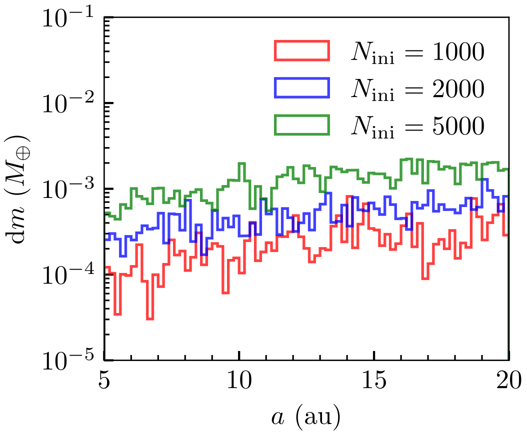

Figure 3.3: Initial mass distribution of the realized planetesimal discs. One example is shown for each of the chosen values of $N_{\rm ini}$. The width of each bin is 0.2 au.

Lau et al. (2022) as summarized in the following. Planetesimals are drawn from the cumulative mass distribution in the work on planetesimal formation by Abod et al. (2019), which has the form of an exponentially truncated power law. The number fraction of planetesimals above mass m is given by

$$\frac{N_{>m}}{N_{\rm ini}} = \left(\frac{m}{m_{\rm min}}\right)^{-0.3} \exp\left(\frac{m_{\rm min} - m}{0.3 m_G}\right), \tag{3.8}$$

for $m \geq m_{\rm min}$, with $m_{\rm min}$ being the minimum planetesimal mass considered, $N_{>m}$ is the number of particles with a mass $> m$, $N_{\rm ini}$ is the initial number of particles, and m_G is a planetesimal gravitational mass. We have set $m_{\rm min} = 10^{-2} m_G$ in this work, which is well below the peak of the distribution of the planetesimal mass in each logarithm mass bin as noted by Lau et al. (2022). The upper limit of m is also artificially set at $3m_G$ in the realization algorithm to avoid a mathematical singularity. This value is an order of magnitude larger than the characteristic mass of the initial mass function ($0.3m_G$), where Abod et al. (2019) also show that the maximum planetesimal mass is about an order of magnitude more massive than the characteristic mass. In this manner, only an insignificant number of massive planetesimals ($\sim 8 \times 10^{-6} N_{\rm ini}$) is lost. The form of the cumulative mass function is shown in Fig. 3.2.

For m_G, we adopt the critical mass for gravitational collapse of a dust clump in the presence of turbulent diffusion by Klahr & Schreiber (2020), which is given by

$$\begin{aligned} m_G &= \frac{1}{9}\left(\frac{\delta}{\rm St}\right)^{3/2} \hat{h}_{\rm g}^3 M_\odot \\ &\approx 5.78 \times 10^{-4} \left(\frac{\delta}{10^{-5}}\right)^{3/2} \left(\frac{\rm St}{10^{-2}}\right)^{-3/2} \left(\frac{\hat{h}_{\rm g}}{0.038}\right)^{3} M_\oplus \end{aligned} \tag{3.9}$$

where δ is the small-scale diffusion parameter, which is independent of $\alpha_{\rm acc}$, and St is the Stokes number. In this work, we set $\delta = 10^{-5}$ and $\mathrm{St} = 10^{-2}$ exclusively for planetesimal realization.

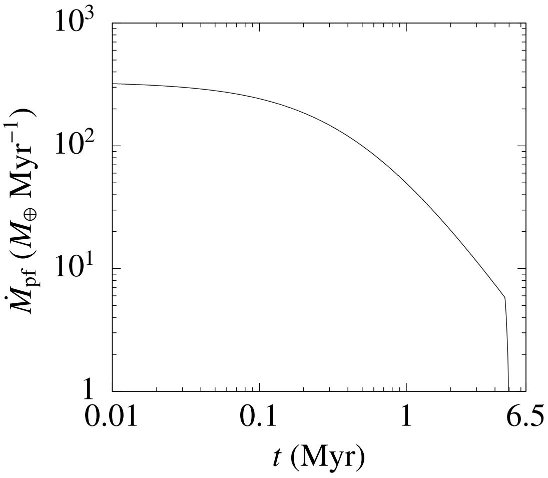

Figure 3.4: Time evolution of the pebble mass flux $\dot{M}_{\mathrm{pf}}$ given by Eq. (3.11) with $Z_0 = 10^{-2}$ and $\alpha_{\mathrm{acc}} = 10^{-3}$ as set in this work.

While the strength of the small-scale diffusion is an active research topic in the field, the adopted value is motivated by the measurements of local diffusivity of dust particles in streaming instability presented in Schreiber & Klahr (2018).

In each simulation, the semimajor axis a of a new planetesimal is randomly drawn from $5-20$ au, which implies a surface number density of planetesimals that scales with $1/r$. The value of m_G is then evaluated with the local disc scale height. Afterwards, the mass m of this planetesimal is drawn from the mass function given by Eq. (3.8) with the chosen value of N_{ini} noted later in Sect. 3.2.6. Figure 3.3 shows the initial mass distributions of the realized planetesimal discs with one example shown for each of the chosen values of N_{ini}. The eccentricity e is randomly drawn from a Rayleigh distribution with the scale parameter 10^{-6}. The inclination i in radian is also drawn from a Rayleigh distribution but with the scale parameter 5×10^{-7} instead. Other angles of the orbital elements are drawn randomly from 0 to 2π. The physical radius R_{p} is calculated by assuming an internal density $\rho_{\mathrm{s}} = 1.5$ g cm^{-3}. The realization process repeats until the total number of planetesimals reaches the chosen value. The planetesimals are then evolved under full gravitational interactions between themselves and the central star, as well as additional effects of pebble accretion (Sect. 3.2.3), gas accretion (Sect. 3.2.4) and planet-disc interactions (Sect. 3.2.5).

3.2.3 Pebble accretion

We implement the ‘pebble formation front’ model (Lambrechts & Johansen 2014) to estimate the pebble mass flux $\dot{m}_{\mathrm{peb}}$. As dust particles coagulate and grow into pebbles, their velocities are strongly influenced by the headwind. This causes a significantly inward drift of pebbles that provide a solid mass flux to the inner part of the disc. Since the dust growth timescale increases with radius in general, the source of the pebble mass flux, or the pebble formation front, evolves outwards in time. The location of the pebble formation front r_{pf} is given by (Lambrechts &

Johansen 2014)

$$r_{\mathrm{pf}}(t) = \left(\frac{3}{16}\right)^{1/3} (GM_*)^{1/3}(\epsilon_{\mathrm{d}}Z_0)^{2/3}t^{2/3} \tag{3.10}$$

with the initial dust-to-gas ratio Z_0 and the particle growth parameter $\epsilon_{\mathrm{d}} = 0.05$. The pebble mass flux $\dot{M}_{\mathrm{pf}}$ is then calculated from the dust mass swept across by the pebble formation front per unit time, that is,

$$\begin{aligned}\dot{M}_{\mathrm{pf}} &= 2\pi r_{\mathrm{pf}} Z_0 \Sigma_{\mathrm{g}}(r_{\mathrm{pf}})\dot{r}_{\mathrm{pf}} \\ &\approx \frac{\dot{M}_*}{10^{-8}M_\odot\ \mathrm{yr}^{-1}} \left(\frac{Z_0}{10^{-2}}\right)^{5/3} \left(\frac{\alpha_{\mathrm{acc}}}{10^{-3}}\right)^{-1} \times \\ &\left(\frac{t+t_0}{\mathrm{Myr}}\right)^{-1/3} 10^2 M_\oplus\ \mathrm{Myr}^{-1}.\end{aligned} \tag{3.11}$$

A factor of $r_{\mathrm{pf}}^{-1/14}$ is omitted for simplicity. We set $Z_0 = 10^{-2}$ in this work and Fig. 3.4 shows the time evolution of $\dot{M}_{\mathrm{pf}}$ for the chosen parameters. We note that at 4.5 Myr, briefly before disc dispersal, $r_{\mathrm{pf}} \approx 350$ au. This is comparable to the typical observed disc sizes, which is of the order of 100 au (e.g. Andrews et al. 2018; Long et al. 2018; Cieza et al. 2021). In Matsumura et al. (2017), $\dot{M}_{\mathrm{pf}}$ is halved inside of the snow line. However, this treatment is not implemented in the present work as it focuses on the outer Solar System where particles are removed before they can reach the ice line in our model. The radial domain of this work is summarized later in Sect. 3.2.6. On the other hand, we follow Matsumura et al. (2021) and adopt the pebble disc scale height given by

$$H_{\mathrm{peb}} = \left(1 + \frac{\mathrm{St}}{\alpha_{\mathrm{turb}}}\right)^{-1/2} H_{\mathrm{g}} \tag{3.12}$$

with the Stokes number of pebble St. Following Ida et al. (2018), an α_{turb} parameter is introduced, which is about an order of magnitude smaller than α_{acc} as evaluated by Hasegawa et al. (2017). The latter is distinct from that in the classical α-parametrization, i.e. the α_{acc} parameter introduced in Sect. 3.2.1. In this work, we set $\alpha_{\mathrm{turb}}/\alpha_{\mathrm{acc}} = 0.1$. The α_{turb} parameter is also used for prescribing gas accretion (Sect. 3.2.4) and planet-disc interactions (Sect. 3.2.5) as described in the respective sub-sections.

Furthermore, the pebble flux available to each body is subtracted by the total pebble accretion rate of the superior bodies that are farther from the central star, if there are any. We define a pebble accretion efficiency ϵ_{PA} such that the growth rate of a body i by pebble accretion is given by

$$\dot{m}_{\mathrm{PA},i} = \epsilon_{\mathrm{PA}} \max\left(\dot{M}_{\mathrm{pf}} - \sum_{n=i+1}^{N} \dot{m}_{\mathrm{PA},n}, 0\right), \tag{3.13}$$

where bodies $(i+1)$ to N are all the superior ones.

In this work, we also compare the pebble accretion efficiency of Ida et al. (2016) with modifications by Matsumura et al. (2021), $\epsilon_{\mathrm{IGM16}}$, and that by Liu & Ormel (2018) and Ormel & Liu (2018), ϵ_{OL18}. In the derivation of $\epsilon_{\mathrm{IGM16}}$, the pebble-accreting body is assumed to be in a circular orbit as noted in Sect. 3.2 of Ida et al. (2016) and shown in Eq. (33) of their work regarding the pebble relative velocity. In contrast, Liu & Ormel (2018) and Ormel & Liu (2018) do not hold this assumption, and both the inclination and the eccentricity of the pebble-accreting body contribute to the pebble relative velocity. The modifications of $\epsilon_{\rm IGM16}$ made by Matsumura et al. (2021) considered the inclination of the body. However, it only plays a role in the calculation of the pebble volume density as shown in Eq. (32) of their work but not in the calculation of the pebble relative velocity. The differences between the two pebble accretion prescriptions and the consequences are further discussed in Sect. 3.4.1.

When the planetesimals grow into massive cores, the process of pebble isolation occurs when they perturb the gas surface density profile and stop pebbles from reaching the planet itself as well as the inferior bodies that are closer to the central star, if there are any. We follow the assumption in Matsumura et al. (2017) that the required mass, which is often called the 'pebble isolation mass', is given by

$$\begin{aligned} m_{\rm iso} &= \frac{1}{2}\hat{h}_{\rm g}^{3} M_{*} \\ &\approx 9.14 \left(\frac{\hat{h}_{\rm g}}{0.038} \right)^{3} M_{\oplus}. \end{aligned} \tag{3.14}$$

Once any planet reaches this mass, pebble accretion is stopped for this planet and all the inferior ones if there are any.

3.2.4 Gas accretion

When a massive core has formed and its solid accretion rate is low, gas can contract and form an envelope. We follow Ikoma et al. (2000) for the critical mass for runaway gas accretion, which is given by, for planet i,

$$m_{\rm g,crit} = 10 \left(\frac{\dot{m}_{{\rm PA},i}}{10^{-6} M_{\oplus}\ {\rm yr}^{-1}} \frac{\kappa}{1\ {\rm cm}^{2}\ {\rm g}^{-1}} \right)^{p} M_{\oplus}. \tag{3.15}$$

In this work, we set the parameter $p = 0.25$ (Ida & Lin 2004) and the envelope opacity $\kappa = 1\ {\rm cm}^2\ {\rm g}^{-1}$. For cores that have reached this mass, we assume the gas envelope collapses on the Kelvin-Helmholtz timescale $\tau_{\rm KH}$ given by (Ikoma et al. 2000; Ida & Lin 2004)

$$\tau_{\rm KH} = 10^{9} \left(\frac{m}{M_{\oplus}} \right)^{-3} \left(\frac{\kappa}{1\ {\rm cm}^{2}\ {\rm g}^{-1}} \right) {\rm yr}. \tag{3.16}$$

There are two factors that limit the actual gas accretion rate considered in our model. First, the gas supply is limited by the stellar accretion rate as well as the gas accreted by the superior planets. Also, gap opening by the planet shall further limit the gas accretion rate. And, we assume gas accretion is exponentially cutoff when the planet's Hill radius equals the local disc scale height, which is given by $m_{\rm Hill} = 3M_{*}\hat{h}_{\rm g}^{3}$. These can be summarized as the expression for the gas accretion rate of planet i

$$\dot{m}_{\mathrm{g},i} = \min\left[\frac{m}{\tau_{\mathrm{KH}}}, \max\left(\dot{M}_* - \sum_{n=i+1}^{N} \dot{m}_{\mathrm{g},n}\ , 0\right) f_{\mathrm{local}} \exp\left(-\frac{m}{m_{\mathrm{Hill}}}\right)\right] \tag{3.17}$$

where planets $(i+1)$ to N are all the superior ones and the reduction factor f_{local} is given by (Ida et al. 2018)

$$f_{\mathrm{local}} = \frac{0.0308 \hat{h}_{\mathrm{g}}^{-4} (m/M_*)^{4/3} \alpha_{\mathrm{acc}}^{-1}}{1 + 0.04K}. \tag{3.18}$$

The gap opening factor K is given by Eq. (3.24) in the next subsection (Sect. 3.2.5).

3.2.5 Planet-disc interactions

Other than the N-body gravitational interactions, the bodies also experience the torques due to the planet-disc interactions. We adopt the prescription based on dynamical friction by Ida et al. (2020) and the transition from the low-mass to the high-mass regime by Ida et al. (2018) based on the gap opening factor K by Kanagawa et al. (2015b). The timescales for the non-isothermal case and finite inclination i, while $i < \hat{h}_{\mathrm{g}}$, (Appendix C and D of Ida et al. 2020 and Matsumura et al. 2021) are implemented. The evolution timescales of semimajor axis, eccentricity and inclination are defined respectively by

$$\tau_a \equiv -\frac{a}{\mathrm{d}a/\mathrm{d}t}, \tau_e \equiv -\frac{e}{\mathrm{d}e/\mathrm{d}t}, \tau_i \equiv -\frac{i}{\mathrm{d}i/\mathrm{d}t}. \tag{3.19}$$

These timescales are given by

$$\tau_a = \frac{t'_{\mathrm{wav}}}{2\hat{h}_{\mathrm{g}}^2}\left[\frac{\Gamma_L}{\Gamma_0}\left(1 - \frac{1}{C_{\mathrm{M}}}\frac{\Gamma_L}{\Gamma_0}\sqrt{\hat{e}^2 + \hat{i}^2}\right)^{-1} + \frac{\Gamma_C}{\Gamma_0}\exp\left(-\frac{\sqrt{\hat{e}^2 + \hat{i}^2}}{e_{\mathrm{f}}}\right)\right]^{-1}, \tag{3.20}$$

$$\tau_e = 1.282 t'_{\mathrm{wav}}\left[1 + \frac{(\hat{e}^2 + \hat{i}^2)^{3/2}}{15}\right], \tag{3.21}$$

$$\tau_i = 1.838 t'_{\mathrm{wav}}\left[1 + \frac{(\hat{e}^2 + \hat{i}^2)^{3/2}}{21.5}\right], \tag{3.22}$$

where $\hat{e} \equiv e/\hat{h}_{\mathrm{g}}$, $\hat{i} \equiv i/\hat{h}_{\mathrm{g}}$, and we follow Fendyke & Nelson (2014) for the factor $e_{\mathrm{f}} = 0.01 + \hat{h}_{\mathrm{g}}/2$. The normalized Lindblad torque Γ_L/Γ_0 and corotation torque Γ_C/Γ_0 are described in detail by

Paardekooper et al. (2011). The characteristic time including the transition to the high-mass regime $t'_{\rm wav}$ (Tanaka et al. 2002; Ida et al. 2018) is given by

$$t'_{\rm wav} = \left(\frac{M_*}{m}\right)\left(\frac{M_*}{\Sigma_{\rm g} r^2}\right)\left(\frac{\hat{h}_{\rm g}^4}{\Omega_{\rm K}}\right)(1 + 0.04K) \tag{3.23}$$

with the gap opening factor K given by

$$K = \left(\frac{m}{M_*}\right)^2 \hat{h}_{\rm g}^{-5}\alpha_{\rm turb}^{-1}. \tag{3.24}$$

As noted in Lau et al. (2022), it is more suitable to evaluate the value of $\Omega_{\rm K}$ at the instantaneous distance from the star r of the body instead of its semimajor axis a in N-body simulations with large number of particles due to potential frequent encounters. We follow Ida et al. (2018) and introduce the $\alpha_{\rm turb}$ parameter set to $\alpha_{\rm turb}/\alpha_{\rm acc} = 0.1$ as described in Sect. 3.2.3. The three timescales are applied to the equation of motion

$$\boldsymbol{a} = -\frac{v_{\rm K} \cdot S_a}{2\tau_a}\boldsymbol{e}_\theta - \frac{v_r}{\tau_e}\boldsymbol{e}_r - \frac{v_\theta - v_{\rm K}}{\tau_e}\boldsymbol{e}_\theta - \frac{v_z}{\tau_i}\boldsymbol{e}_z \tag{3.25}$$

in the cylindrical coordinates (r, θ, z) with the velocity of the embryo $\boldsymbol{v} = (v_r, v_\theta, v_z)$ and the local Keplerian velocity $v_{\rm K} = r\Omega_{\rm K}$. A switch for planet migration S_a is introduced to toggle the evolution of the semimajor axis, which is turned off and on respectively by setting S_a to 0 and 1 in this work.

3.2.6 Numerical setups

To explore the dependence on the total number of planetesimals, three values of $N_{\rm ini} = \{1000, 2000, 5000\}$ are chosen. They translate respectively to a total planetesimal mass of about $\{0.02, 0.04, 0.1\}M_\oplus$. We test two pebble accretion efficiency prescriptions $\epsilon_{\rm PA} = \{\epsilon_{\rm IGM16}, \epsilon_{\rm OL18}\}$ described in Sect. 3.2.3 and the two states of $S_a = \{0, 1\}$ described in Sect. 3.2.5 that switches off or on the evolution of semimajor axis due to planet-disc interactions. Each simulation lasts for 6.5 Myr to allow for further dynamical evolution due to gravitational interactions after disc dispersal. Particles are removed if the heliocentric distance is less than 1 au or greater than 100 au. For each combination of the parameters, we conduct five simulations to sample the stochastic variations in the outcome. Thus a total of 60 simulations are conducted in this work and presented in the next section.

3.3 Results

The first part of this section (Sect. 3.3.1) presents the results with migration turned off, i.e. $S_a = 0$, followed by Sect. 3.3.2 where the results with migration turned on, i.e. $S_a = 1$, is presented.

3.3.1 Simulations without planet migration ($S_a = 0$)

Pebble accretion efficiency $\epsilon_{\rm PA} = \epsilon_{\rm IGM16}$

Figure 3.5 shows the results for $N_{\rm ini} = 1000$, $S_a = 0$ and $\epsilon_{\rm PA} = \epsilon_{\rm IGM16}$. Each row presents a snapshot of the simulations at $t = \{0.10, 0.75, 2.50, 4.00, 6.50\}$ Myr respectively. For the first three columns from the left, the total occurrences of particles across all five simulations are shown by heat maps. The left-most column shows the mass m in $M_\oplus$ and the semimajor axis a. The next two columns to the right show the eccentricity e and inclination i against m respectively. The right-most column shows the differential mass distribution of the particles with each colour corresponds to one of the five simulations. Particles in one of the five simulations (blue) is also plotted with particles above $10^{-3}M_\oplus$ denoted by enlarged dots. For the last row (6.5 Myr), which shows the end results, particles above $10^{-3}M_\oplus$ in all simulations are shown individually (with a different colour for each simulation) without using heat maps.

The m–a plots show a rapid growth by pebble accretion in the inner part of the disc in the first 0.1 Myr of the simulations. Some planetesimals in the massive tail of the distribution have grown by more than 3 orders of magnitude dominantly by pebble accretion. The growth rate has a strong dependence on the distance from the star, and particles closer to the central star accrete pebble much faster, as predicted by Ida et al. (2016). This is also consistent with the analysis which includes both pebble and planetesimal accretion in Coleman (2021), though our simulations focus on the outer Solar System.

The e–m plots and the i–m plots show the early and fast growing bodies quickly heat up their neighbouring planetesimals from the beginning of the simulations to 0.75 Myr, increasing the eccentricities and inclinations of neighbouring planetesimals. The massive cores of $\sim M_\oplus$ stop further growth of the neighbouring smaller bodies by viscous stirring, with about 20 bodies having reached $\sim 1 - 10M_\oplus$ by 0.75 Myr. This effect of viscous stirring on pebble accretion is consistent with Levison et al. (2015) and further discussed in Sect. 3.4.1. The e and i of these cores are also damped and remain low in contrast to those of the smaller bodies, which allows these massive bodies to further increase in mass due to the proximity to the dense pebble disc. This effect is more noticeable from the differential mass distributions, i.e. the rightmost column, that only the particles in the massive tail of the initial planetesimal population can grow significantly while the rest remain about the same mass. The growth of these massive bodies is drastically different from the traditional oligarchic growth scenario, where the growth is slowed down by viscous heating that clears nearby planetesimals. Here, the more massive bodies can continue growth via pebble accretion until reaching the pebble isolation mass, which is a result of the perturbations to the gas disc.

As the simulations progress forward, the massive cores grow further by gas accretion and eject most of the small bodies from $0.75 - 4$ Myr. At the end of the simulations, i.e. $t = 6.50$ Myr, some of the massive cores and gas giants ($m > 10^2M_\oplus$) formed have been ejected, and $1-4$ gas giants remain but their locations vary greatly across the simulations. This indicates a strong stochastic behaviour due to dynamical instabilities that result from the formation of multiple gas giants in a short range of distance from the star. Also, ice giants ($m \sim 10M_\oplus$) do not survive in any of these simulations: they either became gas giants or were scattered out of the system by

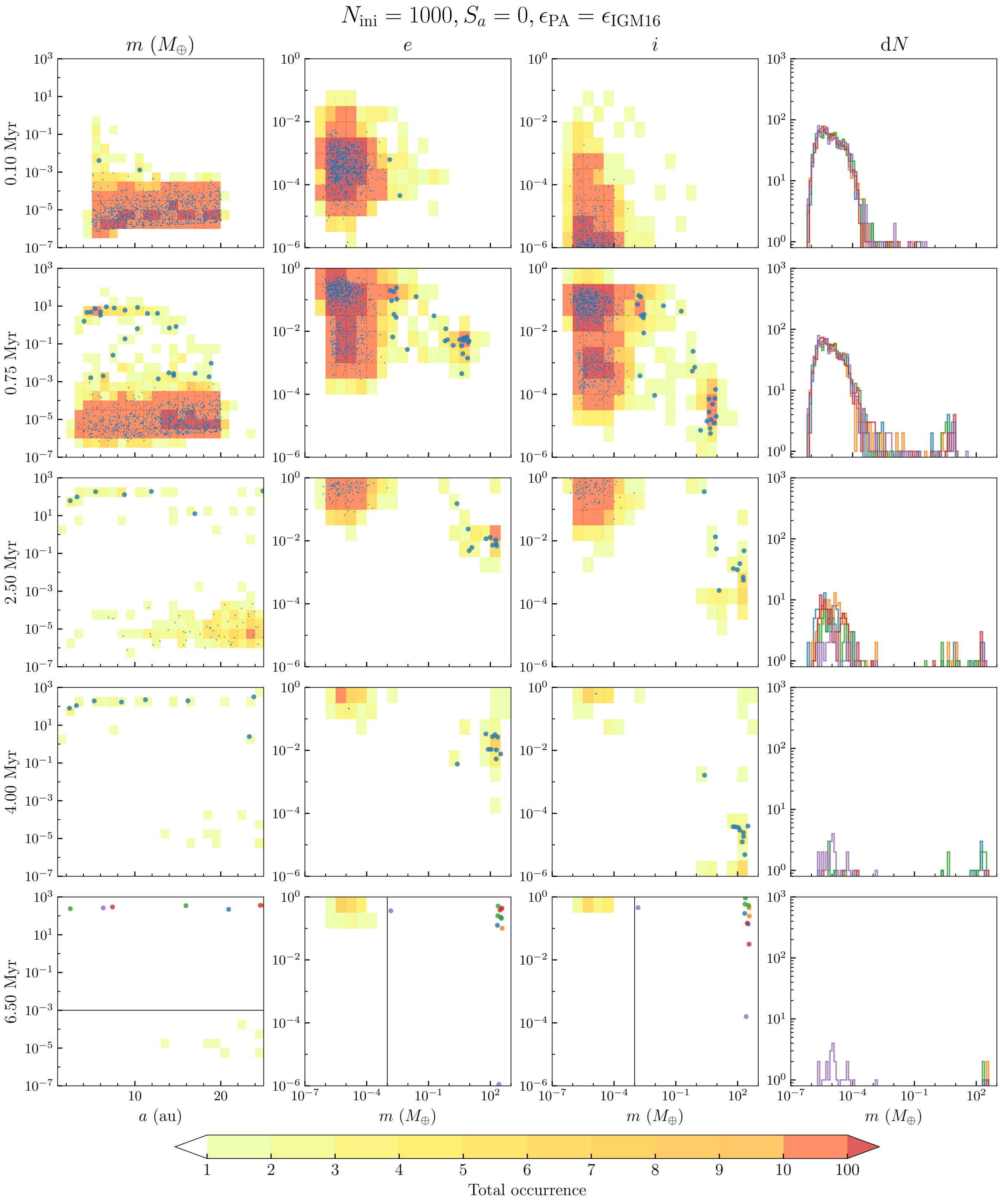

Figure 3.5: Results for the simulations with $N_{\rm ini} = 1000$, migration turned off ($S_a = 0$), and the pebble accretion efficiency $\epsilon_{\rm PA} = \epsilon_{\rm IGM16}$. Each row presents a snapshot of the simulations at the time indicated by the timestamp on the left. For the first three columns from the left, the total occurrences of particles across all five random simulations are shown by heat maps with 2×2 cells in each minor axis grid cell. The left-most column shows m and a. The next two columns to the right respectively shows the e and i, respectively, against a. The right-most column shows the differential mass distribution of all bodies with each colour corresponds to one of the five simulations. Particles in one of the five simulations (blue) is also plotted with enlarged dots denoting particles above $10^{-3} M_\oplus$. For 6.5 Myr, i.e. the end of the simulations, particles above $10^{-3} M_\oplus$ in all five simulations are shown individually without using heat maps. Further descriptions are in the text.

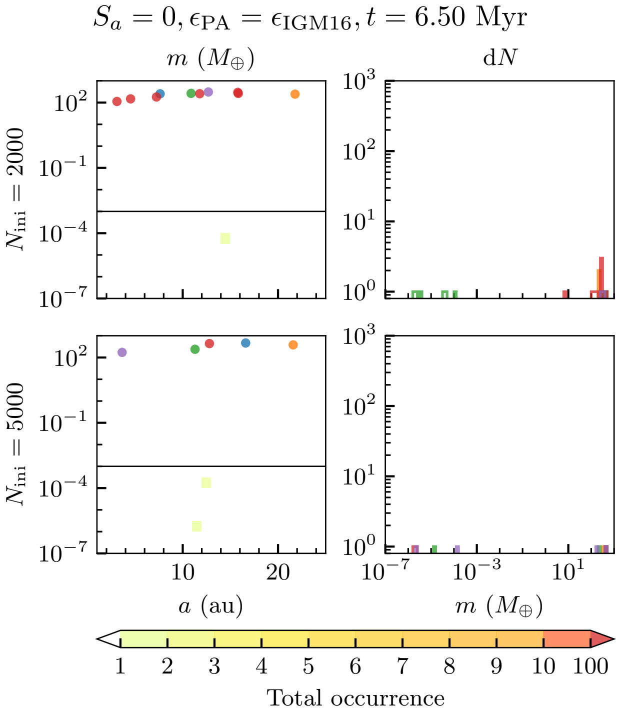

Figure 3.6: End results for the simulations with $N_{\rm ini}$ = 2000 and 5000, respectively, as indicated on the left, migration turned off (S_a = 0), and the pebble accretion efficiency $\epsilon_{\rm PA}$ = $\epsilon_{\rm IGM16}$. The two columns here correspond to the left-most and the right most columns of Fig. 3.5, respectively. There is no qualitative difference in the end results among the simulations with the chosen set of $N_{\rm ini}$ = {1000, 2000, 5000}.

other giants. On the other hand, the results with $N_{\mathrm{ini}} = 2000$ and 5000 do not show any qualitative difference from the presented results with $N_{\mathrm{ini}} = 1000$ (Fig. 3.6).

Pebble accretion efficiency $\epsilon_{\mathrm{PA}} = \epsilon_{\mathrm{OL18}}$

Figure 3.7 shows the results for $N_{\mathrm{ini}} = 1000$, $S_a = 0$ and $\epsilon_{\mathrm{PA}} = \epsilon_{\mathrm{OL18}}$. Compared to the results for $\epsilon_{\mathrm{PA}} = \epsilon_{\mathrm{IGM16}}$, the growth by pebble accretion is generally slower, but still rapid. Some planetesimals grow by up to about 2 orders of magnitude in mass in the first 0.1 Myr and massive cores ($m \sim M_\oplus$) are formed at 0.75 Myr. At 2.5 Myr, the massive cores in the inner part of the disc ($\sim 5 - 10$ au) have reached the local pebble isolation mass and gas accretion begins with less than ~ 10 bodies having gained mass between the $\sim 10M_\oplus$ cores and the initial planetesimals. In the previous simulations (Fig. 3.5), this stage is reached at 0.75 Myr. This delay is caused by the change in the adopted pebble accretion efficiency ϵ_{PA}, where $\epsilon_{\mathrm{IGM16}}$ is more efficient than ϵ_{OL18} as also shown in Matsumura et al. (2021). A comparison between the two efficiency prescriptions and the consequences are further discussed in Sect. 3.4.1. A more distinct dichotomy in mass is produced with $\epsilon_{\mathrm{PA}} = \epsilon_{\mathrm{OL18}}$ as shown by comparing the differential mass distribution in Fig. 3.5 for 0.75 Myr and that in Fig. 3.7 for 2.50 Myr. A more significant number of planetesimals has reached $\sim 10^{-3}M_\oplus$ in the former case while a sharper cut near the upper end ($\sim 10^{-4}M_\oplus$) of the initial distribution is shown in the latter case. At this stage, the intermediate-mass bodies between these two groups, which have mass of about $10^{-5} - 10^{-1}M_\oplus$, are generally dynamically colder, as shown by the *e–m* and *i–m* plots. As the simulations continue to 4.00 Myr, some bodies have become gas giants in the inner part of the disc, with some bodies of $\sim 1 - 10M_\oplus$ residing outside of 10 au, in contrast to the results shown in Fig. 3.5 at the same time.

At the end of the simulations, one to two gas giants and one to two ice giants are formed as well, which is the closest set of simulations in the work to reproduce the Solar System's giant planets. A significant number of the initial planetesimals remain, especially in the outer part of the disc at around 20 au. This is distinct from the results with $\epsilon_{\mathrm{PA}} = \epsilon_{\mathrm{IGM16}}$, where no ice giants are formed and most of the initial planetesimals have been scattered at the end of the simulations, probably due to the higher number of gas giants. Nonetheless, the locations of the leftover bodies still vary greatly across the simulations, so that the stochastic nature of the system remains.

Figure 3.8 shows the results for $N_{\mathrm{ini}} = 2000$ instead with the same pebble efficiency prescription. Compared to Fig. 3.7, the differential mass distribution shows that the massive tail extends for about twice as high in m. This leads to the formation of more massive cores in the subsequent evolution of the simulations. At the end of the simulations, more gas giants and fewer ice giants are formed in this case. Only two out of the five simulations has one to four ice giants, while this class of bodies is absent in the rest of the simulations. With $N_{\mathrm{ini}} = 5000$, shown in Fig. 3.9, only one simulation contains an ice giant at the end, which instead is located in the inner part of the disc at about 6 au. Here, we find a dependence on the value of N_{ini}, which is not present when $\epsilon_{\mathrm{PA}} = \epsilon_{\mathrm{IGM16}}$ (Sect. 3.3.1). This is likely caused by the difference in the rate of pebble accretion, which is further discussed in Sect. 3.4.1.

3.3.2 Simulations with planet migration ($S_a = 1$)

Figure 3.10 shows the results for $N_{\rm ini} = 1000$, with migration $S_a = 1$ and $\epsilon_{\rm PA} = \epsilon_{\rm IGM16}$. The snapshots of the *m–a* distribution show that once the cores reach $\sim M_\oplus$, they migrate inwards rapidly, even though $\alpha_{\rm turb}/\alpha_{\rm acc} = 0.1$. For the massive cores that grow from planetesimals in the inner part of the disc, they have moved out of the simulation domain before runaway gas accretion occurs. For the massive cores that remain by the end of the simulations, the depletion of the gas disc stops both the migration as well as gas accretion. As a result, only cores of a few $M_\oplus$ are formed and survive in the simulations. A large fraction of the initial planetesimal population remains at the end as they are not scattered due to the absence of giant planets. Similarly, Fig. 3.11 shows the results for $\epsilon_{\rm PA} = \epsilon_{\rm OL18}$ with $S_a = 1$ where only cores of a few $M_\oplus$ are formed and survive. These cores are slightly less massive in this case compared to Fig. 3.10. The results with $N_{\rm ini} = 2000$ and 5000 do not show any qualitative difference from this results with migration in effect. Since the massive cores migrate rapidly and none reach the runaway gas accretion phase by the end of the simulation, the dependence on $N_{\rm ini}$ shown in the case without planet migration for $\epsilon_{\rm PA} = \epsilon_{\rm OL18}$ (Sect. 3.3.1) is no longer present in this case here.

3.4 Discussions

3.4.1 Pebble accretion efficiency

Pebble accretion has been shown by the results of our model (Sect. 3.3) to be a promising way to grow planetesimals efficiently such that massive cores of $\sim 10 M_\oplus$ can form well before disc dispersal and accrete gas to become giant planets. Nonetheless, forming giant planets analogous to those in the Solar System still requires further modifications to the model. In the presented results without planet migration ($S_a = 0$), ice giants are formed only in the simulations with the pebble accretion efficiency prescription by Liu & Ormel (2018) and Ormel & Liu (2018), i.e. $\epsilon_{\rm PA} = \epsilon_{\rm OL18}$, as presented in Sect. 3.3.1. The ice giants in these simulations stop accreting gas because by the time they are massive enough to accrete a gaseous envelope the gas disc is dispersed. In contrast with $\epsilon_{\rm PA} = \epsilon_{\rm IGM16}$, as shown in Sect. 3.3.1, massive cores of $\sim 10 M_\oplus$ are formed much earlier and the giant planets have enough time to reach the prescribed final mass (Sect. 3.2.4) before disc dispersal. This shows that the timing of the formation of the massive cores and the start of gas accretion plays an important role in the final architecture of the planetary system.

As noted by Matsumura et al. (2021), $\epsilon_{\rm OL18}$ is generally a few times less efficient than $\epsilon_{\rm IGM16}$ for the adopted value of $\alpha_{\rm turb}$. And, in the present work, the simulations begin with a mass spectrum of planetesimals which spans over two decades in mass, up to $10^{-4} M_\oplus$, instead of lunar-mass embryos. This demonstrates the effect of the pebble accretion onset mass and the effect of viscous stirring on pebble accretion efficiency more clearly as discussed in the following.

Pebble accretion onset mass

First, we focus on the limit that the eccentricity e of the pebble-accreting body is much lower than the midplane pressure gradient parameter $\eta \sim 10^{-3}$. This is also an assumption held by Ida et al. (2016) in the derivation of the pebble accretion efficiency. Since we are considering the start of pebble accretion, the mass of the body is generally small and pebble accretion typically operates in the Bondi regime. In this case, the pebble relative velocity is determined by the headwind. For a high pebble relative velocity, the pebble encounter time is shortened so that pebbles may not be deflected enough from the gas streamline and not have enough time to settle onto the planetesimal. As such, the accretion is no longer in the settling regime. This reduction effect is captured in the pebble accretion efficiency prescription by Ida et al. (2016) as well as that by Liu & Ormel (2018) and Ormel & Liu (2018) but in slightly different manners.

Ida et al. (2016) adopt the reduction factor for the cross section in the settling regime of pebble accretion proposed by Ormel & Kobayashi (2012). This reduction factor is given by

$$\kappa_{\rm IGM16} = \exp\left[-\left(\frac{\rm St}{\min(2, {\rm St}_{\rm crit})}\right)^{0.65}\right] \tag{3.26}$$

with the critical Stokes number of pebble

$${\rm St}_{\rm crit} = \frac{4m}{\eta^3 M_*}. \tag{3.27}$$

A similar reduction factor is also found in Liu & Ormel (2018), which is given by

$$\kappa_{\rm OL18} = \exp\left[-\frac{1}{2}\left(\frac{\Delta v}{v_{\rm crit}}\right)^2\right] \tag{3.28}$$

with the pebble relative velocity Δv and the critical relative velocity

$$v_{\rm crit} = \left(\frac{m}{M_* {\rm St}}\right)^{1/3} v_K. \tag{3.29}$$

In the head wind regime, $\Delta v = \eta v_K$, and, with Eq. (3.28), the reduction factor can be expressed as

$$\kappa_{\rm OL18,hw} \approx \exp\left[-\left(\frac{\rm St}{0.707 \cdot {\rm St}_{\rm crit}}\right)^{2/3}\right] \tag{3.30}$$

for a more insightful comparison with $\kappa_{\rm IGM16}$ in Eq. (3.26). By inspection, the dependence on the planetesimal mass m is virtually identical for both cases when $m \lesssim 2 \times 10^{-4} M_\oplus$ for $\eta = 10^{-3}$, while a factor of about 0.707 is multiplied to m for $\kappa_{\rm OL18,hw}$. Figure 3.12 shows the values of $\kappa_{\rm IGM16}$ and $\kappa_{\rm OL18,hw}$ with an assumed $\rm St = 0.1$ and $r = 5$ au in our disc model. For $m \lesssim 10^{-5} M_\oplus$, $\kappa_{\rm OL18,hw}$ is generally a few times smaller than $\kappa_{\rm IGM16}$. This is in agreement with the findings by Matsumura et al. (2021) and the early stage of the presented simulation results. When the bodies are still dynamically cold, the growth by pebble accretion with $\epsilon_{\rm PA} = \epsilon_{\rm OL18}$ is generally slower.

While restricting the discussion in the headwind regime with small e, a pebble accretion onset mass $m_{\mathrm{PA,hw}}$ can be defined (Visser & Ormel 2016; Ormel 2017) by setting $\Delta v = v_{\mathrm{crit}}$, which yields

$$m_{\mathrm{PA,hw}} = \mathrm{St}\,\eta^3 M_*. \tag{3.31}$$

For $m = m_{\mathrm{PA,hw}}$, this means $\kappa_{\mathrm{OL18}} \approx 0.61$ and $\kappa_{\mathrm{IGM16}} \approx 0.67$. Figure 3.13 shows a comparison of $m_{\mathrm{PA,hw}}$ and the planetesimal gravitational mass of the adopted initial planetesimal mass function, m_G, at different locations of the disc. The increase with r for $m_{\mathrm{PA,hw}}$ is steeper than that for m_G. This is in agreement with the results that the growth by pebble accretion is faster in the inner part of the disc. Also, m_G is about $5-10$ times smaller than $m_{\mathrm{PA,hw}}$ from $5-20$ au. This means the massive tail of the planetesimal population overlaps with the mass range for the sharp cut off in the values of the reduction factors for both prescriptions (κ_{IGM16} & $\kappa_{\mathrm{OL18,hw}}$) as shown in Fig. 3.12. As a result, the randomness in the exact number of particles drawn near the top end of the distribution as well as that in their locations play a significant role to the final architecture of the modelled planetary systems.

This is more clearly shown by the difference in the results with $N_{\mathrm{ini}} = \{1000, 2000, 5000\}$ while all have $S_a = 0$ and $\epsilon_{\mathrm{PA}} = \epsilon_{\mathrm{OL18}}$. As the number of planetesimal increases, the largest drawn mass increases slightly as well due to the higher probability of getting at least one particle with such mass. This leads to an earlier formation of massive cores, which are more likely to become gas giants by the time of disc dispersal while fewer or no ice giants remain. Nonetheless, this effect is not observed with $\epsilon_{\mathrm{PA}} = \epsilon_{\mathrm{IGM16}}$ likely due to a generally more efficient pebble accretion such that gas accretion starts early for the massive cores with enough time to reach the mass of a gas giant even with $N_{\mathrm{ini}} = 1000$.

Although our results show an apparent dependence on the initial number of particles N_{ini}, we emphasize that this can be a result of a statistical artefact. With the adopted initial mass function by Abod et al. (2019), as shown in Eq. (3.8), there is no upper limit on the planetesimal mass. Although an artificial upper limit of 10 times of the characteristic mass is imposed, this limit has a negligible effect on the actual realized planetesimal populations, where only a number fraction of planetesimals of $\sim 8 \times 10^{-6}$ is lost. Therefore, the massive tail of the initial planetesimal population drawn in this manner has a dependence on the number of particles, which sets the normalization constant of the initial mass function. This means a physical upper limit of planetesimal mass (e.g. Gerbig & Li 2023) is needed to remove this artefact for future investigations. Nonetheless, our results show the upper end of the initial planetesimal population plays the most important role in growth by pebble accretion while the rest of the small planetesimals do not affect their growth significantly.

We note that in Lambrechts & Johansen (2012), the transition mass of an embryo m_{t} is defined as the mass at which the Hill radius is comparable to the Bondi radius, i.e.

$$m_{\mathrm{t}} = \sqrt{\frac{1}{3}\frac{(\eta v_{\mathrm{K}})^3}{G\Omega_K}} \approx 0.578\eta^3 M_*. \tag{3.32}$$

This mass is often adopted as the initial embryo mass in the works involving pebble accretion (e.g. Bitsch et al. 2015b). The value of m_{t} is a few times larger than $m_{\mathrm{PA,hw}}$ from Eq. (3.31) for $\mathrm{St} = 0.1$. This indicates these initial embryos can always grow by pebble accretion efficiently.

The evolution from the point of planetesimal formation to the onset of pebble accretion is missing in this approach. We also note that the characteristic mass ($0.3M_G$) of the adopted initial planetesimal mass function is about an order of magnitude less massive than $m_{\mathrm{PA,hw}}$, which is comparable to the value adopted by Coleman (2021). However, in the expression for m_G in this work as shown by Eq. (3.9), the value of the small-scale diffusion parameter δ can be an order of magnitude larger or smaller than the adopted value (Schreiber & Klahr 2018). This translates to an even larger uncertainty in the initial planetesimal mass since $m_G \propto \delta^{3/2}$, which shall greatly change the results of our model and will require further investigations.

Pebble accretion and dynamical heating

However, as noted by Ida et al. (2016), the assumption of small e in the estimation of the pebble relative velocity only holds when $e < \eta \sim 10^{-3}$. This condition breaks down quite early in the presented simulations, with a majority of the particles having e exceeding 10^{-3} by 0.75 Myr in all the presented simulations. Multiple planet formation models (e.g. Levison et al. 2015; Jang et al. 2022; Lau et al. 2022; Jiang & Ormel 2023) have shown the effect of increased pebble relative velocity due to dynamical heating on pebble accretion. Figure 3.12 also includes the general form of κ_{OL18} with $\Delta v = \max(0.76e, \eta v_K)$ (Liu & Ormel 2018) for $e = 10^{-2}$, where the curve is shifted towards higher m by more than two orders of magnitudes, i.e. a much larger m is required for efficient pebble accretion. Therefore, it is likely an important feature of a realistic model to consider the effect of pebble accretion being interrupted when the eccentricities grow, especially in the context of planet formation where massive cores and giant planets are formed among planetesimals. However, once planet migration is in effect and cores of $\sim 1 - 10M_\oplus$ are readily removed, they cannot continuously excite and eject the planetesimals. Pebble accretion in this case is not severely interrupted by dynamical heating as shown in the results (Sect. 3.3.2), so that both pebble accretion prescriptions yield more similar results at the end of the simulations when migration and removal is present.

We note that there are other works on the initial planetesimal mass function (e.g. Simon et al. 2016, 2017; Schäfer et al. 2017; Gerbig & Li 2023), and this topic remains an active field of research. Meanwhile, the outcome of the subsequent growth of the initial planetesimals is sensitive to their initial mass as well as the distribution. Also, we assume a planetesimal disc as a part of the initial conditions, but its formation is not investigated in this work, which is also an active field of research (e.g. Drążkowska et al. 2016; Carrera et al. 2017; Schoonenberg et al. 2018; Lenz et al. 2019, 2020). These parts of the model concerning the initial planetesimals require further investigations for a more robust planet formation model.

3.4.2 Planet migration

When planet migration is turned off in our model, i.e. $S_a = 0$, the results with $N_{\mathrm{ini}} = 1000$ and $\epsilon_{\mathrm{PA}} = \epsilon_{\mathrm{OL18}}$ (Sect. 3.3.1, Fig. 3.7) show one to two gas giants and one to two ice giants beyond 6 au. This is in general agreement with Levison et al. (2012) in forming the giant planets in the Solar System without forming hundreds of massive cores in the process. In their work, planet migration is not considered either.

However, once planet migration is turned on in our model, i.e. $S_a = 1$, the results (Sect. 3.3.2) show that cores of $\sim 1 - 10 M_\oplus$ rapidly migrate towards the inner part of the disc and many leave the simulation domain as a migration trap is not implemented at the inner edge of the disc. This is in agreement with previous works on planet formation that include planet migration (e.g. Cossou et al. 2014; Coleman & Nelson 2016b; Matsumura et al. 2017; Jang et al. 2022). Although the migration timescale in the high-mass regime in this work is already lengthened by setting a turbulent-α parameter $\alpha_{\rm turb}$ that is only one-tenth of the classical α parameter $\alpha_{\rm acc}$, it is still not enough to retain these massive cores at wide orbit in our model to form Solar-System-like giant planets. Further parameter search may be required to produce cold giant planets with planet migration in effect but the current results suggest that some massive cores are inevitably lost to the inner Solar System in the process as shown in other works (e.g. Bitsch et al. 2019; Matsumura et al. 2021).

Figure 3.14 shows a heat map of the migration timescale τ_a in the m–r space at $t = 0.5$ Myr in our model. There is a region of rapid migration with $\tau_a \sim 10^5$ yr for $m \sim 1 - 10 M_\oplus$ across the planetesimal disc. This is in agreement with the results that the massive cores have migrated significantly before runaway gas accretion can occur for them to enter the high-mass regime of migration where $\tau_a \sim 10^6$ yr. For the surviving cores, migration only stops as the gas surface density becomes very low that slows down migration but this also terminates gas accretion as shown in the results. Also, it seems to be a general result that multiple massive cores ($\sim 1 - 10 M_\oplus$) inevitably enter the inner Solar System with a smooth disc model where migration trap is not present except at the inner edge of the protoplanetary disc. In contrast, other works (e.g. Coleman & Nelson 2016a; Lau et al. 2022) have shown a possibility in retaining these cores at wide orbit due to the presence of a substructure in the gas disc. These findings and the recent observations of substructure in protoplanetary discs (e.g. Andrews et al. 2018; Long et al. 2018; Dullemond & Penzlin 2018; Cieza et al. 2021) suggest that a substructure in the protoplanetary disc is a promising way to interrupt rapid migration and prevent the formation of super-Earths and hot Jupiters.

3.5 Conclusions

This work attempts to form the giant planets of the Solar System in a smooth protoplanetary disc. An initial planetesimal disc is simulated with the parallelized N-body code SyMBAp with additional subroutines to include the effects of pebble accretion, gas accretion, and planet-disc interactions with the protoplanetary disc.

Our model starts from planetestesimals (each with $m \lesssim 10^{-4} M_\oplus$) instead of planetary embryos ($m \sim 10^{-2} M_\oplus$). In this work, we demonstrate the difference between the pebble accretion prescription by Ida et al. (2016) and that by Liu & Ormel (2018) and Ormel & Liu (2018). In Ida et al. (2016), the pebble-accreting body is assumed to be in a circular orbit and the pebble relative velocity, which sets the pebble encounter time, is set by the headwind in the disc. In contrast, Liu & Ormel (2018) and Ormel & Liu (2018) do not hold this assumption and consider the relative velocity due to eccentricity and inclination. In the case that the number of embryos is small and they are well above the pebble accretion onset mass both prescriptions give similar results, as noted in Matsumura et al. (2021). However, in a planetesimal disc, viscous stirring becomes important and can effectively terminate growth by pebble accretion due to the increased pebble relative velocity and shortened pebble encounter time. This can occur when the inclinations of the bodies are small, and they are still well inside the pebble disc as also noted by Lau et al. (2022). Therefore, to realistically model planet formation via pebble accretion starting from planetesimals, it is crucial to consider the reduced pebble encounter time due to dynamical heating.

When planet migration is not considered, our model can reproduce one to two gas giants and one to two ice giants beyond 6 au, which is analogous to the giant planets in the Solar System. However, we also note that the results have a dependence on the initial number of planetesimals. Further studies on the processes involved in planetesimals formation is required to construct a more realistic model.

Once planet migration is in effect, massive cores of about 10 $M_\oplus$ are readily removed as they migrate towards the inner boundary of the simulations. This shows that the formation of the giant planets in the Solar System requires an alternative and effective way to stop the migration of the first massive body formed before reaching the inner Solar System. Multiple works (e.g. Coleman & Nelson 2016a; Lau et al. 2022) have demonstrated that pressure bump in the disc can act as a migration trap while some other works (e.g. Jiang & Ormel 2023; Chrenko & Chametla 2023) do not support this scenario. Further investigations are required to characterize the disc conditions that can retain massive planetary cores and allow the formation of cold gas giants.

Acknowledgments

This work was supported in part by a postgraduate studentship (T.C.H.L.) and a seed fund for basic research (T.C.H.L and M.H.L.) at the University of Hong Kong and Hong Kong RGC grant 17306720 (T.C.H.L and M.H.L.). Parts of the computations were performed using research computing facilities offered by HKU Information Technology Services. T.C.H.L also acknowledges funding from the Deutsche Forschungsgemeinschaft (DFG, German Research Foundation) under grant 325594231. This research was supported by the Munich Institute for Astro-, Particle and BioPhysics (MIAPbP) which is funded by the Deutsche Forschungsgemeinschaft (DFG, German Research Foundation) under Germany´s Excellence Strategy – EXC-2094 – 390783311.

3.6 Appendix

3.6.1 Additional figures

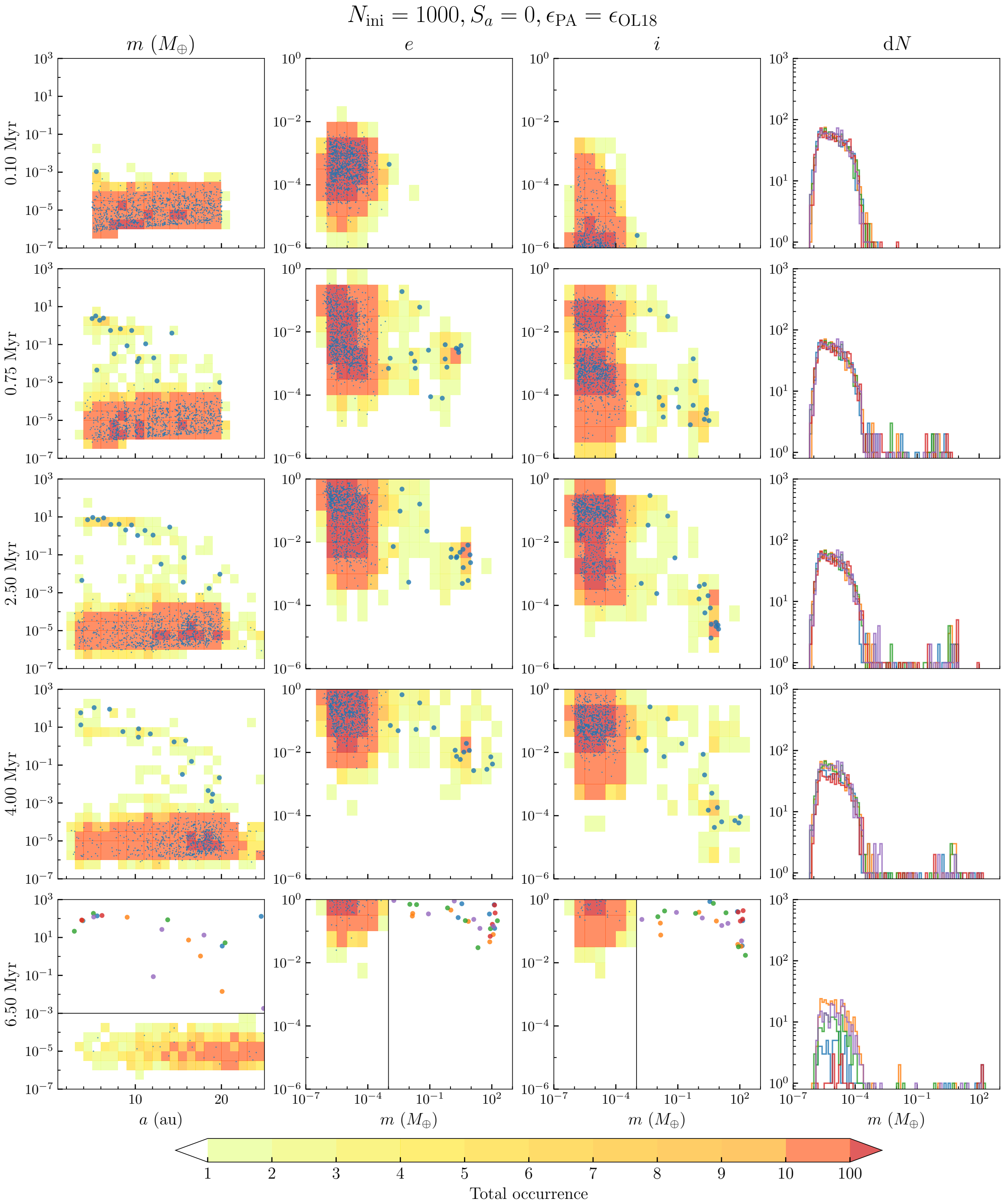

Figure 3.7: Same as Fig. 3.5 except $\epsilon_{\text{PA}} = \epsilon_{\text{OL18}}$.

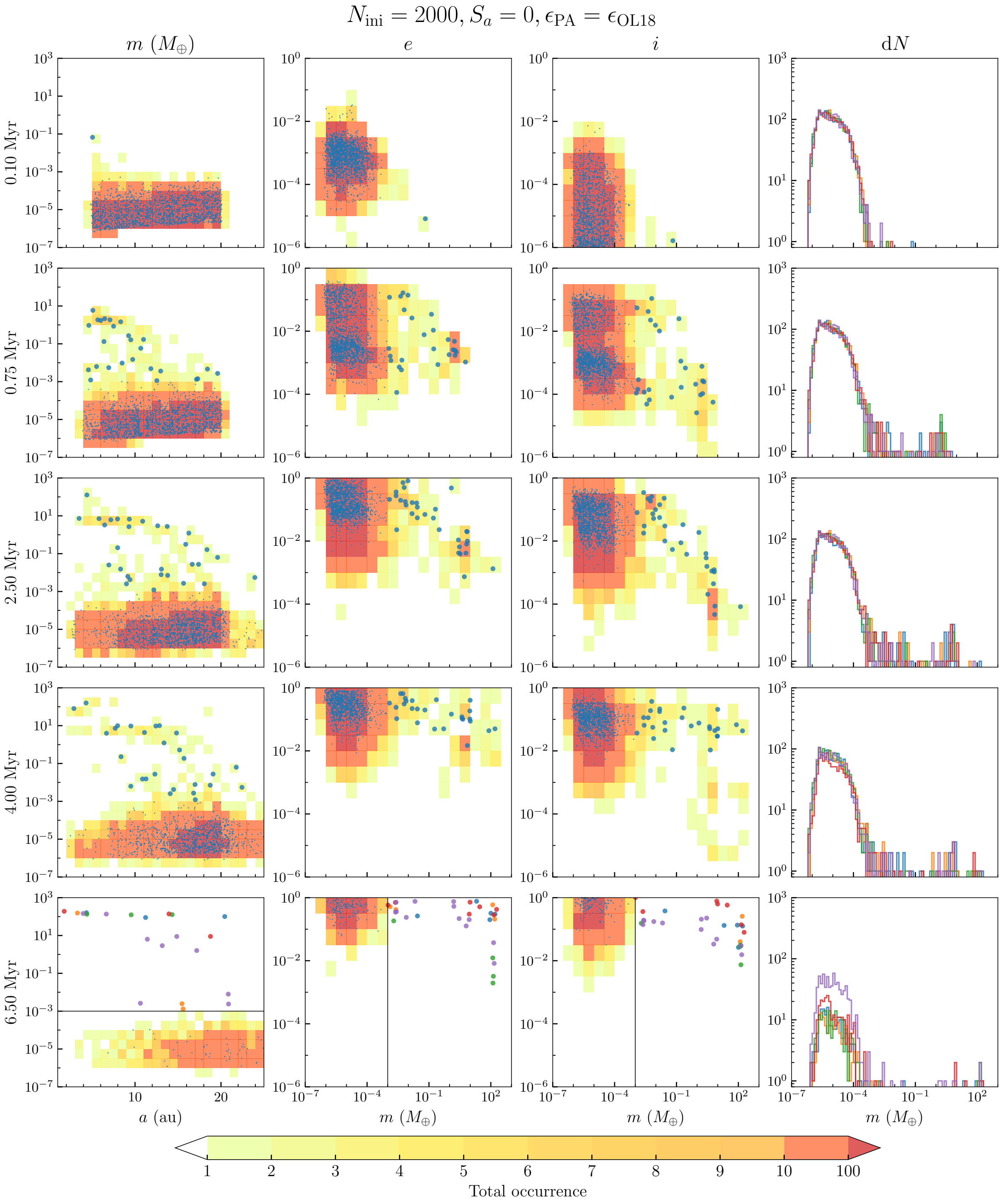

Figure 3.8: Same as Fig. 3.7 except $N_{\rm ini}$ = 2000.

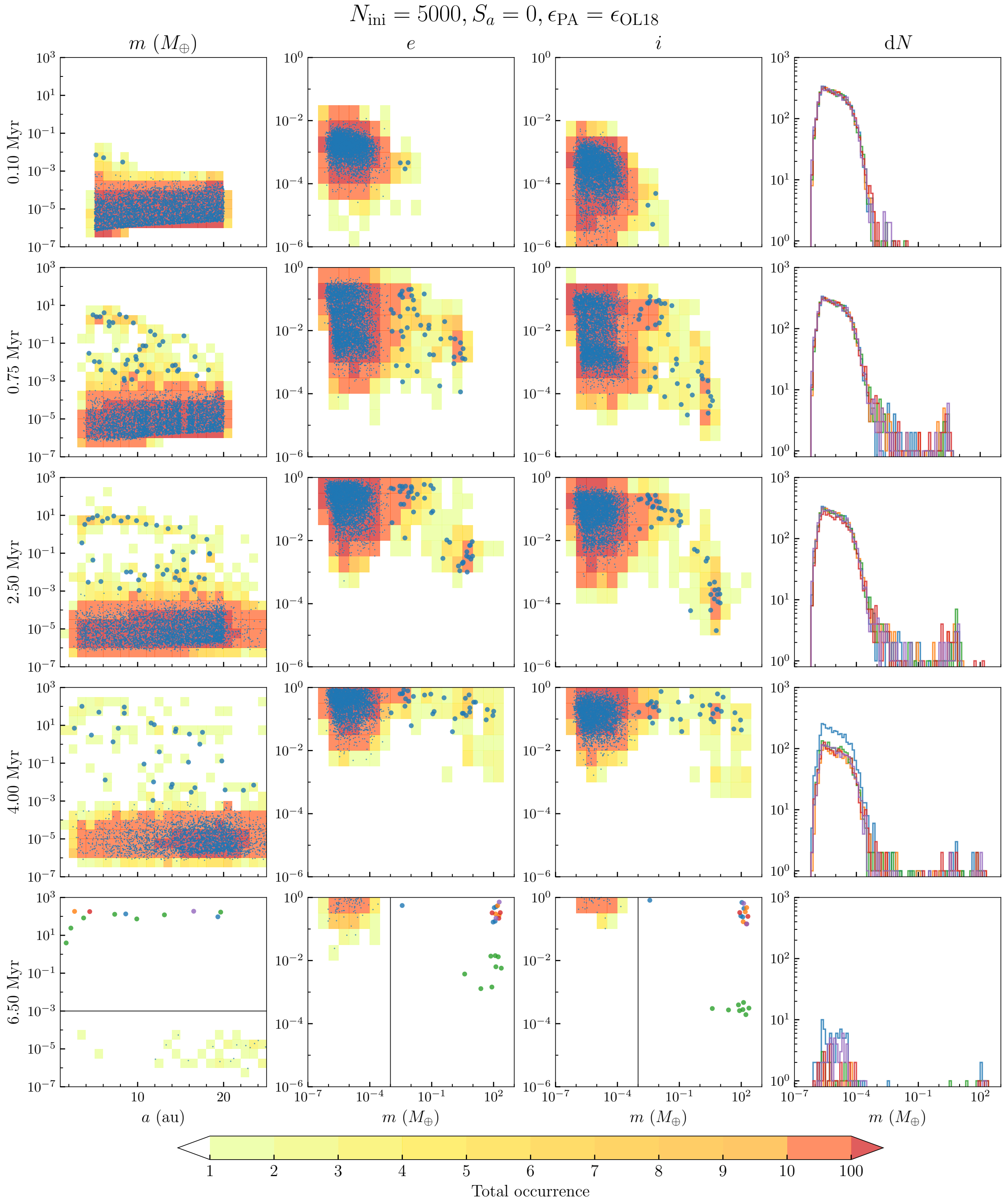

Figure 3.9: Same as Fig. 3.7 and 3.8 except $N_{\rm ini}$ = 5000.

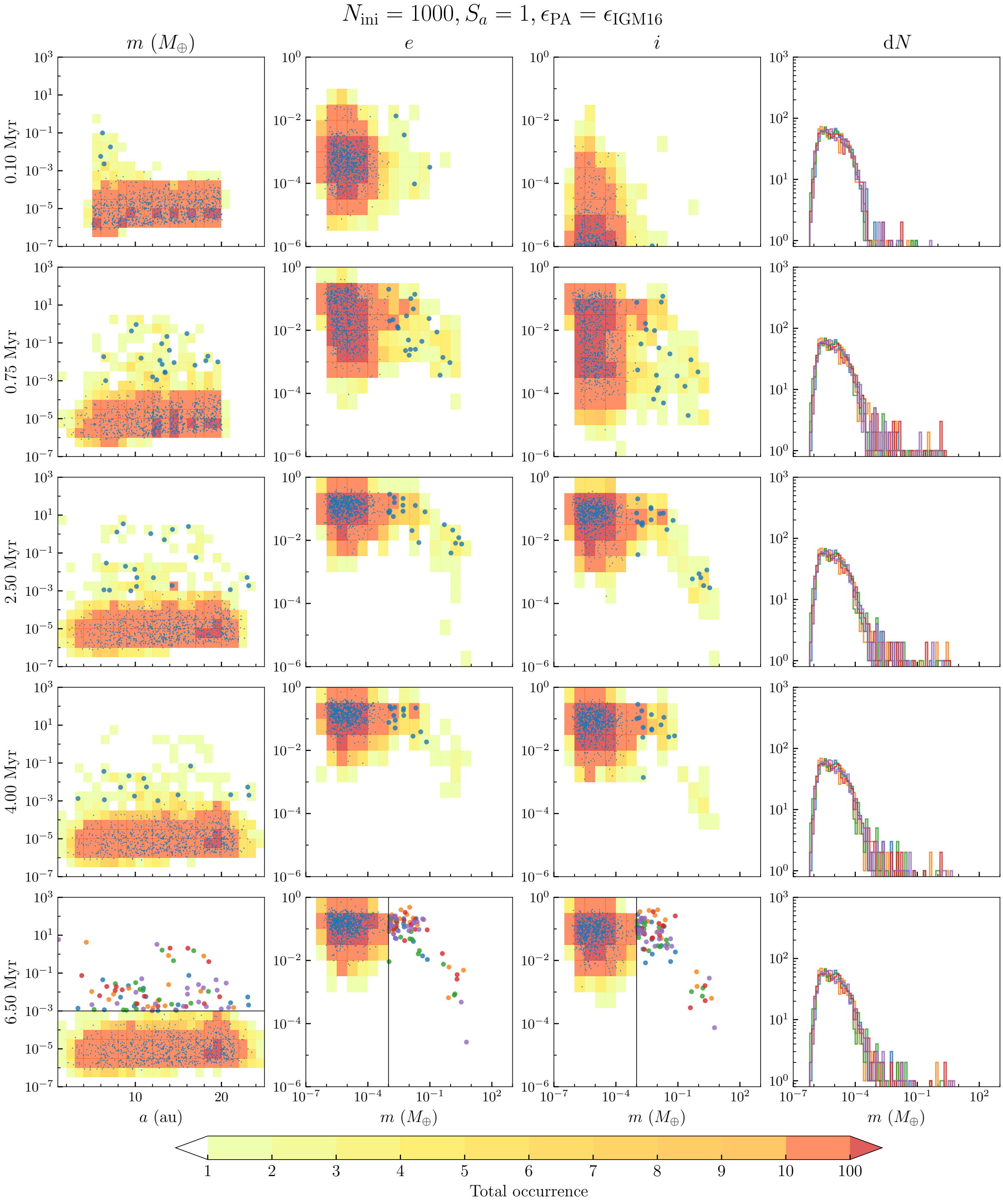

Figure 3.10: Same as Fig. 3.5 except with migration turned on ($S_a = 1$).

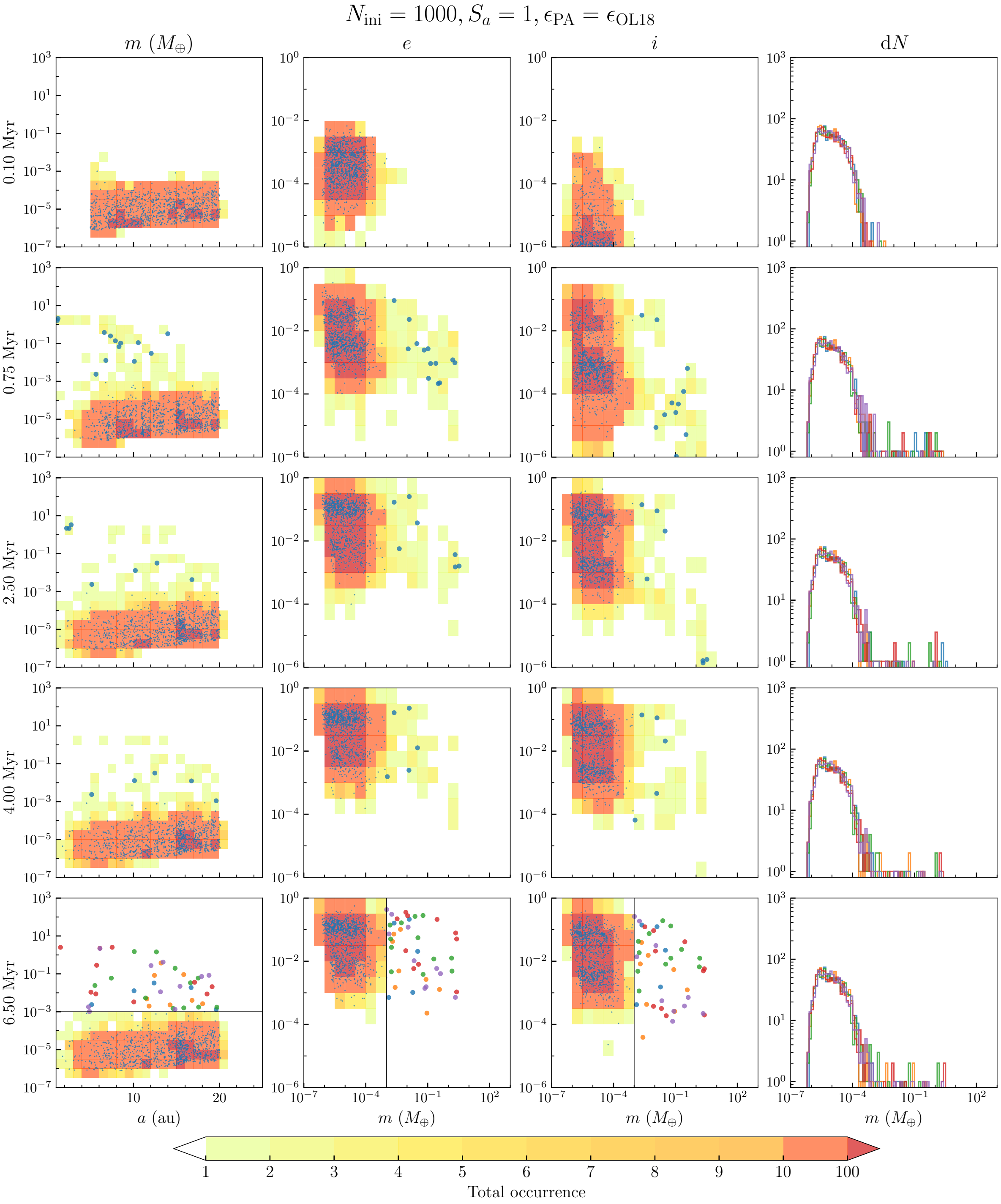

Figure 3.11: Same as Fig. 3.7 except $S_a = 1$.

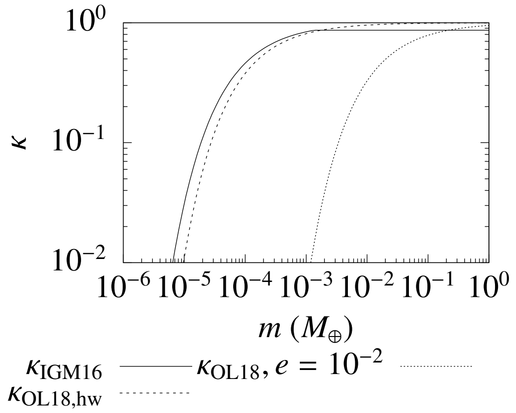

Figure 3.12: Reduction factor κ on the pebble accretion cross section in our disc model according to the prescription by Ida et al. (2016), κ_{IGM16} (solid line), a similar reduction factor by Liu & Ormel (2018) in the head wind regime with small e and i $\kappa_{\mathrm{OL18,hw}}$ (dashed line), and that with $e = 10^{-3}$ and small i $\kappa_{\mathrm{OL18}}, e = 10^{-2}$ (dotted line) as different mass m. The values of St = 0.1 and $r = 5$ au are set for this estimation.

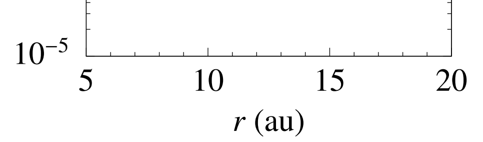

Figure 3.13: Pebble accretion onset mass $m_{\mathrm{PA,hw}}$ in the headwind regime (solid line) and the planetesimal gravitational mass m_G (dashed line) at different locations of the disc r with the corresponding value of η shown in the upper x-axis. The values of m_G are around the mass range for the steep cutoff in κ shown in Fig. 3.12.

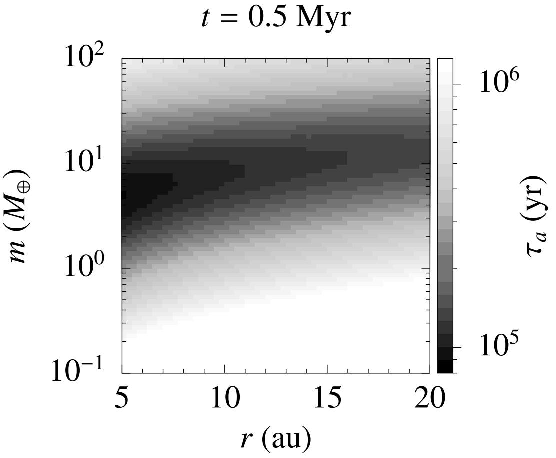

Figure 3.14: Heat map of the migration timescale τ_a in the m–r space at t = 0.5 Myr in our model. A region of rapid migration ($\tau_a \sim 10^5$ yr) is presence for $m \sim 1 - 10 M_\oplus$ across the planetesimal disc (r = 5 – 20 au).

Chapter 4

Rapid formation of massive planetary cores in a pressure bump

Tommy Chi Ho Lau, Joanna Drążkowska, Sebastian M. Stammler, Tilman Birnstiel, and Cornelis P. Dullemond

This chapter was published in Astronomy & Astrophysics, 668, A170 (2022)

Abstract: Models of planetary core growth by either planetesimal or pebble accretion are traditionally disconnected from the models of dust evolution and formation of the first gravitationally-bound planetesimals. The state-of-the-art models typically start with massive planetary cores already present. We aim to study the formation and growth of planetary cores in a pressure bump, motivated by the annular structures observed in protoplanetary disks, starting with sub-micron-sized dust grains. We connect the models of dust coagulation and drift, planetesimal formation in the streaming instability, gravitational interactions between planetesimals, pebble accretion, and planet migration, into one uniform framework. We find that planetesimals forming early at the massive end of the size distribution grow quickly dominantly by pebble accretion. These few massive bodies grow on the timescales of ~100 000 years and stir the planetesimals formed later preventing the emergence of further planetary cores. Additionally, a migration trap occurs allowing for retention of the growing cores. Pressure bumps are favourable locations for the emergence and rapid growth of planetary cores by pebble accretion as the dust density and grain size are increased and the pebble accretion onset mass is reduced compared to a smooth-disk model.

4.1 Introduction

Recent high-resolution interferometry observations by the Atacama Large Millimeter/submillimeter Array (ALMA) revealed that substructure may be common in protoplanetary disks, although we are still limited to the largest and thus brightest ones. Nevertheless, there is increasing evidence that disk substructures must be common even in unresolved disks coming from comparison of the observational data of disks population and theoretical models (Toci et al. 2021; Zormpas et al. 2022). Multiple surveys, e.g. Andrews et al. (2018), Long et al. (2018) and Cieza et al. (2021), have shown that most of the substructures are presented in the form of axisymmetric rings. Through detailed analysis, Dullemond & Penzlin (2018) found that dust trapping in a pressure bump is consistent with the rings sampled from the DSHARP survey. Kinematic studies with ALMA by Teague et al. (2018a,b) further showed that the dust rings coincide with the local pressure maxima in the analyzed disks. However, the origin of such pressure bumps remains uncertain, where the possible causes include disk-planet interaction due to an existing massive planet (Rice et al. 2006; Pinilla et al. 2012; Dipierro et al. 2015; Dong et al. 2017), sublimation (Saito & Sirono 2011) and instabilities (Takahashi & Inutsuka 2014; Flock et al. 2015; Lorén-Aguilar & Bate 2015; Pinilla et al. 2016; Dullemond et al. 2018).

Despite the uncertainties of the cause, the dust-trapping pressure bump is likely a favourable environment for the formation and growth of planetesimals towards massive planetary cores (Morbidelli 2020; Guilera et al. 2020; Chambers 2021; Andama et al. 2022). The locally enriched dust-to-gas ratio could trigger streaming instability (Youdin & Lithwick 2007; Johansen et al. 2007, 2009; Bai & Stone 2010), which is the prevailing pathway to overcome the 'metre-size barrier' of dust growth (Weidenschilling 1977; Güttler et al. 2010; Zsom et al. 2010) to form planetesimals in the order of 100 km (Johansen et al. 2012, 2015; Simon et al. 2016, 2017). More recently, Stammler et al. (2019) suggested that planetesimal formation by streaming instability, where the midplane dust-to-gas ratio is regulated, can explain the similarity in the optical depths of the DSHARP rings studied by Dullemond & Penzlin (2018). And, in the hydrodynamical simulations with self-gravity by Carrera et al. (2021), a small pressure bump can already trigger planetesimal formation by streaming instability with cm-sized grains, although this may not be applicable to the case with mm-sized dust (Carrera & Simon 2022).

In the classical model, planetesimal accretion has been shown to quickly enter a stage of oligarchic growth with direct-N body simulations (Kokubo & Ida 2000). A massive planetary core is unlikely to form and accrete gas within the typical lifetime of protoplanetary disks particularly at wide orbits to form cold Jupiter with the minimum mass solar nebula, while multiple works (e.g. Fortier et al. 2007, 2009; Guilera et al. 2010) have shown planetesimal accretion can be efficient in a significantly more massive disk. However, planetesimals that are large enough to gravitationally deflect dust from the gas streamline and have long enough encounter time can accrete a significant fraction of the drifting dust or 'pebbles'. This emerged as a mechanism for efficient planetesimal growth often named 'pebble accretion' (Ormel & Klahr 2010; Lambrechts & Johansen 2012; Guillot et al. 2014; see Johansen & Lambrechts 2017; Ormel 2017, for review). In a pressure bump, pebbles are trapped and the locally enhanced dust surface density also provides an elevated level of pebble flux compared to that in a smooth disk. The impeded drifting speed of the pebbles also lengthens the encounter time with the planetesimal particularly in the outer disk, where the pebble-carrying headwind is faster. Both of these factors increase the rate of planetesimal growth by pebble accretion inside a pressure bump.

As planetesimals grow into more massive embryos, the gravitational torque exerted by the disk becomes important. For low-mass planets that induce small perturbations in the disk, the disk-planet interaction lies in the type-I (or low-mass) regime (Goldreich & Tremaine 1979; Artymowicz 1993; Tanaka et al. 2002; Tanaka & Ward 2004; see Kley & Nelson 2012, for review). As shown in the recent N-body planet formation models, e.g. Matsumura et al. (2017); Bitsch et al. (2019); Liu et al. (2019), this poses a challenge: embryos formed in the outer Solar System should be stopped from entering the terrestrial planet region as they are needed in the outer Solar system to form cold giant planets. However, Coleman & Nelson (2016a) showed that radial substructures in the disk can trap embryos at the outer edges and allow the formation of cold Jupiters. This suggests pressure bumps are not only favourable to the growth of planetesimals, but also capable of retaining the massive planetary cores produced.

In this work, we model the formation and evolution of planetesimals in an axisymmetric pressure bump of a protoplanetary disk numerically. We coupled the dust and gas evolution code `DustPy` (Stammler & Birnstiel 2022) with the parallelized symplectic N-body integrator `SyMBAp` (Lau & Lee in prep.) with modifications to include gas drag, type-I damping and migration, and pebble accretion according to the disk model. As the disk evolves and accumulates dust at the pressure bump, a fraction of the dust is converted into planetesimals according to the condition for streaming instability. These planetesimals are then realized as N-body particles and evolve through gravitational interactions as well as the additional processes mentioned. The details of our models and initial conditions are presented in Section 4.2. The results of this work is presented in Section 4.3, which are followed by the discussions in Section 4.4. The findings of our work is summarized in Section 4.5.

4.2 Method

`DustPy` (Stammler & Birnstiel 2022), based on the model by Birnstiel et al. (2010), is employed to simulate a protoplanetary disk, which includes viscous evolution of the gas, coagulation, fragmentation, advection and diffusion of the dust. It is coupled to `SyMBAp` (Lau & Lee in prep.), which is a parallelized version of the symplectic direct N-body algorithm `SyMBA` (Duncan et al. 1998).

4.2.1 Disk model

Gas component

We considered a protoplanetary disk around a Solar-type star. The disk is assumed to be axisymmetric and in vertical hydrostatic equilibrium. The initial gas surface density $\Sigma_{\mathrm{g,init}}$ is set according to the self-similar solution of a viscous disk by Lynden-Bell & Pringle (1974) such that

$$\Sigma_{\mathrm{g,init}} = \frac{M_{\mathrm{disk}}}{2\pi r_{\mathrm{c}}^2}\left(\frac{r}{r_{\mathrm{c}}}\right)^{-1}\exp\left(-\frac{r}{r_{\mathrm{c}}}\right) \tag{4.1}$$

with the distance from the star r, the initial mass of the disk M_{disk} and the characteristic radius r_{c}. We have set $M_{\mathrm{disk}} = 0.1 M_{\odot}$ and $r_{\mathrm{c}} = 100$ au, which imply $\Sigma_{\mathrm{g,init}} \approx 1400\ \mathrm{g\ cm^{-2}}$ at $r = 1$ au. The gas disk is viscously evolved in time t according to the advection-diffusion equation

$$\frac{\partial \Sigma_{\mathrm{g}}}{\partial t} = \frac{3}{r}\frac{\partial}{\partial r}\left[r^{1/2}\frac{\partial}{\partial r}(\nu \Sigma_{\mathrm{g}} r^{1/2})\right], \tag{4.2}$$

where the back reaction from the dust is neglected. The Shakura & Sunyaev (1973) α-parametrization is adopted for the kinematic viscosity ν such that

$$\nu = \alpha c_\mathrm{s} H_\mathrm{g} \tag{4.3}$$

with the speed of sound c_s and the disk scale height H_g. The viscosity parameter $\alpha = 10^{-3}$ is set in this work. The disk scale height is defined by $H_\mathrm{g} \equiv c_\mathrm{s}/\Omega_\mathrm{K}$, where the local Keplerian orbital frequency $\Omega_\mathrm{K} = \sqrt{GM_*/r^3}$ with the gravitational constant G and the mass of the central star M_*. The isothermal sound speed is used and given by $c_\mathrm{s} = \sqrt{k_\mathrm{B}T/\mu}$ with the Boltzmann constant k_B, the midplane temperature T and the mean molecular weight of the gas $\mu = 2.3m_\mathrm{p}$. The disk is assumed to be passively irradiated by the Solar luminosity, which gives a midplane temperature profile

$$T \approx 263.2 \left(\frac{r}{\mathrm{au}}\right)^{-1/2} \mathrm{K}. \tag{4.4}$$

This setup yields the dimensionless gas disk scale height

$$\hat{h}_\mathrm{g} \equiv \frac{H_\mathrm{g}}{r} \approx 0.0326 \left(\frac{r}{\mathrm{au}}\right)^{1/4}. \tag{4.5}$$

The midplane pressure gradient parameter η is then given by

$$\eta = -\frac{\hat{h}_\mathrm{g}^2}{2} \frac{\partial \ln P}{\partial \ln r} \tag{4.6}$$

with the midplane gas pressure P, which describes the degree of 'sub-Keplerity' of the gas. A logarithmic radial grid is adopted that spans, for a disk gap at 10 au, from 1 to 100 au with 99 cells, and, for a disk gap at 75 au, from 10 to 100 au with 66 cells. Additional grid refinement is imposed around the exterior pressure bump of the gap (see Section 4.2.2).

Dust component

The initial dust surface density $\Sigma_\mathrm{d,init}$ is given by

$$\Sigma_\mathrm{d,init} = Z\, \Sigma_\mathrm{g,init} \tag{4.7}$$

with the global dust-to-gas ratio Z set at the Solar metallicity of 0.01. We follow the size distribution of the interstellar medium (Mathis et al. 1977) for the initial dust grain sizes. The maximum initial size is set at 1μm and the internal density of 1.67 g cm^{-3} is assumed. A total of 141 dust mass bins logarithmically spaced from 10^{-12} to 10^{8} g are used. Each mass species is evolved in time through transport with the advection-diffusion equation (Clarke & Pringle 1988) coupled to growth and fragmentation with the Smoluchowski equation. The fragmentation velocity is assumed to be 10 m s^{-1}. At collision velocities above which, the dust aggregates are assumed to fragment. The Stokes number St_i of each mass bin i is then calculated by considering the Epstein and the Stokes I regimes. The dust scale height of each mass species $H_{\mathrm{d},i}$ is calculated according to Dubrulle et al. (1995)

$$H_{\mathrm{d},i} = H_\mathrm{g} \sqrt{\frac{\alpha}{\alpha + \mathrm{St}_i}}. \tag{4.8}$$

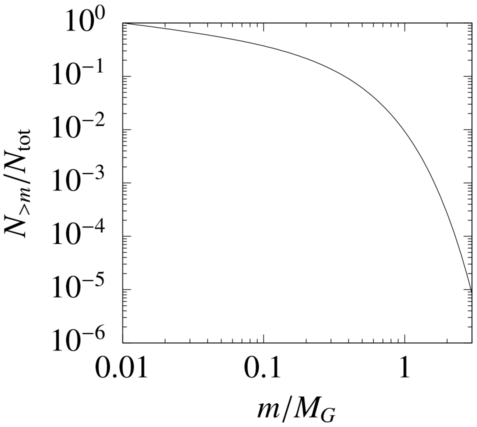

Figure 4.1: The truncated power law cumulative mass distribution adopted following Abod et al. (2019).

Further details of the gas and dust evolution algorithm are described in Stammler & Birnstiel (2022).

4.2.2 Disk Gap

A stationary Gaussian gap is created in the disk following the model in Dullemond & Penzlin (2018). A pre-existing planet in the gap is not considered in this work. Since $\alpha\Sigma_{\mathrm{g}}$ is a constant in our disk model at a steady state, the disk gap can be created from a smooth disk by adopting a modified α-parameter with radial dependence $\alpha'(r)$ given by

$$\alpha'(r) = \alpha/F(r), \tag{4.9}$$

where the function

$$F(r) = \exp\left[-A\exp\left(-\frac{(r-r_0)^2}{2w^2}\right)\right] \tag{4.10}$$

with the gap amplitude A, the location r_0 and the gap width w. We fixed $A = 2$ and tested two gap locations $r_0 = \{10, 75\}$ au. At $r_0 = 10$ au, w is set to 2 au. At $r_0 = 75$ au, w is scaled by $r^{13/16}$ yielding $w \approx 10.3$ au. This is motivated by the radial scaling of the gap width given by the empirical formula for the structure of a planet-induced gap in Kanagawa et al. (2017). Combined with the disk model, the prescribed disk gap also results in a local maximum of gas surface density at the outer edge, which is also a local maximum of pressure. We note that the sign of η in Eq. 4.6 changes across the pressure maximum, where $\eta > 0$ implies sub-Keplerian gas and $\eta < 0$ implies super-Keplerian gas.

4.2.3 Planetesimal formation

As dust accumulates at the exterior pressure bump of the disk gap, the dust is converted into planetesimals based on the prescriptions in Drążkowska et al. (2016) and Schoonenberg et al. (2018) with the adoption of the smooth planetesimal formation activation function $\mathcal{P}_{\mathrm{pf}}$ in Miller

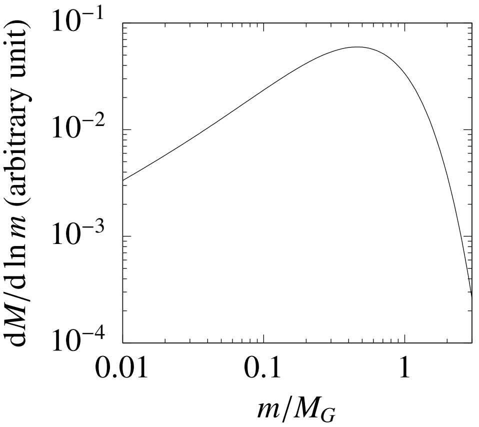

Figure 4.2: The total mass in each logarithmic mass bin in the adopted planetesimal mass distribution. The mass in the most massive bin is about 17.9 times more massive than the bin at $10^{-2}M_G$.

et al. (2021). A smooth activation function that centres around a midplane dust-to-gas ratio $\rho_\mathrm{d}/\rho_\mathrm{g}$ of unity is expected to be more probable than a sharp activation of the streaming instability, because the latter causes planetesimals to form in discrete pulses with sharp temporal fluctuations in our tests. The smooth activation function is given by

$$\mathcal{P}_\mathrm{pf} = \frac{1}{2}\left[1 + \tanh\left(\frac{\log(\rho_\mathrm{d}/\rho_\mathrm{g})}{n}\right)\right] \tag{4.11}$$

with the smoothness parameter n set to 0.03 in this work. $\mathcal{P}_\mathrm{pf}$ is evaluated at each radial cell and the local dust surface density in each mass bin i is removed by

$$\frac{\partial \Sigma_{\mathrm{d},i}}{\partial t} = -\mathcal{P}_\mathrm{pf}\Sigma_{\mathrm{d},i}\frac{\zeta}{t_{\mathrm{set},i}} = -\mathcal{P}_\mathrm{pf}\zeta\Sigma_{\mathrm{d},i}\mathrm{St}_i\Omega_\mathrm{K} \tag{4.12}$$

with ζ the planetesimal formation efficiency per settling time, which we set to 0.05 corresponding to a planetesimal conversion time of 40 settling times when the dust-to-gas ratio is unity. The settling time $t_{\mathrm{set},i}$ of mass bin i is given by

$$t_{\mathrm{set},i} = \frac{1}{\mathrm{St}_i\Omega_\mathrm{K}}. \tag{4.13}$$

We note that ζ is not well-constrained while the effect of using a different value is not studied in this work. Then, the local dust surface density loss is summed over all mass bins and added to the local planetesimal surface density Σ_plts, i.e.,

$$\frac{\partial \Sigma_\mathrm{plts}}{\partial t} = -\sum_i \frac{\partial \Sigma_{\mathrm{d},i}}{\partial t}. \tag{4.14}$$

Planetesimals are then realized from the radial profile of $\Sigma_\mathrm{plts}(r)$. We adopted the cumulative mass distribution resulting from the fitting to the streaming instability simulations by Abod et al.

(2019). This has the form of an exponentially truncated power law such that the number fraction of planetesimals above mass m is given by

$$\frac{N_{>m}}{N_{\rm tot}} = \left(\frac{m}{m_{\rm min}}\right)^{-0.3} \exp\left(\frac{m_{\rm min} - m}{0.3M_G}\right), \tag{4.15}$$

for $m \geq m_{\rm min}$ with the minimum planetesimal mass $m_{\rm min}$ and the characteristic planetesimal mass M_G. The form of Eq. (4.15) is shown in Fig. 4.1. Schäfer et al. (2017) noted that $m_{\rm min}$ is sensitive to the spacial resolution of streaming instability simulation. Nonetheless, the total mass in each mass bin in logarithmic scale can be estimated by

$$\mathrm{d}M \propto -\frac{\mathrm{d}N_{>m}}{\mathrm{d}m} m^2 \mathrm{d}\ln m. \tag{4.16}$$

We have set $m_{\rm min} = 10^{-2}M_G$ in this work, where the peak of dM is about 17.9 times of that at $m_{\rm min}$ as shown in Fig. 4.2. Since Eq. (4.15) $\to 0$ only when $m \to \infty$, we artificially set the upper limit of m at $3M_G$ in the algorithm of realization, which implies that a small number fraction of planetesimals of about 8.48×10^{-6} is lost. Klahr & Schreiber (2020) considered the critical mass for gravitational collapse of a dust clump in the presence of turbulent diffusion. We have adopted this mass as M_G, which is given by

$$\begin{aligned} M_G &= \frac{1}{9}\left(\frac{\delta}{\mathrm{St}}\right)^{3/2} \hat{h}_{\rm g}^3 M_\odot \\ &\approx 7.22 \times 10^{-3} \left(\frac{\delta/\mathrm{St}}{10^{-4}/10^{-2}}\right)^{3/2} \left(\frac{\hat{h}_{\rm g}}{0.058}\right)^3 M_\oplus \end{aligned} \tag{4.17}$$

with the small-scale diffusion parameter δ which is independent of α in our model. As noted by Johansen et al. (2006), there exists discrepancy on the measurement of the relative strength of turbulent viscosity and turbulent diffusion in the literature, which remains an active research topic (e.g. Schreiber & Klahr 2018). We tested two values of $\delta = \{10^{-4}, 10^{-5}\}$. This is motivated by the measurements in streaming instability simulations by Schreiber & Klahr (2018). Depending on the box sizes, the values of the measured small-scale diffusion parameter in the radial direction range from $10^{-6} - 10^{-4}$ for the midplane dust-to-gas ratio of 1. Since $M_G \propto \delta^{3/2}$, a huge number of planetesimals are produced for the case with $\delta = 10^{-6}$ in our preliminary runs, which is computationally unaffordable. Therefore, this value of δ is not tested in this work. The potential effect is discussed in Section 4.4.3. And, St is evaluated by taking the density-averaged value across all mass bins in the local radial cell. We note that Abod et al. (2019) also provided a characteristic mass based on the balance between the tidal force and self-gravity, which has a dependence of $\Sigma_{\rm g}\Omega_{\rm K}^{-4}$ and is independent of the local diffusivity. This would result in a characteristic mass of $\sim 10M_\oplus$ at 80 au in our disk model, which is unlikely to be physically probable.

In each simulation, the semimajor axis a of a planetesimal is first randomly drawn using $\Sigma_{\rm plts}(r)$ as a radial distribution function and M_G is evaluated at the local radial cell. Then, the planetesimal mass m is drawn from Eq. (4.15). At each communication between `DustPy` and

`SyMBAp`, if the total planetesimal mass accumulated in terms of surface density exceeds this value, a planetesimal is then realized and subtracted from the accumulated mass. The eccentricity e is randomly drawn from a Rayleigh distribution with the scale parameter 10^{-6}. The inclination i in radian is also drawn from a Rayleigh distribution but with the scale parameter 5×10^{-7}. Other angles of the orbital elements are drawn randomly from 0 to 2π. The physical radius R_p is calculated by assuming an internal density ρ_s of 1.5 g cm^{-3}. Then, the planetesimal surface density is subtracted according to the m and a of the realized planetesimal. If the total planetesimal mass in the local cell is not enough, the planetesimal mass from the neighbouring cells is used for the subtraction as well. Afterwards, another value of m is drawn immediately and a planetesimal with mass m is realized until the remaining accumulated planetesimal mass is less than m. The last drawn value of m is retained for the next communication step such that the realization is not biased towards lower mass. Since this process does not guarantee that all mass in Σ_plts can be realized, the residual is accumulated for the next communication step. Further details on the communication step are in Section 4.2.5.

4.2.4 Planetesimal evolution

The realized planetesimals, and a Solar-mass central star, are then evolved by `SyMBAp` with full gravitational interactions as well as additional subroutines to include gas drag, type-I damping and migration, and pebble accretion. If two bodies collide, they are assumed to merge completely. Hence, collisions are perfectly inelastic in this work. At each communication step, other than the newly formed planetesimals in terms of surface density, the radial profiles of the gas component and the dust component are passed to `SyMBAp`. The gas component includes

- the gas surface density Σ_g;
- the midplane temperature T;
- the gas disk scale height H_g;
- the midplane gas density ρ_g, and;
- the midplane pressure gradient parameter η,

and the dust component, for each mass bin i, includes

- the Stokes number St_i;
- the dust disk scale height $H_{\mathrm{d},i}$, and;
- the dust surface density $\Sigma_{\mathrm{d},i}$.

The mass of the accreted pebbles is also passed to `DustPy` and subtracted from the dust surface density as further discussed in Section 4.2.4. As the planetesimals gradually gain mass, they are referred to as embryos, protoplanets or planetary cores in this work. Generally, planetesimal refers to a body that has not gained mass significantly while embryo refers to a body that has grown by more than an order of magnitude. Protoplanet refers to a massive dominating body in the context of viscous stirring among a crowd of planetesimals while planetary core refers to a body which is massive enough and has the potential to accrete gas and form a giant planet. Nonetheless, these bodies are not strictly distinctive and have no fundamental difference in the simulations. They are all treated as fully interacting particles.

Gas drag and type-I torques

Planetesimals and planets experience the combined effect of the aerodynamic gas drag and the type-I torques due to the planet-disk interaction in this work. Generally in typical disk environment at 10 au, gas drag ($\propto m^{-1/3}$) is more dominant for small bodies while the type-I torques ($\propto m$) gradually overtake for $m \gtrsim 10^{-5} M_\oplus$. Since gas accretion and feedback are not considered, the transition to the high-mass regime (type-II) is not included.

We adopted the aerodynamic gas drag by Adachi et al. (1976) that

$$\boldsymbol{a}_{\rm drag} = -\left(\frac{3C_{\rm D}\rho}{8R_{\rm p}\rho_{\rm s}}\right) v_{\rm rel}\boldsymbol{v}_{\rm rel}, \tag{4.18}$$

with the drag coefficient $C_{\rm D}$ and, the relative velocity between the planetesimal and the gas $\boldsymbol{v}_{\rm rel}$. The gas flow is assumed to be laminar and cylindrical, where the magnitude is given by $v_{\rm K}(1-|\eta|)$ with the local Keplerian velocity $v_{\rm K}$. Since the planetesimals in this work are well larger than km in size, the large Reynolds number case is generally applicable for $C_{\rm D}$, which we set the value to be 0.5 (Whipple 1972). The gas density ρ at the planetesimal's position z above the midplane is given by $\rho = \rho_{\rm g}\exp(-0.5z^2/H_{\rm g}^2)$.

For type-I damping and migration, we adopted the prescription based on dynamical friction by Ida et al. (2020). The timescales for the isothermal case and finite i, while $i < \hat{h}_{\rm g}$, (Appendix D of Ida et al. (2020)) are implemented. The evolution timescales of semimajor axis, eccentricity and inclination are defined respectively by

$$\tau_a \equiv -\frac{a}{{\rm d}a/{\rm d}t}, \tau_e \equiv -\frac{e}{{\rm d}e/{\rm d}t}, \tau_i \equiv -\frac{i}{{\rm d}i/{\rm d}t}. \tag{4.19}$$

These timescales are given by, with $\hat{e} \equiv e/\hat{h}_{\rm g}$ and $\hat{i} \equiv i/\hat{h}_{\rm g}$,

$$\tau_a = \frac{t_{\rm wav}}{C_{\rm T}\hat{h}_{\rm g}^2}\left[1 + \frac{C_{\rm T}}{C_{\rm M}}\sqrt{\hat{e}^2 + \hat{i}^2}\right], \tag{4.20}$$

$$\tau_e = 1.282 t_{\rm wav}\left[1 + \frac{(\hat{e}^2 + \hat{i}^2)^{3/2}}{15}\right], \tag{4.21}$$

$$\tau_i = 1.805 t_{\rm wav}\left[1 + \frac{(\hat{e}^2 + \hat{i}^2)^{3/2}}{21.5}\right]. \tag{4.22}$$

The characteristic time $t_{\rm wav}$ (Tanaka et al. 2002) is given by

$$t_{\rm wav} = \left(\frac{M_*}{m}\right)\left(\frac{M_*}{\Sigma_{\rm g} r^2}\right)\left(\frac{\hat{h}_{\rm g}^4}{\Omega_{\rm K}}\right), \tag{4.23}$$

where Σ_g and $\hat{h}_\mathrm{g}$ are retrieved from the local radial cell of the disk model. Due to frequent close encounters in the planetesimal belt, the semimajor axes may briefly depart greatly from the instantaneous locations resulting in an unphysical t_wav, which is then evaluated at the instantaneous r of the embryo instead of its semimajor axis, in contrast to the statement in Ida et al. (2020). The coefficients C_M and C_T are given by

$$C_\mathrm{M} = 6(2p_\Sigma - q_T + 2), \tag{4.24}$$

$$C_\mathrm{T} = 0.73 + 1.08p_\Sigma + 0.87q_T, \tag{4.25}$$

with $p_\Sigma \equiv -\mathrm{d}\ln\Sigma_\mathrm{g}/\mathrm{d}\ln r$ and $q_T \equiv -\mathrm{d}\ln T/\mathrm{d}\ln r$, which are evaluated with the local radial cell as well as the immediate neighbouring ones. The three timescales are then applied to the equation of motion

$$\boldsymbol{a} = -\frac{v_\mathrm{K}}{2\tau_a}\boldsymbol{e}_\theta - \frac{v_r}{\tau_e}\boldsymbol{e}_r - \frac{v_\theta - v_\mathrm{K}}{\tau_e}\boldsymbol{e}_\theta - \frac{v_z}{\tau_i}\boldsymbol{e}_z \tag{4.26}$$

in the cylindrical coordinates (r, θ, z) that the velocity of the embryo $\boldsymbol{v} = (v_r, v_\theta, v_z)$. And, v_K is evaluated at the instantaneous r of the embryo. Ida et al. (2020) noted that local uniformity on the scale of H_g is assumed in the derivations. This condition is satisfied for the disk gap implemented in this work, as described in Section 4.2.2, where the half-width is wider than the local H_g at both locations of 10 and 75 au.

Pebble accretion

The planetesimals are formed in a dust-enhanced location, where significant growth by pebble accretion is expected. We have adopted the pebble accretion efficiency ϵ_PA by Liu & Ormel (2018) and Ormel & Liu (2018), which is defined as the mass fraction of the pebble flux accreted by the planetesimal or planet. This prescription includes both the ballistic regime and the settling regime of pebble accretion and, considers the local disk conditions and the orbit of the pebble-accreting embryo. In particular, the e and i of the embryo are taken into account when evaluating the relative velocity with respect to the pebble, which is critical in a planetesimal belt as viscous stirring is significant. Since a substructured disk is considered in this work, the 'pebble formation front' model by Lambrechts & Johansen (2014) cannot be applied as explicitly noted by the authors, where a finite and positive η is assumed.

We note that η changes sign across the pressure bump and requires careful treatment. For the relative velocity between the pebble and an embryo in circular orbit, the direction of the Hill shear also changes sign for super-Keplerian pebbles drifting outwards from the inner orbits. Therefore, the existing expression combining the headwind- and shear-dominated regimes is still valid (Eq. (10) in Liu & Ormel (2018)) and the absolute value of η should be used in this case. Since the radial profile of η is given in a radial grid from `DustPy`, to capture the narrow region where η can be very close to zero, the value of η is interpolated at the radial position of each embryo before the absolute value is taken.

Following Drążkowska et al. (2021), the pebble accretion rate is calculated by summing the respective rates for each mass bin i at the local radial cell, which is given by multiplying the corresponding $\epsilon_{\mathrm{PA},i}$ to the pebble flux $\dot{M}_{\mathrm{peb}} = 2\pi r v_{\mathrm{drift},i}\Sigma_{\mathrm{d},i}$. The pebble drift velocity $v_{\mathrm{drift},i}$ of mass bin i is given by (Weidenschilling 1977)

$$v_{\mathrm{drift},i} = 2\mathrm{St}_i|\eta|r\Omega_{\mathrm{K}}. \tag{4.27}$$

The accretion rate can be summarized as

$$\dot{m} = \sum_i \epsilon_{\mathrm{PA},i} 2\pi r v_{\mathrm{drift},i}\Sigma_{\mathrm{d},i} \tag{4.28}$$

$$= \sum_i \epsilon_{\mathrm{PA},i} 4\pi r^2 \mathrm{St}_i|\eta|\Omega_{\mathrm{K}}\Sigma_{\mathrm{d},i}. \tag{4.29}$$

Since η is expected to cross zero in our disk model, we note that this means $v_{\mathrm{drift}} = 0$ when $\eta = 0$ with Eq. (4.27) and ϵ_{PA} is undefined. In our implementation, this would give $\dot{m} = 0$ as the supply of pebbles by headwind is halted. The mass of the accreted pebbles of each mass bin in the respective radial cell is then subtracted from the dust component of the disk in the next immediate communication step. Nonetheless, the contribution from the turbulence of the gas and the diffusion of the dust on v_{drift} are neglected that only the pebbles supplied by the headwind is considered, i.e., a more conservative pebble accretion rate is adopted. The possible implications are further discussed in Section 4.4.1.

Since this work neglects the gas feedback from the embryos onto the disk, the simulation is stopped once any particle reaches 1/10 of the local pebble isolation mass m_{iso}, which is given by (Lambrechts et al. 2014)

$$m_{\mathrm{iso}} = 20\left(\frac{\hat{h}_{\mathrm{g}}}{0.05}\right)^3 M_{\oplus}. \tag{4.30}$$

Nonetheless, (Sándor & Regály 2021) reported that the pebble isolation mass may be about 2 – 3 times larger at a pressure bump while the results presented in Bitsch et al. (2018) do not support this conclusion.

4.2.5 Numerical set-up

The timestep in `DustPy` Δt_{disk} is variable and determined by the rate of change of the gas and dust surface densities while `SyMBAp` requires a fixed timestep Δt_{nbod} for the symplecticity. For all the simulations in this work, $\Delta t_{\mathrm{disk}} > \Delta t_{\mathrm{nbod}}$. Therefore, after Δt_{disk} is evaluated in `DustPy`, it is rounded down to the nearest integral multiple of Δt_{nbod}. With the timestep determined, `DustPy` takes one step, and `SyMBAp` takes a number of $\Delta t_{\mathrm{disk}}/\Delta t_{\mathrm{nbod}}$ steps in parallel. Then, communication is made via MPI, where the data of the newly formed planetesimals (Section 4.2.3), the relevant gas and dust components (Section 4.2.4), and the rounded Δt_{disk} are passed from `DustPy` to `SyMBAp`, and, the data of the accreted pebbles (Section 4.2.4) are passed from `SyMBAp` to `DustPy`. Afterwards, `DustPy` and `SyMBAp` take their respective step(s) again in parallel and this process repeats until the simulation ends.

For the simulations with the disk gap at 10 au, $\Delta t_{\mathrm{nbod}} = 0.5$ yr is used and particles are removed if the heliocentric distance is less than 5 au or greater than 10^3 au. And, for the gap

Table 4.1: Summary of the combinations of parameters, the times required for each combination to reach t_0 that the first planetesimal was formed as well as the time when $0.1m_{\rm iso}$ is reached. As the mass of planetesimal is drawn randomly, there are some variations in the time required among the simulations with the same parameters. Further descriptions are in the respective sub-section.

r_0 (au)	δ	Time to t_0 ($\times 10^5$yr)	Time to $0.1m_{\rm iso}$ (t_0 + ... $\times$ 10^5yr)	Section
10	10^{-4}	$\{1.05, 1.11, 1.14, 1.14, 1.15\}$	$\{0.34, 0.26, 0.22, 0.24, 0.24\}$	4.3.1
10	10^{-5}	$\{0.93, 0.98, 1.03, 1.05, 1.06\}$	$\{0.51, 0.46, 0.37, 0.34, 0.37\}$	4.3.2
75	10^{-4}	$\{4.9, 5.2, 5.3, 5.6, 6.0\}$	$\{2.2, 1.9, 1.9, 1.4, 1.2\}$	4.3.3
75	10^{-5}	$\{4.5, 4.6, 4.6, 4.6, 5.1\}$	$\{3.1, 2.9, 3.0, 3.0, 2.4\}$	4.3.4

location of 75 au, $\Delta t_{\rm nbod} = 20$ yr is used and particles are removed if the heliocentric distance is less than 50 au instead. The additional subroutines for gas drag, type-I damping and migration, and pebble accretion are added to `SyMBAp` following the integration step in Matsumura et al. (2017) as

$$\mathcal{P}^{\tau/2}\mathcal{M}^{\tau/2}\mathcal{N}^{\tau}\mathcal{M}^{\tau/2}\mathcal{P}^{\tau/2}, \tag{4.31}$$

where the timestep $\tau = \Delta t_{\rm nbod}$, the operator $\mathcal{P}$ handles the effect of pebble accretion, $\mathcal{M}$ handles the effect of gas drag, type-I damping and migration, and $\mathcal{N}$ is the second-order symplectic integrator in the original `SyMBAp`. $\mathcal{P}$ and $\mathcal{M}$ operate in the heliocentric coordinates and $\mathcal{N}$ operates in the democratic heliocentric coordinates, therefore, coordinate transformations are done at each step.

In this work, two gap locations $r_0 = \{10, 75\}$ au and two values of the local diffusion parameter $\delta = \{10^{-4}, 10^{-5}\}$ are tested. Five simulations for each combination are conducted to minimize the statistical effect, i.e., a total of 20 simulations are conducted and presented in the next section.

4.3 Results

In each simulation, some time is required for the gap to attain the prescribed form and accumulate enough dust to trigger planetesimal formation by streaming instability. We define the time that the first planetesimal is realized as t_0 and Table 4.1 summarizes the time required to reach t_0 for each simulation. Since the masses of the planetesimals are drawn randomly, simulations with the same parameter may not reach t_0 at the same time and a small variation is recorded. Simulations end when $0.1m_{\rm iso}$ is reached and the respective times are also summarized in Table 4.1. Descriptions for each set of parameters are in the following sub-sections respectively.

4.3.1 Disk gap at 10 au and $\delta = 10^{-4}$

Fig. 4.3 shows the radial dust distribution of one of the five simulations at t_0, where the heat map shows the profile of the midplane dust density $\sigma_{\rm d}$ for difference dust mass $m_{\rm d}$. The drift and the fragmentation limits are shown by the green and blue lines respectively. It shows that the dust mass is only limited by the fragmentation limit ($\gg$ mm) at the pressure bump near 14 au. The

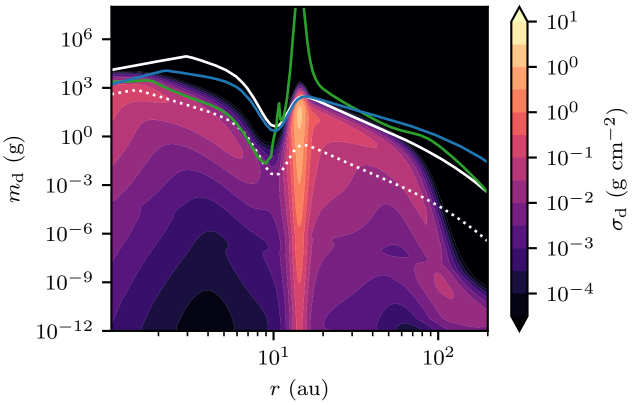

Figure 4.3: The dust distribution at t_0 of one of the five simulations for the disk gap at 10 au and $\delta = 10^{-4}$. The heat map shows the radial profile of the midplane dust density σ_d for difference dust mass m_d. The white lines show the m_d corresponding to St = 0.1 (solid) and 0.01 (dotted) respectively. The green and blue lines shows the drift and the fragmentation limits respectively. The dust mass is shown limited by the fragmentation limit ($\gg$ mm) at the dust trap near 14 au.

inward drifting dust from the outer disk is trapped and coagulation continues. Planet formation by streaming instability occurs as enough dust accumulates at the pressure bump.

Fig. 4.4 and 4.5 show the results of the five simulations for r_0 = 10 au and $\delta = 10^{-4}$. Figure 4.4a shows the radial profiles of the gas and dust surface densities as well as that of the dust-to-gas ratio when planetesimals start to form in one of the simulations. We note that there is no significant difference in the disk profiles among the simulations and the disk profiles did not change drastically up to the end of the simulations. The disk gap is shown centred at 10 au as prescribed and dust accumulates at the outer edge of the gap. Across the local pressure maximum, as shown by the radial profiles from one of the simulations in Fig 4.4b, both $\dot{M}_\mathrm{peb}$ and η cross zero and switch sign, where the negative values are denoted by the dashed lines. However, just outside of this narrow region, the peaks of $\dot{M}_\mathrm{peb}$ are almost up to $10^4 M_\oplus$ Myr^{-1} while η is still lower than 10^{-2} at the these two locations.

In Fig. 4.4c, panels i to iii show the mass and semimajor axis of the planetesimals at different times. The colours show the results from each of the five simulations and the bodies that reached $10^{-2} M_\oplus$ are denoted with large dots. In this case, the characteristic planetesimal mass $M_G \approx 3 \times 10^{-3} M_\oplus$ while there are small variations in time and distance as the disk is evolving slightly and the planetesimals do not form at the same location r. We define t_0 the time that the formation of planetesimals has just started. At t_0 (Fig. 4.4c i), just enough dust has accumulated at the pressure bump and planetesimal formation starts around the local pressure maximum at about 14.2 au. Planetesimals continue to form and some grow rapidly through pebble accretion as in Fig. 4.4c ii at $t_0 + 5 \times 10^3$ yr. The five simulations ended from $t_0 + 2.2 \times 10^4$ to $t_0 + 3.4 \times 10^4$ yr as $0.1 m_\mathrm{iso} \approx 4.1 M_\oplus$ is reached respectively (Fig. 4.4c iii). The narrow region with low pebble flux does not show significant effect in this setup. The coloured lines in Fig. 4.4c iii show the trajectories of the most massive body in each simulation. The massive planetary cores remain near the pressure bump with slight inward migration, which also started scattering the smaller

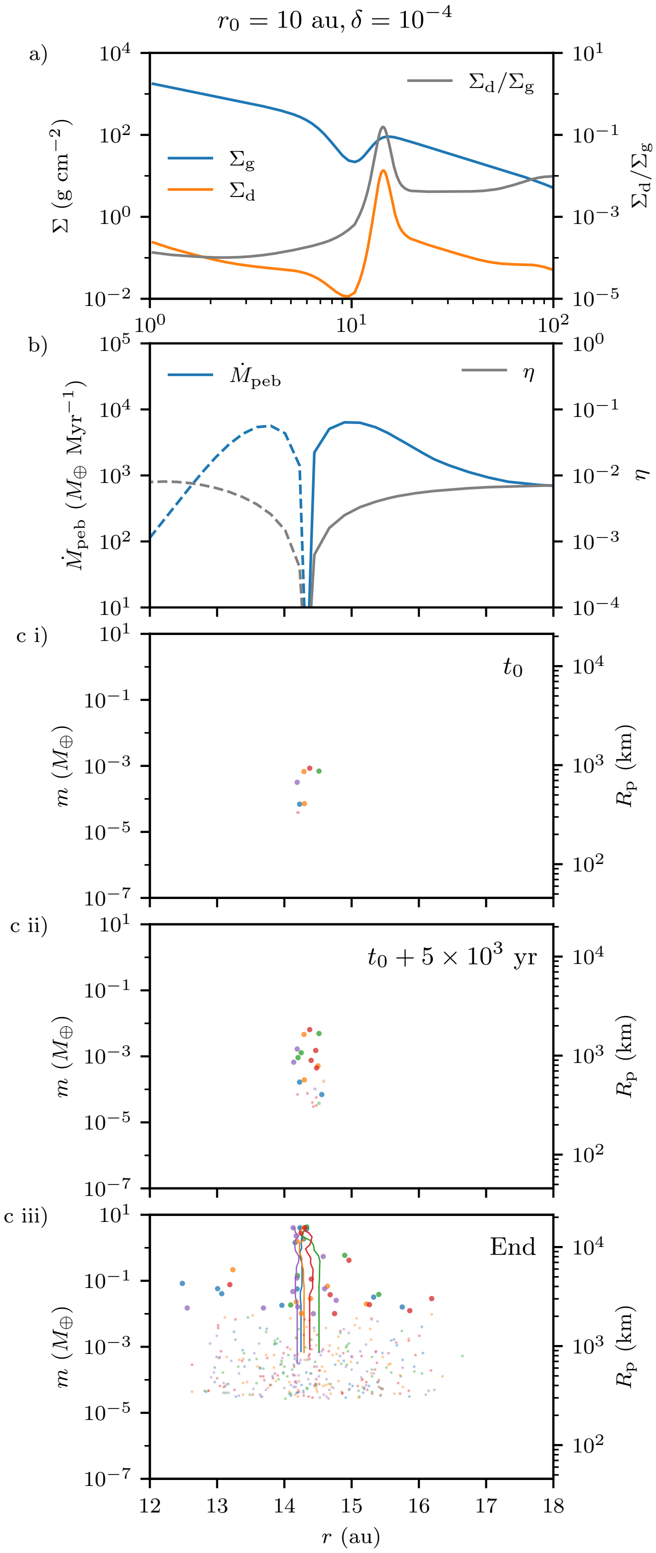

Figure 4.4: Simulation results for the disk gap at 10 au and $\delta = 10^{-4}$, where $M_G \approx 3 \times 10^{-3} M_\oplus$. **a)** The radial profiles in one of the five simulations of the dust and gas surface densities as well as the dust-to-gas ratio at t_0 when planetesimal formation starts. **b)** Pebble flux $\dot{M}_{\rm peb}$ and the pressure support parameter η around the pressure bump from one of the five simulations, where the dashed lines denote negative values. **c)** Time sequence of mass m and semimajor axis r of the planetesimals. Planetesimals that reach $10^{-2} M_\oplus$ by the end are denoted with large dots. Each colour shows one of the five simulations, which ended from $t_0 + 2.2 \times 10^4$ to $t_0 + 3.4 \times 10^4$ yrs. Further descriptions are in the text.

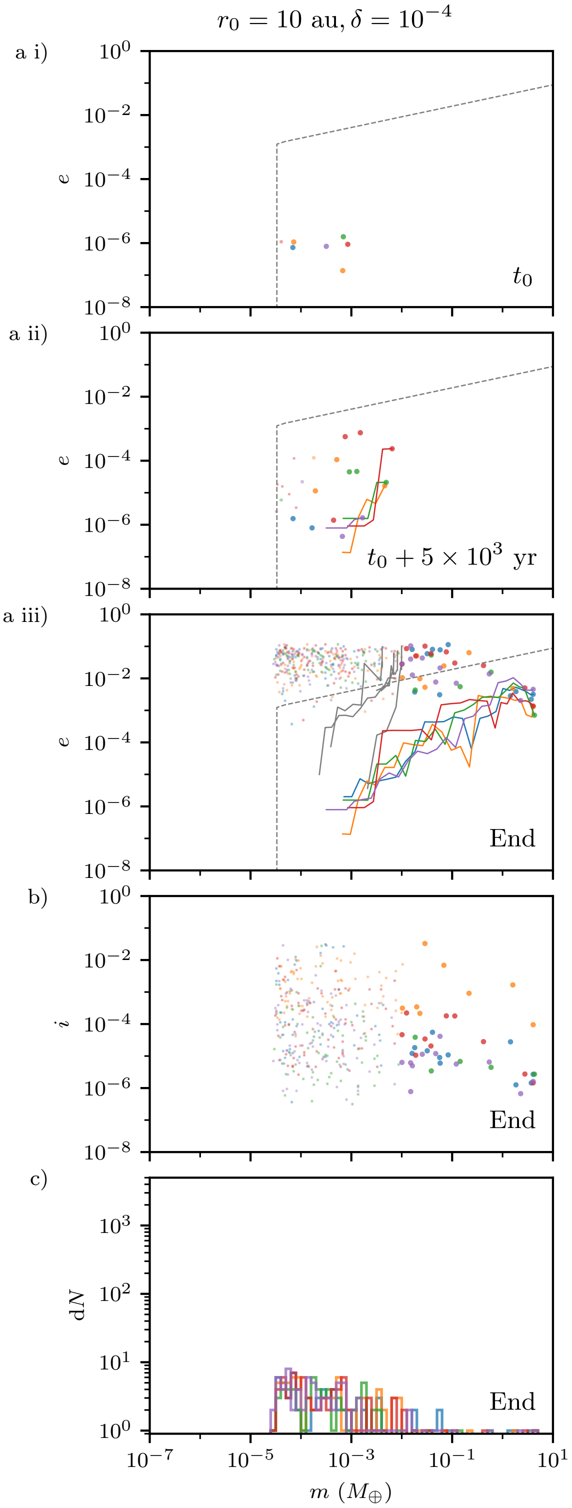

Figure 4.5: Further simulation results for the disk gap at 10 au and $\delta = 10^{-4}$. **a)** Time sequence of planetesimals eccentricity e and mass m. The coloured trajectories follow the most massive bodies and the grey trajectories follow the most massive ones under $10^{-2} M_\oplus$ in each of the simulations. The dashed lines denote the pebble accretion onset mass discussed in Section 4.4.2. **b)** Planetesimals inclination i and mass m at the end, where the i of most bodies are still lower than the pebble disk scale height. **c)** The differential mass distribution at the end of the model with 10 mass bins in each decade. It shows only a few massive cores are formed while the simulations stop before a large population of planetesimals are formed.

planetesimals.

Fig. 4.5 shows further details of the effect of viscous stirring. Panels a i to iii show the eccentricity and mass of the planetesimals at the respective times in Fig. 4.4c. In Fig. 4.5a, the trajectory of the most massive body at the end of each simulation is shown by the coloured line, and that for the most massive body with $m < 10^{-2} M_\oplus$ is shown by the grey line. The dashed line shows a pebble accretion onset mass assuming $\eta = 10^{-3}$ and $\mathrm{St} = 10^{-1}$, which is further discussed in Section 4.4.2. From Fig. 4.5a i to ii, the planetesimals formed early and close to the massive end of the distribution grow rapidly by pebble accretion and stir the latecomers. In Fig. 4.5a iii, the most massive body in each simulation has relatively low eccentricity throughout the entire time. The latecomers, which are born after an embryo has already grown significantly to $\sim M_\oplus$, are being stirred to high eccentricity as shown by the grey trajectories. This halted pebble accretion even though their inclinations are still lower than the pebble disk scale height as shown in Fig. 4.5b. Meanwhile, the role of gas drag has not shown its significance in the results likely due to the large ($\gtrsim$ 100km) size of the planetesimals in our model and the strong dynamical heating due to the rapidly-formed massive cores. The role of viscous stirring and pebble accretion is further discussed in Section 4.4.2.

The differential mass distributions at the end (Fig. 4.5c) show only a small number of massive cores ($\geq M_\oplus$) are formed in each of the simulations. In this setup, the simulations are quickly stopped as $0.1 m_{\mathrm{iso}}$ is reached shortly after only a small number of planetesimals were formed. The form of the initial mass distribution is not clearly shown even though most planetesimals did not grow significantly. We note that less than 10 mergers occurred in each of the simulations, which have no significant effect on the growth and the final mass of the bodies.

4.3.2 Disk gap at 10 au and $\delta = 10^{-5}$

Another set of five simulations with $r_0 = 10$ au and $\delta = 10^{-5}$ are conducted, in comparison to the results where $\delta = 10^{-4}$. As suggested by Eq. (4.17), the change of δ means that M_G is $10^{3/2}$, that is about 32 times, lower. With the characteristic mass $M_G \approx 9 \times 10^{-5} M_\oplus$, the number of planetesimals produced is much higher. The dust and gas surface densities, pebble flux and η have no significant difference with respect to the case of $\delta = 10^{-4}$ as other parameters are unchanged. The five simulations ended from $t_0 + 3.4 \times 10^4$ to $t_0 + 5.1 \times 10^4$ yr.

Fig. 4.6 shows the results of models with $\delta = 10^{-5}$. As previously, only the planetesimals which are formed early and massive can start pebble accretion right after formation. Similar to the case with $\delta = 10^{-4}$, these bodies grow efficiently and stir up the population of smaller planetesimals. The grey trajectories in Fig. 4.6a iii show more clearly that some small bodies could still grow briefly by pebble accretion from about $10^{-4} M_\oplus$ to just below $10^{-2} M_\oplus$ but further growth is halted due to their high eccentricities. Although the inclinations of the small planetesimals shown in Fig. 4.6b are not much higher than the pebble disk scale height, they cannot still accrete pebbles. Figure 4.6c shows that the majority of the planetesimal population did not grow significantly. The form of the initial mass distribution (Fig. 4.1) is retained and only a small number of massive cores are formed. In each of the simulations, about 200 mergers occurred, which is dominated by the massive cores accreting small planetesimals. The mass difference between the two populations is more than 4 orders of magnitude so these mergers have

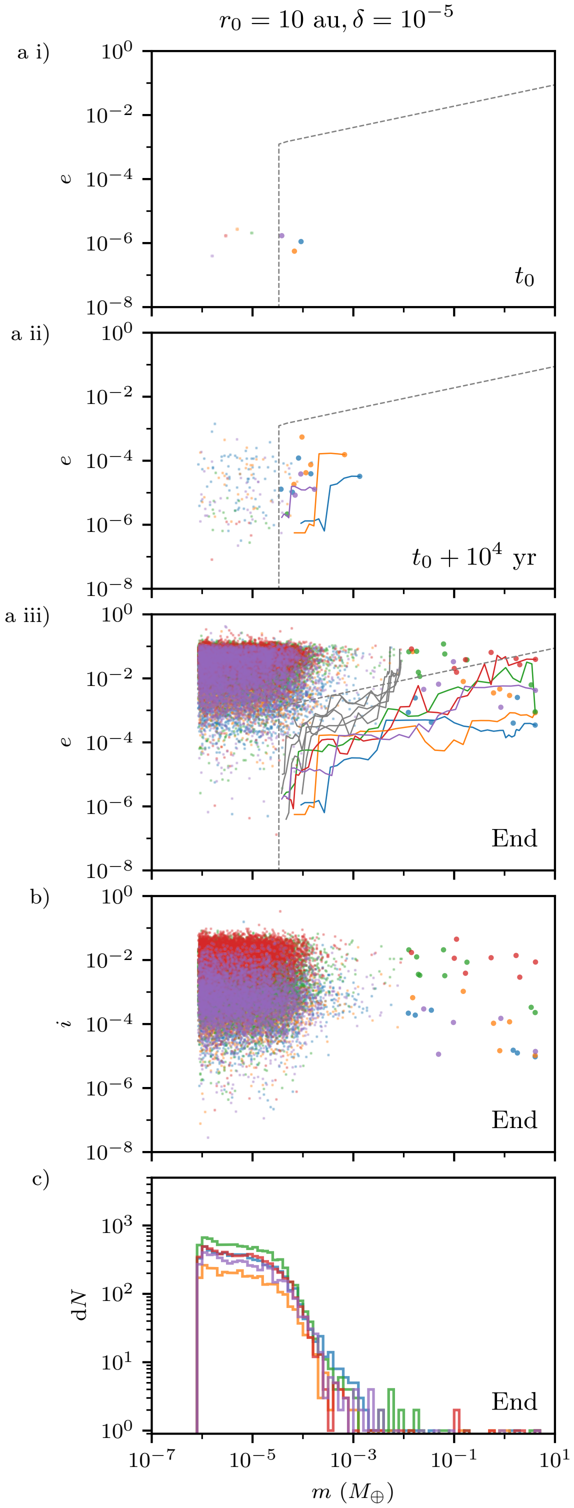

Figure 4.6: Simulation results for the disk gap at 10 au and $\delta = 10^{-5}$, which ended from $t_0 + 3.4\times10^4$ to $t_0 + 5.1\times10^4$ yr. **a)** The *e*-*m* time sequence shows only the planetesimals formed early and relatively massive can accrete pebbles efficiently and stir up the latecomers. **b)** The *i*-*m* plot at the end of the simulations shows that the inclinations of the small planetesimals are still not much larger than the pebble disk scale height. **c)** The differential mass distribution at the end shows the majority of the planetesimal did not grow significantly by pebble accretion and retain the form of the initial mass distribution as shown in Fig. 4.1. Only a small number of massive cores are formed in the simulations.

no significant effect on the final masses of the massive planetary cores.

4.3.3 Disk gap at 75 au and $\delta = 10^{-4}$

Figure 4.7 and 4.8 show the results of the five simulations for $r_0 = 75$ au and $\delta = 10^{-4}$. Figure 4.7a shows the pressure bump centring at 75 au as prescribed and the outer pressure maxima is at about 100 au. Compared to the setup with the disk gap at 10 au, Fig. 4.7b shows that the pebble flux is only slightly lower near the pressure bump while η is a few times higher in general. The five simulations ended from $t_0 + 1.2 \times 10^5$ to $t_0 + 2.2 \times 10^5$ yrs as $0.1 m_{\rm iso} \approx 17.2 M_\oplus$ is reached respectively. Similarly, the *m*-*r* time sequence (Fig. 4.7c) shows that the planetesimals formed early accrete pebbles efficiently and reach the pebble isolation mass in about 0.1 Myr. We note that M_G is similar to that for the simulations with $r_0 = 10$ au, which is due the increase in $\hat{h}_{\rm g}$ being mostly offset by the increase in the mass-averaged St.

Figure 4.8 shows further details of the results, which is again similar to the case of $r_0 = 10$ au and $\delta = 10^{-4}$ (Fig. 4.5). In the time sequence (Fig. 4.8a), the planetesimals formed early grow by pebble accretion at a slower but still rapid rate and stir the latecomers to eccentric orbits that stopped pebble accretion. Figure 4.8b shows that the inclinations of planetesimals remain even lower, which is around the values drawn at their realization. Nonetheless, the small bodies still cannot accrete pebbles due to high relative pebble velocity and only a small number of massive bodies are formed as shown in Fig. 4.8c.

4.3.4 Disk gap at 75 au and $\delta = 10^{-5}$

Figure 4.9 shows the results of the five simulations for $r_0 = 75$ au and $\delta = 10^{-5}$. The five simulations ended between $t_0 + 2.4 \times 10^5$ to $t_0 + 3.1 \times 10^5$ yr. Similar to the previous cases, only the planetesimals that formed early and relatively large can accrete pebbles efficiently similar to the case of $r_0 = 10$ au and $\delta = 10^{-5}$. The results also confirm that growth is dominated by the large embryos, which viscously stir the majority of the planetesimals. Pebble accretion again cannot operate for these excited bodies due to high pebble relative velocities even though their inclinations are much lower than the pebble disk scale height. In comparison to the case of $r_0 = 10$ au and $\delta = 10^{-5}$, a smaller numbers of larger embryos ($\geq M_\oplus$) are formed at the end.

4.4 Discussions

4.4.1 Pressure bump

The results presented in this work show that the environment in a pressure bump is favourable to the rapid formation of massive planetary cores in numerous possible ways, which is in agreement with the results by Morbidelli (2020); Guilera et al. (2020); Chambers (2021). First, dust drifting from the outer disk is trapped and accumulated at the exterior edge of the disk gap. This way a pebble passing the planet orbit without being accreted is not lost to the inner disk, but can be accreted at later passages. This circumvents the issue of large required pebble masses (Ormel

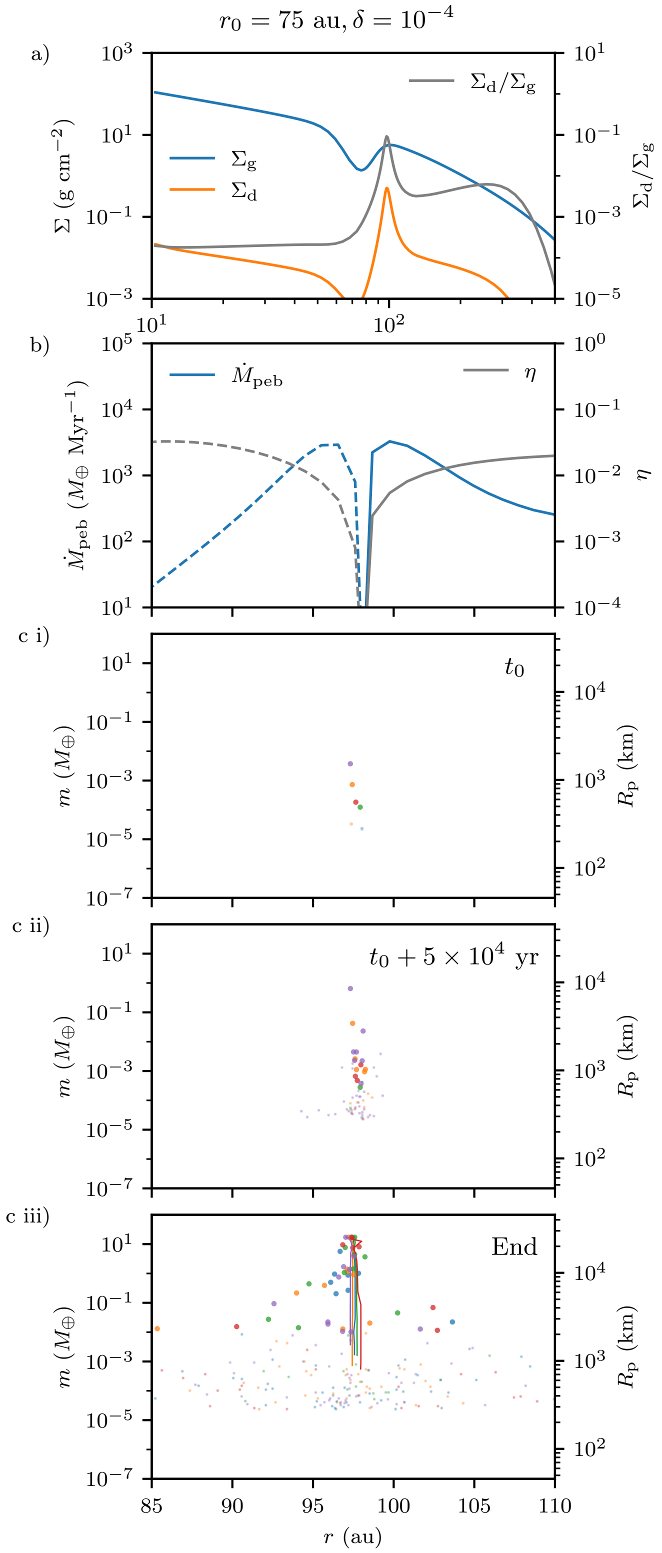

Figure 4.7: Simulation results for the disk gap at 75 au and $\delta = 10^{-4}$. **a)** The radial profiles of the disk when planetesimal formation starts. **b)** The radial profiles of pebble flux $\dot{M}_{peb}$ that it is still high around the pressure bump, yet slightly lower compared to the models at 10 au shown in Fig. 4.4b. The pressure support parameter η is generally a few times higher while the regions of low η still coincide with the peaks of the pebble flux. **c)** The *m*-*r* time sequence also shows similar results except the planetesimals are formed later and the grow rate is slower. The five simulations ended from $t_0 + 1.2 \times 10^5$ to $t_0 + 2.2 \times 10^5$ yrs.

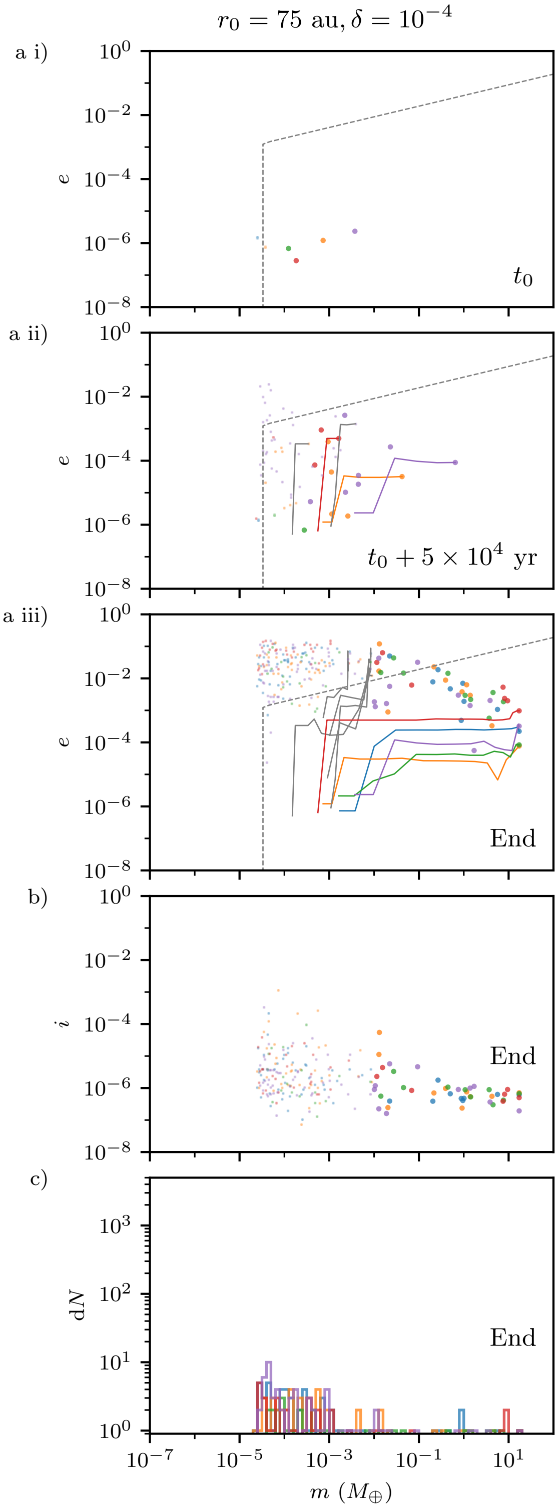

Figure 4.8: Further simulation results for the disk gap at 75 au and $\delta = 10^{-4}$. **a)** The *e*-*m* time sequence shows that a small number of massive cores are formed, which excite and prevent the growth of the latecomers. This is similar to the results to the case with $r_0 = 10$ au and $\delta = 10^{-4}$. **b)** The *i*-*m* plot at the end of the simulations shows that the inclinations remain very low for all bodies that is around the values drawn at their formation. **c)** The differential mass distribution at the end also shows only a small number of mass cores are formed and the simulations are stopped before a large population of planetesimals is produced. This is also similar to the case with $r_0 = 10$ au and $\delta = 10^{-4}$.

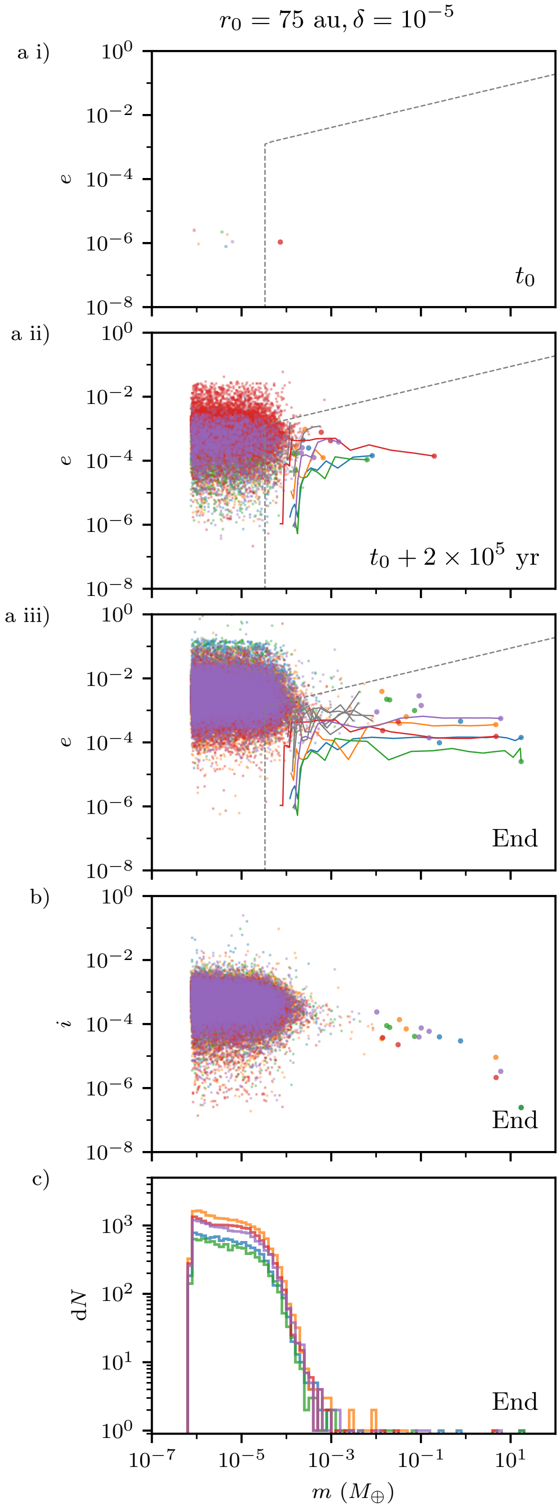

Figure 4.9: Simulation results for the disk gap at 75 au and $\delta = 10^{-5}$, which ended from $t_0 + 2.4 \times 10^5$ to $t_0 + 3.1 \times 10^5$ yrs. **a)** The *e*-*m* time sequence shows that a small number of massive embryos started growth early and stirred the majority of the lately-formed planetesimals into eccentric orbits. **b)** The *i*-*m* plot at the end of the simulations shows that the *i* of all bodies remain well lower than the pebble disk scale height and confirms that the pebble relative velocity is critical. **c)** Compared to the case of $r_0 = 10$ au and $\delta = 10^{-5}$, the differential mass distribution shows an even smaller number of massive cores formed in these simulations.

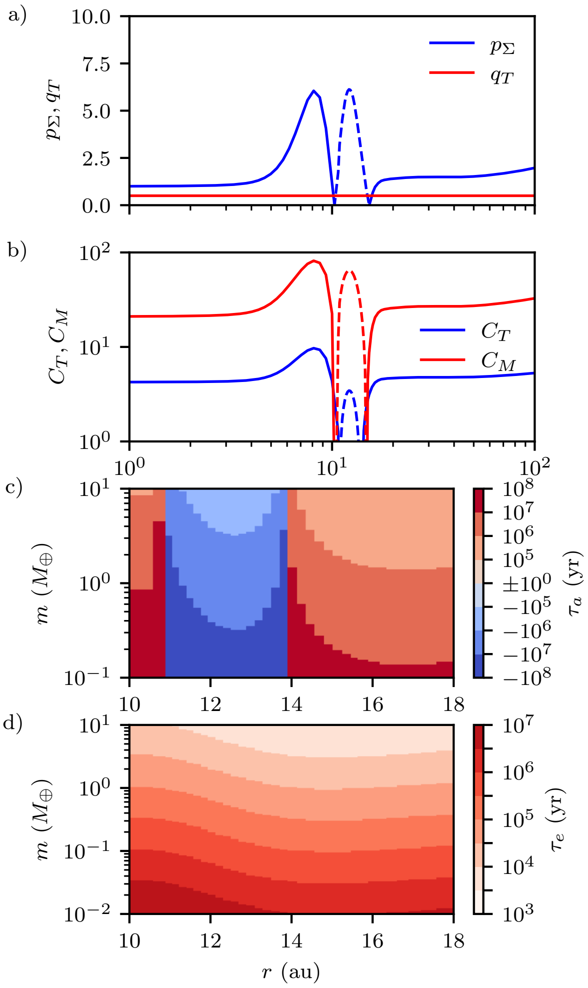

Figure 4.10: The radial profiles of the migration related parameters at the end of one of the simulations with $r_0 = 10$ au. **a)** q_T remains constant in our disk model while p_Σ varies greatly and changes sign across the pressure bump. **b)** The coefficients for τ_a also changes sign but at slightly different locations according to Eq. (4.24) & (4.25) respectively. **c)** τ_a near the pressure bump for an embryo of different masses with $e = 10^{-3}$ and $i = e/2$, where inward migration is denoted by red and outward migration is denoted by blue. The migration rate slows down and changes sign slightly interior ($\approx$ 14 au) to the location of planetesimal formation ($\approx$ 14.2 au). **d)** τ_e at the same locations, which is $\propto t_{\rm wav} \propto m^{-1}$. This shows type-I damping starts to become efficient when the embryos is $\gtrsim 10^{-1} M_\oplus$.

2017). Secondly, as the mid-plane dust-to-gas ratio gradually increases, it can reach the critical level for streaming instability. The grain sizes are also just limited by the fragmentation limit ($\gg$ mm). Therefore, planetesimal formation by streaming instability is possible in this specific environment. The planetesimals are formed within the regions of high pebble density and can accrete them efficiently.

Furthermore, the headwind, which carries the dust or pebbles, is slower around the pressure bump. In the headwind regime, the pebble relative velocity is mostly determined by $\eta v_{\rm K}$, which is applicable to a dynamically cold planetesimal belt. The pebble accretion onset mass in this case can be estimated by (Visser & Ormel 2016; Ormel 2017)

$$M_{\rm PA,hw} = {\rm St}\,|\eta|^3 M_*. \tag{4.32}$$

In both cases of $r_0 = 10$ au and 75 au, η at the location of the peak of the pebble flux is a few times lower than the value of it in a smooth disk. This greatly decreases the required mass for efficient pebble accretion particularly in the outer disk as $\eta \propto \hat{h}_{\rm g}^2$. Combining the decreased $M_{\rm PA,hw}$ and the enhanced $\dot{M}_{\rm peb}$, the planetesimals formed early that are well in the headwind regime can easily initiate rapid growth by pebble accretion. In our setup, the growth timescale in the settling regime at the pressure bump is $\sim 10^3 - 10^4$ yr for $r_0 = 10$ au and it is a few times higher for $r_0 = 75$ au.

We note that $\dot{M}_{\rm peb}$ is tiny in the immediate vicinity of the peak of the pressure bump in our model, where the pebble drift velocity switches sign and crosses zero with η. This results from our assumptions that pebbles are only supplied by radial drift due to the headwind in the disk. In a more realistic scenario, pebbles are also transported by turbulent diffusion. This effect is negligible when the headwind dominates the supply of pebbles. However, at the pressure bump, the headwind changes direction and is weak within a narrow region (e.g. Fig. 4.4b & 4.7b). In this case, turbulent diffusion can supply pebbles to this region such that the pebble flux is always finite and smooth. Although these effects are modelled by `DustPy` in the disk, the prescription of the pebble accretion efficiency by Liu & Ormel (2018) and Ormel & Liu (2018) is yielded from a model with a finite headwind, which ranges from $15 - 60 {\rm ms}^{-1}$. It remains uncertain if the same prescriptions can be applied to pebbles transported by turbulent diffusion as well as the relative radial motion of the embryo. Therefore, in this work, we only consider the pebble flux due to the headwind in the disk, which is proportional to $|\eta|$, which would result in a more conservative pebble accretion rate.

Nonetheless, this region of small $\dot{M}_{\rm peb}$ did not show significant effect likely due to the finite width and the dynamical spreading of the planetesimal belt. The value of $\dot{M}_{\rm peb}$ is also exceptionally high ($> 10^3 M_\oplus$ Myr^{-1}) just outside of this region. However, the width of this low pebble flux zone shall change with the shape of the disk gap, which may cause more significant effect on the growth of the planetesimals with a different prescription.

In other works adopting a smooth disk model, as the embryos become massive, the rapid type-I migration has been shown causing these bodies to quickly move to the inner disk. However, in our model with the pressure bump, these massive planetary cores are retained similar to the results of planet migration in structured disk in Coleman & Nelson (2016a). In the adopted migration prescription for an embryo with low eccentricity and inclination the sign of τ_a is determined by the coefficient $C_{\rm T}$ in Eq. (4.20). And, $C_{\rm T}$ is given by Eq. (4.25), which depends on

p_Σ and q_T. Figure 4.10 shows the migration parameters at the end of one of the simulations with $r_0 = 10$ au as an example, where τ_a and τ_e are calculated assuming $e = 10^{-3}$ and $i = e/2$. In our disk model, q_T is constant throughout the disk while p_Σ varies greatly and switches sign across the pressure bump as shown in Fig. 4.10a. This implies that C_T also switches sign and is negative slightly interior to the pressure maximum (Fig. 4.10b). As the migration direction changes from inward to outward going into the pressure bump from the exterior (Fig. 4.10c), this helps retaining the massive embryos at wide orbits as shown in our results in Section 4.3. Nonetheless, we note that the mass dependence of the migration trap (e.g. Chrenko et al. 2022) is not studied in our work since gas accretion and gap opening, which shall occur upon the formation of massive planetary cores, are not considered in our model.

4.4.2 Pebble accretion and viscous stirring

When a planetesimal is in an eccentric orbit, the pebble relative velocity is no longer dominated by the headwind but by the planetesimal's orbital velocity instead. In the adopted pebble accretion prescription by Liu & Ormel (2018) and Ormel & Liu (2018), the azimuthal pebble relative velocity is given by

$$\Delta v_y = \max(v_\mathrm{cir}, v_\mathrm{ecc}), \tag{4.33}$$

where v_cir combines the headwind and the Hill regimes in the circular limit. And, v_ecc corresponds to the eccentric limit that $v_\mathrm{ecc} = 0.76 e v_\mathrm{K}$. For small planetesimals, pebble accretion mostly does not operate in the Hill regime. Therefore, the pebble accretion onset mass in Eq. (4.32) can be refined into a more general form that

$$M_\mathrm{PA} = \mathrm{St}\,[\max(|\eta|, 0.76e)]^3 M_*. \tag{4.34}$$

This mass is denoted by the dashed line in the e-m plots in Section 4.3 assuming $\mathrm{St} = 0.1$ and $\eta = 10^{-3}$.

The shear-dominated (low-energy) regime of viscous stirring (Ida & Makino 1993) is applicable as the e_m and i_m of the newly-born latecomers are very low before reaching the equilibrium values. The stirring timescale for eccentricity is much shorter than that for inclination and dynamical friction is ineffective (Ida 1990). This is more significant in the results for $\delta = 10^{-4}$ where $e \ll i$ in general even at the end of the simulations. And, in the results for $\delta = 10^{-5}$, the excitation in e occurred much earlier than that for i as well while the equipartition of energy is only reached in some of the simulations. In this regime, the protoplanet-planetesimal viscous stirring timescale for eccentricity is given by (Ida & Makino 1993)

$$\tau_{\mathrm{vs},e}^{M-m} = 7.20 \times 10^3 \left(\frac{M}{M_\oplus}\right)^{-1/2} \left(\frac{a}{10\ \mathrm{au}}\right)^{3/2} \left(\frac{e_{m,\mathrm{rms}}}{5 \times 10^{-3}}\right)^3 \mathrm{yr}, \tag{4.35}$$

with $e_{m,\mathrm{rms}}$ the root-mean-square value of e_m and the mass of the protoplanet M. When a massive embryo has formed, the latecomers are stirred to high eccentricities within a very short timescale. Any newly formed planetesimals are excited to high eccentricity quickly, which results in a $M_\mathrm{PA} \gg M_\mathrm{PA,hw}$ for them. As a result, pebble accretion cannot operate even if the latecomers have mass greater than $M_\mathrm{PA,hw}$.

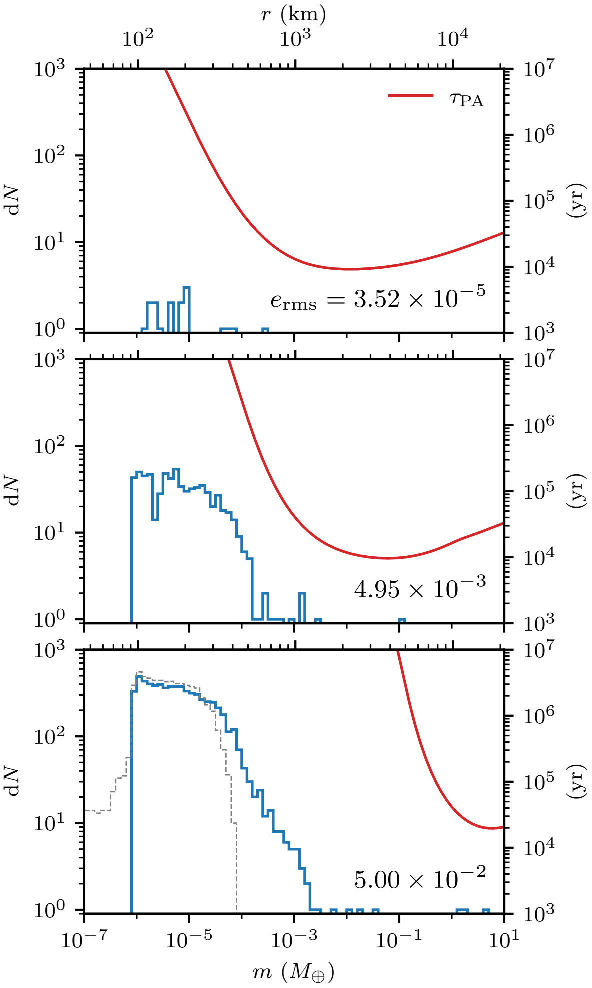

Figure 4.11: The differential mass distribution from one of the simulations with $r_0 = 10$ au and $\delta = 10^{-5}$ at $t_0 + 5 \times 10^4$ yr (top), $t_0 + 2 \times 10^5$ yr (middle) and $t_0 + 3.7 \times 10^5$ yr (bottom) with 10 mass bins in each decade. The red line in each panel shows the corresponding estimation of the pebble accretion timescale $\tau_{\rm PA}$ with respect to mass for the instantaneous $e_{\rm rms}$ of all bodies. The grey histogram in the bottom panel shows the initial mass of all planetesimals produced throughout the simulation. The evolution shows a window period exists that significant growth by pebble accretion is possible. This period starts from the time of the formation of the first planetesimal with $m > M_{\rm PA,hw}$ and ends at the time when it becomes massive enough to excite the less massive bodies to high eccentricity in a short timescale.

Meanwhile, the e of the massive bodies are being damped efficiently by the type-I torques as $\tau_e \propto t_{\rm wav} \propto m^{-1}$, which enable continuous pebble accretion. In the example for $r_0 = 10$ au as shown in Fig. 4.10d, type-I damping gradually becomes significant ($\lesssim 10^6$ yr) for $m \gtrsim 10^{-1} M_\oplus$. Thus, the latecomers are prevented from pebble accretion as a result of both viscous stirring from the massive planet formed earlier and the inefficient type-I damping.

This also implies that a window period exists between the time of the formation of the first planetesimal with $m > M_{\rm PA,hw}$ and the time when it becomes massive enough to halt pebble accretion for the less massive bodies. During this window period, a few of the planetesimals formed with $m > M_{\rm PA} \sim M_{\rm PA,hw}$ can still grow by a few orders of magnitude in mass as shown in our results.

For example, Fig. 4.11 shows the evolution of the differential mass distribution of one of the simulations with $r_0 = 10$ au and $\delta = 10^{-5}$. The red line in each panel shows the corresponding pebble accretion timescale $\tau_{\rm PA} \equiv m/\dot{m}$ with respect to m. $\tau_{\rm PA}$ is estimated near the centre of the planetesimal belt at 14.2 au using the root-mean-square eccentricity of all bodies $e_{\rm rms}$. The estimation also assumes $\dot{M}_{\rm peb} = 10^3 M_\oplus$ Myr^{-1} and St $= 0.1$. The top panel, at $t_0 + 5 \times 10^4$ yr, shows that when a massive body has not formed and $e_{\rm rms}$ is low, $M_{\rm PA} = M_{\rm PA,hw}$ is about $10^{-4} M_\oplus$ where $\tau_{\rm PA} \sim 10^4$ yr. Rapid growth is possible for the bodies in the massive end of the planetesimal mass distribution. As a few embryos grow significantly in mass and excite $e_{\rm rms}$ to above 0.76η, the eccentric limit of pebble accretion becomes applicable. The middle panel, at $t_0 + 2 \times 10^5$ yr, shows that $M_{\rm PA}$ starts to shift away from the majority of the planetesimals. The leading bodies dominate growth and the bottom panel, at $t_0 + 3.7 \times 10^5$ yr, shows that the small planetesimals are further excited and $M_{\rm PA}$ increases drastically. The grey histogram shows the distribution of the initial mass of all planetesimals produced throughout the simulation. The bodies of $\gtrsim 10^{-3} M_\oplus$ were born within the window period such that the masses had grown by at least an order of magnitude before $M_{\rm PA}$ overtook them.

The exact number of massive cores formed by the end of the simulations is then also determined by the rate of planetesimal formation, which has not been explored in this work. Since the transition between the headwind and the eccentric limits becomes critical in this scenario, the expression for Δv_y in Eq. (4.33) merits further refinements for a smoother and more physical expression.

We note that this mechanism is conceptually different from the ‘viscous stirring pebble accretion’ in Levison et al. (2015), where pebble accretion for smaller bodies is stalled due to high inclinations. In our model, the pebble disk scale height for each dust species is given by Eq. (4.8), which is about $0.32 H_{\rm g}$ for $\alpha = 10^{-3}$ and St = 0.1. And, in the results presented in Section 4.3, the inclinations of the small bodies have not been stirred greatly away from the pebble disk in general but pebble accretion is already effectively stopped by the increased pebble relative velocity.

4.4.3 Characteristic mass M_G

The characteristic mass of the initial planetesimal mass distribution given by Eq. (4.17) is sensitive to the small-scale diffusion parameter that $M_G \propto \delta^{3/2}$. We only tested the values of $\delta = \{10^{-4}, 10^{-5}\}$ due to computational limit while the measurements by Schreiber & Klahr (2018) range from $10^{-4} - 10^{-6}$. A strong dependence on the simulation domain size is also shown in their work.

Since planetesimal accretion is inefficient in our parameter space, pebble accretion is only possible for the planetesimals with large enough mass initially. For the results of $\delta = 10^{-4}$ shown in Section 4.3.1 & 4.3.3, $M_G > M_{\rm PA,hw}$. In this case, planetesimals that are formed slightly later than the first one can still accrete pebble and grow by at least an order of magnitude in mass. And, $0.1 m_{\rm iso}$ is reached only after a small population of planetesimals have formed. The form of the initial mass distribution cannot be retrieved from the end results. In contrast, for $\delta = 10^{-5}$ shown in Section 4.3.1 & 4.3.3, $M_G \sim M_{\rm PA,hw}$. Fewer bodies are formed with mass between the most massive cores and the vast population of small planetesimals. The distinction between these two classes is much clearer. As a result, the initial planetesimals distribution is mostly presented and preserved in this case.

Although the rapid formation of massive planetary cores are possible in the parameters tested, we expect that for a very low δ, pebble accretion may not occur as $M_G \ll M_{\rm PA,hw}$. And, the timescale of runaway planetesimal accretion is given by (Ormel et al. 2010)

$$\tau_{\rm rg} = 5.45 \times 10^7 \left(\frac{m}{10^{-5} M_\oplus}\right)^{1/3} \left(\frac{M_*}{M_\odot}\right)^{-1/2} \left(\frac{\Sigma_{\rm plts}}{10 \text{ g cm}^{-2}}\right)^{-1} \times \left(\frac{\rho_{\rm s}}{1.5 \text{ g cm}^{-3}}\right)^{2/3} \left(\frac{a}{100 \text{ au}}\right)^{3/2} \text{yr}. \tag{4.36}$$

Planetesimal accretion is also unlikely to be efficient enough to reach $M_{\rm PA,hw}$ within the typical disk lifetime particularly at the outer disk. This will likely result in a population of planetesimals with the initial mass distribution preserved. This consequence is also consistent with the recent work by Lorek & Johansen (2022) that the seeds for pebble accretion are unlikely to form through planetesimal accretion beyond 5-10 au within the typical disk lifetime.

4.4.4 Potential effects of a planet in the disk gap

In this work, a planet in the disk gap is not considered while the results show the growth of planetesimals by pebble accretion is also sensitive to viscous stirring. This implies that if there exists a planet in the gap, the planetesimal belt formed at the pressure bump may be heated and prevented from growth by pebble accretion. For instance, the fitting of a planet-induced gap in the simulations by Kanagawa et al. (2017) has a half width $\propto m^2$. Meanwhile, the half width of the heated zone of a planet (Ida & Makino 1993) scales with its Hill radius that $\propto m^{1/3}$. This implies that there may exist a regime transition as the gap-opening planet grows in mass because the gap expands faster than the heated zone. However, the exact width of the heated zone also depends on the e and i of the planetesimals as shown in Ida & Makino (1993). This requires further modellings that include gas accretion and feedback onto the gas disk. For instance, our model neglects the effect of the recently proposed thermal torque mainly due to heat released from solid accretion (Benítez-Llambay et al. 2015; Masset 2017; Guilera et al. 2021) and the effect of the dust torque (Benítez-Llambay & Pessah 2018).

4.4.5 Other recent works

Planet growth by pebble accretion in substructured disk is also studied by Morbidelli (2020). In this work, the dust ring is assumed to be in a steady-state, which is described by a Gaussian distribution. It shows that planet may migrate slightly inwards but out of the dust-concentrated region, where growth by pebble accretion is significantly slowed down. In comparison, the dust-to-gas ratio in our model is much higher at the outer edge of the disk gap (e.g. Fig. 4.4a & 4.7a). Since the disk gap is only prescribed towards the gas component, the dust component evolves around it and results in a much higher dust density at the pressure bump. Also, Morbidelli (2020) adopted a migration prescription for a non-isothermal disk, in contrast to our model. Since the coefficients of the migration torque are different between the isothermal and non-isothermal cases, the planet trap locates at a different location. Further investigations on the effect of migration in the context of substructured disks and planetary growth are required.

In the work by Guilera et al. (2020), planet formation in an ice-line (~ 3 au) induced pressure bump is also studied with a model that includes dust growth, planetesimal formation by streaming instability, pebble accretion and planet migration. In this model, a uniform initial radius of 100 km for the planetesimals is adopted. When an embryo reaches lunar mass, the effects of pebble accretion, gas accretion and planet migration are enabled for it. The rapid formation of massive planetary cores is also demonstrated and the pressure bump acts as a planet trap for planet with mass $\lesssim 10 M_\oplus$. In comparison, we adopted a distribution of initial planetesimal mass and demonstrated the effect of viscous stirring on pebble accretion by full N-body simulations. However, the initial planetesimal mass adopted in our work is generally much larger. The effect of planetesimal accretion is not noticeable due to the greater distance from the star. Once a massive core is formed, the neighbouring planetesimals are likely scattered and a new gap should form due to the planet-disk interactions, which changes the location of pressure bump.

Chambers (2021) studied the formation of cold Jupiter in a substructured disk starting with embryos of $\sim 10^{-4} M_\oplus$. A series of 8 pressure bumps is prescribed and the embryos are placed at the respective locations of ‘pebble trap’. In addition to pebble accretion, gas drag and the type-I torques, gas accretion and gap opening are also included in this model. Their results also show that massive planetary cores can form rapidly in pressure bump, which acts as a migration trap as well. Meanwhile, the production of planetesimals is not considered in this model, which is also favoured in pressure bump, and pebbles are added to the disk locally after 400 orbital periods. Since planetesimals are formed in a dust concentrated region, the ones above M_{PA} can immediately start pebble accretion as shown in our model.

In the recent work by Jiang & Ormel (2023), planetesimal growth in a clumpy ring and a pressure-induced dust ring are studied respectively. In their case, a constant mass flux is supplied from the outer disk and a single Stokes number is assumed for the pebbles. In contrast, in this present work, we modelled the dust and gas evolution of the entire protoplanetary disk where mass is conserved globally. We also include the variation in the Stokes numbers of different mass species at different locations, which is critical to the initial planetesimal mass distribution and the pebble accretion efficiency.

A similar pebble accretion efficiency prescription is adopted in their work. We note that the factor of $1/\eta$ from ϵ_{PA} is eliminated for the pebble accretion rate while $\eta = 0$ at the local pressure maximum. This implicitly assumed that the pebble flux due to the radial motion of the planet, turbulence in the disk and diffusion of the dust is equivalent to that due to the headwind. We discussed in Section 4.4.1 that the prescription of $\epsilon_{\rm PA}$ is yielded from models with non-zero headwind. Therefore, we have taken a more conservative approach by considering only the pebble flux due to the headwind for accretion in our work.

A migration prescription for a smooth disk with an artificial migration strength prefactor is adopted in their work. Meanwhile, in the prescription by Ida et al. (2020) adopted in this work, the local slopes of the surface density and temperature profiles are taken in account, which naturally stop inward migration slightly interior to but not exactly at the pressure bump. Nonetheless, we note that these prescriptions assume a local uniformity on the scale of $H_{\rm g}$. Further studies are required for a sharp pressure bump.

Their work also showed that pebble accretion is efficient with low eccentricity, which is consistent with our results for the massive planetary cores formed. In addition, with a mass spectrum of planetesimals, the smaller or lately-formed planetesimals are excited significantly and pebble accretion is halted as demonstrated in this work.

Jang et al. (2022) also studied the subsequent evolution of planetesimals formed by streaming instability in a smooth disk with a constant pebble flux. They modelled a planetesimal belt with a width of $\Delta r = \eta r$ respectively at different locations of the disk. Their results show that rapid growth by pebble accretion is not possible at the outer disk due to the strong headwind, which drastically increases the pebble accretion onset mass. In the results with type-I migration, they also show rapid inward migration for the embryos that reach $\sim 1 M_\oplus$. In contrast, as discussed in Section 4.4.1, planetesimals can still accrete pebbles efficiently in our results due to weakened headwind in the pressure bump. They are also retained near the pressure bump due to the change in the slope of the gas surface density.

4.5 Conclusions

This work demonstrated that the rapid formation of massive planetary cores in a pressure bump is possible starting from ISM-sized dust. The dust and gas evolution code `DustPy` is used to model a protoplanetary disk consistently. It is coupled to the parallelized N-body code `SyMBAp` to integrate a large number of planetesimals. According to the evolving disk, the planetesimals also experience the effects of gas drag, type-I migration and pebble accretion.

As the micron-sized dust particles coagulate up to the cm-m regime, the pressure bump traps the dust drifting from the outer disk. The locally enhanced dust-to-gas ratio can then trigger planetesimal formation by streaming instability. These km-sized planetesimals are naturally born in a location where the pebble flux is exceptionally large and the headwind is weakened. This allows the planetesimals which are formed early and relatively massive to grow efficiently by pebble accretion even in the outer disk. Only a small number of massive cores ($\sim M_\oplus$) are formed as the later-formed planetesimals are excited into eccentric orbits, where pebble accretion is halted. The massive embryos are retained near the dust trap as the direction of migration switches to outward migration slightly interior to the local pressure maximum. A natural continuation of this work is including gas accretion and feedback onto the protoplanetary disk in the model.

This shall provide further insights on the open questions regarding the architecture of the Solar System as well as those of other exoplanetary systems.

Nonetheless, the characteristic masses of the planetesimals adopted in this work are limited by computational costs. Since pebble accretion is unlikely to be efficient for even smaller planetesimals, it merits further analyses on the initial mass distribution of planetesimals resulting from streaming instability, which has been an active research topic, e.g. Simon et al. (2016, 2017); Schäfer et al. (2017); Abod et al. (2019); Li et al. (2019); Rucska & Wadsley (2020).

As pebble accretion may not operate in a heated planetesimal belt due to high pebble relative velocity, a pre-existing planet in the gap may immediate excite the newly formed planetesimals. This depends on the width of the gap and that of the heated zone. A planet-induced gap is not considered and the shape of the disk gap is also not explored in this work. These ingredients of our model require further investigations.

Acknowledgments

We thank Chris Ormel and Beibei Liu for the insightful discussions. We acknowledge funding from the European Research Council (ERC) under the European Union's Horizon 2020 research and innovation programme under grant agreement No 714769 and funding by the Deutsche Forschungsgemeinschaft (DFG, German Research Foundation) under grant 325594231 and Germany's Excellence Strategy - EXC-2094 - 390783311 and EXC 2181/1 - 390900948 (the Heidelberg STRUCTURES Excellence Cluster). JD was funded by the European Union under the European Union's Horizon Europe Research & Innovation Programme 101040037 (PLANETOIDS). Views and opinions expressed are however those of the authors only and do not necessarily reflect those of the European Union or the European Research Council. Neither the European Union nor the granting authority can be held responsible for them.

Chapter 5

Sequential giant planet formation initiated by disc substructure

Tommy Chi Ho Lau, Til Birnstiel, Joanna Drążkowska, and Sebastian Stammler

This chapter was published in Astronomy & Astrophysics, 688, A22 (2024)

Abstract: Planet formation models are necessary to understand the origins of diverse planetary systems. Circumstellar disc substructures have been proposed as preferred locations of planet formation, but a complete formation scenario has not been covered by a single model so far. We aim to study the formation of giant planets facilitated by disc substructure and starting with sub-micron-sized dust. We connect dust coagulation and drift, planetesimal formation, N-body gravity, pebble accretion, planet migration, planetary gas accretion, and gap opening in one consistent modelling framework. We find rapid formation of multiple gas giants from the initial disc substructure. The migration trap near the substructure allows for the formation of cold gas giants. A new pressure maximum is created at the outer edge of the planetary gap, which triggers the next generation of planet formation resulting in a compact chain of giant planets. A high planet formation efficiency is achieved, as the first gas giants are effective at preventing dust from drifting further inwards, which preserves material for planet formation. Sequential planet formation is a promising framework to explain the formation of chains of gas and ice giants.

5.1 Introduction

Planet formation is a multi-step process spanning over 40 orders of magnitude in mass. In recent years, there has been significant progress in the understanding of this process driven by the numerous discoveries of exoplanets and observations of protoplanetary discs (see Drążkowska et al. (2023) for a recent review). The formation of the first gravitationally bound building blocks of planets, the planetesimals, which used to be a major bottleneck of the planet formation theory, was addressed by the streaming instability (Johansen et al. 2007). The properties of planetesimals formed in the streaming instability broadly match comets and the Kuiper belt objects (Blum et al.

2017; Nesvorný et al. 2019). The growth timescale of giant planet cores, which was prohibitively long in the classical planetesimal-driven paradigm (Lissauer 1987; Kokubo & Ida 2000, 2002), has been addressed by introducing pebble accretion (Ormel et al. 2010; Lambrechts et al. 2014). Despite these new developments, a consistent model covering all the stages of planet formation does not exist yet. Formation of the cores of giant planets remains a challenge, particularly at large orbital distances (Voelkel et al. 2020; Coleman 2021; Eriksson et al. 2023).

Current planet formation models in general fail to meet both the physical and cosmochemical constraints required to explain the Solar System (e.g. Matsumura et al. 2017; Liu et al. 2019; Bitsch et al. 2019; Lau et al. 2024b). The main challenge remains to be the 'migration problem', where rapid migration occurs for planetary cores of 1 to 10 $M_{\oplus}$, resulting in the formation of super-Earths and hot Jupiters. While the above models generally assume a smooth planetary disc, multiple works (e.g. Coleman & Nelson 2016a; Morbidelli 2020; Guilera et al. 2020; Chambers 2021; Andama et al. 2022; Lau et al. 2022) have modelled the formation and evolution of planetary cores retained at the migration trap near a pressure bump in the disc. Nonetheless, the origin of such pressure bumps remains uncertain, the proposed non-planetary causes include late-stage infall of material (Gupta et al. 2023), sublimation (Saito & Sirono 2011), instabilities (Takahashi & Inutsuka 2014; Flock et al. 2015; Dullemond et al. 2018), and the edge of the dead zone, where the magneto-rotational instability (MRI) is suppressed (Pinilla et al. 2016).

More recently, the high-resolution interferometry observations by the Atacama Large Millimeter/submillimeter Array (ALMA) have shown that substructures are typical in protoplanetary discs. Multiple surveys (e.g. Andrews et al. 2018; Long et al. 2018; Cieza et al. 2021), have shown that most of the substructures are presented in the form of axisymmetric rings. While these observations are limited to large and bright discs, disc population synthesis and theoretical models (Toci et al. 2021; Zormpas et al. 2022) have demonstrated that disc substructures may be common in unresolved discs as well.

Chatterjee & Tan (2013) presented an analytic model demonstrating the 'inside-out' planet formation scenario, where planet formation starts at the outer edge of the MRI active zone around the star. Although this work focuses on explaining the tightly packed chains of planets commonly seen in exoplanetary systems, the model suggests the possibility of planet formation being triggered by the planet formed in the previous generation. A similar idea was also proposed for the formation of Saturn after the completion of Jupiter (Kobayashi et al. 2012), in which the core of Saturn grows rapidly without significant inward drift in the pressure bump induced by the planetary gap of Jupiter, although they did not consider planetesimal formation from dust and pebble accretion.

Motivated by the current models and observations, a substructure in a protoplanetary disc has recently emerged as an ideal location for planet formation (Chambers 2021; Lau et al. 2022; Jiang & Ormel 2023). Lau et al. (2022) modelled the formation and evolution of planetesimals in an initial axisymmetric disc substructure by coupling the dust and gas evolution code DustPy (Stammler & Birnstiel 2022) with the parallelised symplectic N-body integrator SyMBA parallelised (SyMBAp; Lau & Lee 2023). As the disc evolves and satisfies the condition for the streaming instability and the subsequent gravitational collapse, a fraction of the dust is converted into planetesimals as N-body particles. On top of the full N-body gravitational interactions, additional subroutines are gas drag, planet-disc interactions, and pebble accretion. Lau et al. (2022)

showed the rapid formation of planetary cores thanks to the concentrated dust, which are also retained due to the migration trap near the pressure bump. However, this work did not attempt to form giant planets, as the authors focused on the formation of planetary cores, where gas accretion and planetary gap opening are missing in the model.

In this work, we further developed the model in Lau et al. (2022) for the formation of giant planets initiated by a disc substructure and found a scenario of sequential planet formation. In the following, Sec. 5.2 summarises the methods adopted in Lau et al. (2022) and the new components implemented in this work. The results are presented in Sect. 5.3, which are followed by the discussions in Sect. 5.4. The findings of this work are summarised in Sect. 5.5.

5.2 Method

We employed the dust and gas evolution code DustPy v1.0.3 (Stammler & Birnstiel 2022) and the symplectic N-body integrator SyMBAp v1.6 (Lau & Lee 2023), a parallelised version of the Symplectic Massive Body Algorithm (SyMBA; Duncan et al. 1998). The coupling of the two codes to construct a consistent planet formation model was first presented in Lau et al. (2022), which only modelled the formation of planetary cores. In this work, we added gas accretion and planetary gap opening to model the subsequent evolution of the embryos formed at a pressure bump. The following summarises the employed method in Lau et al. (2022) and describes the new components in detail.

5.2.1 Disc model

DustPy simulates the viscous evolution of the gas, coagulation, fragmentation, advection, and diffusion of the dust in a protoplanetary disc. The different parts of the disc model are described in this section.

Gas component

We considered a protoplanetary disc around a solar-type star, which is axisymmetric and in vertical hydrostatic equilibrium. The initial gas surface density $\Sigma_{\rm g,init}$ is given by

$$\Sigma_{\rm g,init} = \frac{M_{\rm disc}}{2\pi r_{\rm c}^2}\left(\frac{r}{r_{\rm c}}\right)^{-1}\exp\left(-\frac{r}{r_{\rm c}}\right), \tag{5.1}$$

with the distance from the star r, the initial mass of the disc $M_{\rm disc}$, and the characteristic radius $r_{\rm c}$. We set $M_{\rm disc} = 0.0263 M_{\odot}$ and $r_{\rm c} = 50$ au, which imply $\Sigma_{\rm g,init}$ ($r = 5$ au) ≈ 134.6 g cm^{-2}.

The gas disc viscously evolves in time t according to the advection-diffusion equation

$$\frac{\partial \Sigma_{\rm g}}{\partial t} = \frac{3}{r}\frac{\partial}{\partial r}\left[r^{1/2}\frac{\partial}{\partial r}(\nu \Sigma_{\rm g} r^{1/2})\right] \tag{5.2}$$

(Lüst 1952; Lynden-Bell & Pringle 1974), while the backreaction from the dust is neglected. The Shakura & Sunyaev (1973) α-parametrisation was adopted for the kinematic viscosity ν such that

$$\nu = \alpha c_{\mathrm{s}} H_{\mathrm{g}}, \tag{5.3}$$

with the speed of sound c_{s} and the disc scale height H_{g}. The viscosity parameter $\alpha = \{3, 5\} \times 10^{-4}$ was set in this work. The disc scale height is defined by $H_{\mathrm{g}} \equiv c_{\mathrm{s}}/\Omega_{\mathrm{K}}$, where the local Keplerian orbital frequency $\Omega_{\mathrm{K}} = \sqrt{GM_{\odot}/r^3}$ with the gravitational constant G. The isothermal sound speed was used and given by $c_{\mathrm{s}} = \sqrt{k_{\mathrm{B}}T/\mu}$ with the Boltzmann constant k_{B}, the midplane temperature T and the mean molecular weight of the gas $\mu = 2.3m_{\mathrm{p}}$. The disc was assumed to be passively irradiated by the solar luminosity at a constant angle of 0.05, which gives a midplane temperature profile

$$T \approx 221 \left(\frac{r}{\mathrm{au}}\right)^{-1/2} \mathrm{K}. \tag{5.4}$$

We note that the normalisation is about 0.84 of that in Lau et al. (2022), which is the result of a correction made to DustPy since v1.0.2. This setup yields the dimensionless gas disc scale height

$$\hat{h}_{\mathrm{g}} \equiv \frac{H_{\mathrm{g}}}{r} \approx 0.0299 \left(\frac{r}{\mathrm{au}}\right)^{1/4}. \tag{5.5}$$

The midplane pressure gradient parameter η is then given by

$$\eta = -\frac{\hat{h}_{\mathrm{g}}^2}{2} \frac{\partial \ln P}{\partial \ln r}, \tag{5.6}$$

with the midplane gas pressure P, which describes the degree of 'sub-Keplerity' of the gas. A logarithmic radial grid was adopted with with 133 cells from 3 to 53 au and with an additional 42 cells from 53 to 1000 au.

Dust component

The initial dust surface density $\Sigma_{\mathrm{d,init}}$ is given by

$$\Sigma_{\mathrm{d,init}} = Z\Sigma_{\mathrm{g,init}} \tag{5.7}$$

with the global dust-to-gas ratio Z set at the solar metallicity of 0.01. We followed Mathis et al. (1977), that is, the MRN size distribution of the interstellar medium, for the initial size distribution of the dust grains. The maximum initial size was set at 1 μm with the internal density of 1.67 g cm^{-3} assumed. A total of 141 dust mass bins logarithmically spaced from 10^{-12} to 10^{8} g were used. Each dust species was evolved in time through transport with the advection-diffusion equation (Clarke & Pringle 1988) coupled to growth and fragmentation with the Smoluchowski equation. The fragmentation velocity was assumed to be 5 ms^{-1}. At collision velocities above which, the dust aggregates are assumed to fragment. The Stokes number St_i of the dust in each dust species i was calculated by considering the Epstein and the Stokes I regimes. The dust scale height of each dust species $H_{\mathrm{d},i}$ was calculated according to Dubrulle et al. (1995),

$$H_{\mathrm{d},i} = H_{\mathrm{g}} \sqrt{\frac{\alpha}{\alpha + \mathrm{St}_i}}, \tag{5.8}$$

assuming $\mathrm{St}_i < 1$. Further details of the algorithms for the disc model are described in Stammler & Birnstiel (2022).

Initial disc gap

An initial axisymmetric gap was introduced to the disc following the model by Dullemond & Penzlin (2018), which is motivated by the commonly observed substructures in protoplanetary discs. To modify the gas profile, we applied a modified α-parameter with radial dependence $\alpha'(r) = \alpha/F(r)$, where the function

$$F(r) = \exp\left[-A \exp\left(-\frac{(r-r_0)^2}{2w^2}\right)\right] \tag{5.9}$$

with the gap amplitude $A = 1$, the location $r_0 = 5.5$ au and the gap width $w = 0.5$ au. The initial gap is removed when the first planet has the gap opening factor K (Kanagawa et al. 2015b) of 250. The K factor is further described in Sect. 5.2.3 on planetary gap opening. This value translates to a perturbation towards the gas disc of about 1/10 of the unperturbed gas surface density.

Since we do not study the physical cause of the initial disc gap, the modified $\alpha'(r)$-parameter only serves the purpose to attain a target gas profile and does not change the actual turbulence in the disc. Therefore, the modified α-parameter $\alpha'(r)$ is exclusively experienced by the gas, while dust diffusion, dust scale height and turbulent collision speeds are set by α. Nonetheless, the dust evolves according to the resulting gas profile. We note that this treatment is not consistent with the substructure formation scenarios where the actual turbulence is changed, for example, the edge of the dead-zone, but consistent with the cases where the turbulence is unchanged, for example, infall of material.

Planetesimal formation

Lau et al. (2022) adopted the truncated power-law cumulative mass distribution from the fitting by Abod et al. (2019). However, the upper end of the distribution is not limited and Lau et al. (2024b) noted that the largest planetesimal in the actual realisation depends on the total number of planetesimals. Therefore, here we adopted the Toomre-like instability criterion Q_p for the gravitational collapse of the dense filament induced by streaming instability and the initial mass function from Gerbig & Li (2023). The criterion for collapse is $Q_\mathrm{p} < 1$ with

$$Q_\mathrm{p} = \sqrt{\frac{\delta}{\mathrm{St}_{avg}}} \frac{c_\mathrm{s}\Omega}{\pi G \Sigma_\mathrm{d,local}}, \tag{5.10}$$

and the mass-averaged Stokes number of the dust in the cell St_{avg}. The local dust surface density $\Sigma_\mathrm{d,local}$ was assumed to be 10 times of the averaged Σ_d of the cell. Motivated by the streaming instability simulations in Schreiber & Klahr (2018), the small-scale diffusion parameter δ was set at 10^{-5}. The model converts dust into planetesimals based on the prescription by Drążkowska

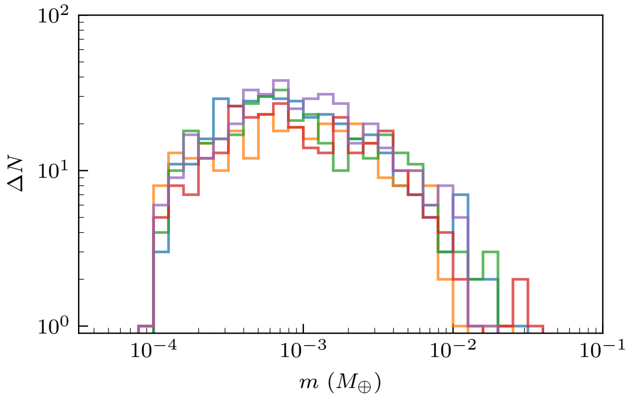

Figure 5.1: Differential mass distribution of the planetesimals formed near the initial disc substructure for the set of simulations with $\alpha = 5 \times 10^{-4}$ drawn from the adopted initial mass function by Gerbig & Li (2023). There are 10 bins per decade in mass m and ΔN is the number of planetesimals in each bin. Each colour corresponds to one of the five simulations.

et al. (2016) and Schoonenberg et al. (2018). The Q_p criterion was combined with the smooth planetesimal formation activation function from Miller et al. (2021), which is given by

$$\mathcal{P}_\mathrm{pf} = \frac{1}{1 + \exp\left[10 \times (Q_\mathrm{p} - 0.75)\right]}, \tag{5.11}$$

and evaluated at each radial grid cell. If any cell also satisfies the criterion of $\rho_\mathrm{d}/\rho_\mathrm{g} \geq 1$, the local dust surface density for each dust species i is reduced by

$$\frac{\partial \Sigma_{\mathrm{d},i}}{\partial t} = -\mathcal{P}_\mathrm{pf} \Sigma_{\mathrm{d},i} \frac{\zeta}{t_{\mathrm{set},i}}. \tag{5.12}$$

The planetesimal formation efficiency per settling time is $\zeta = 10^{-3}$ and the settling time of dust species i is $t_{\mathrm{set},i} \equiv 1/(\mathrm{St}_i \Omega_\mathrm{K})$.

Then, the removed dust is summed over all dust species and added to the local planetesimal mass surface density. We first draw the location of a new planetesimal using the radial profile of the planetesimal mass surface density. Then, we draw the planetesimal mass according to the initial mass function given by Gerbig & Li (2023), which is resulting from the stability analysis of the dispersion relation for dust influenced by turbulent diffusion (Klahr & Schreiber 2021). The maximum and minimum masses associated with the unstable modes are given by

$$m_\mathrm{max,min} = \frac{9}{8}\sqrt{\frac{\pi}{2}}\left(\frac{\delta}{\mathrm{St}_\mathrm{avg}}\right)^{3/2} \hat{h}_\mathrm{g}^3 \left(\frac{1}{Q_\mathrm{p}} \pm \sqrt{\frac{1}{Q_\mathrm{p}^2} - 1}\right)^2 M_\odot, \tag{5.13}$$

and the fastest-growing mode is given by

$$m_{\rm fgm} = \frac{9}{8}\sqrt{\frac{\pi}{2}}\left(\frac{\delta}{{\rm St}_{avg}}\right)^{3/2} \hat{h}_{\rm g}^3 Q_{\rm p}^2 M_\odot \tag{5.14}$$

$$\approx 0.37\left(\frac{\delta/10^{-5}}{{\rm St}_{avg}/0.1}\right)^{3/2}\left(\frac{\hat{h}_{\rm g}}{0.05}\right)^3\left(\frac{Q_{\rm p}}{1}\right)^2 M_{\rm Ceres}, \tag{5.15}$$

assuming isotropy in the small-scale diffusion. We refer the readers to Eq. (20) in Gerbig & Li (2023) for the expression of the probability density function. Figure 5.1 shows an example of the differential mass distribution of the planetesimals formed at about 6.5 au near the initial disc substructure for the set of simulations with $\alpha = 5 \times 10^{-4}$.

As described in Lau et al. (2022), the eccentricity e and the inclination i in radian are randomly drawn from two Rayleigh distributions with the scale parameters 10^{-6} and 5×10^{-7} respectively. The rest of the angles of the orbital elements in radian are drawn randomly from 0 to 2π. The physical radius $R_{\rm p}$ is calculated by assuming an internal density $\rho_{\rm s}$ of 1.5 g cm^{-3}. The drawn mass is subtracted from the surface density from the nearest radial grid cells and the realisation stops when the total remaining mass is less than the drawn mass. Any residue of the planetesimal mass surface density and the last drawn value of planetesimal mass is retained for the next time step to avoid bias towards the lower mass, that is, the drawn mass will be realised as soon as enough planetesimal surface density is available.

5.2.2 Planetesimal evolution

The realised planetesimals, and a Solar-mass star, were then evolved by SyMBAp with full gravitational interactions as well as additional subroutines to include gas drag, the planet-disc interactions, pebble accretion, gas accretion and planetary gap opening. If two bodies collide, they were assumed to merge completely, that is, collisions are perfectly inelastic. At each communication step, on top of the newly formed planetesimals, the radial profiles of the disc were passed to SyMBAp. This included the gas components:

- the gas surface density $\Sigma_{\rm g}$;
- the midplane temperature T;
- the gas disc scale height $H_{\rm g}$;
- the midplane gas density $\rho_{\rm g}$, and;
- the midplane pressure gradient parameter η,

and the dust component, for each dust species i,:

- the Stokes number ${\rm St}_i$;
- the dust disc scale height $H_{{\rm d},i}$, and;

- the dust surface density $\Sigma_{\mathrm{d},i}$.

Also, the feedback to the disc was also passed to DustPy including

- the dust mass loss due to pebble accretion (Sect. 5.2.2);
- the gas mass loss due to gas accretion (Sect. 5.2.2), and;
- the change in gas surface density due to planetary gap opening (Sect. 5.2.3),

which are further described in the respective subsections.

Pebble accretion

The treatment for the pebble accretion rate of each planetesimal is identical to that presented in Lau et al. (2022) and summarised below. First, the pebble mass flux of dust species i at any location is given by

$$\dot{M}_{\mathrm{peb}} = 2\pi r v_{\mathrm{drift},i}\Sigma_{\mathrm{d},i}. \tag{5.16}$$

The pebble drift speed of dust species i is $v_{\mathrm{drift},i} = 2\mathrm{St}_i|\eta|r\Omega_{\mathrm{K}}$ (Weidenschilling 1977). Then, we implemented the pebble accretion efficiency factor $\epsilon_{\mathrm{PA},i}$ by Liu & Ormel (2018) and Ormel & Liu (2018) to calculate the fraction of the local pebble mass flux being accreted by each planetesimal or planet for dust species i. The pebble accretion rate by a planetesimal or a planet is then given by summing the contributions from all dust species, which is

$$\dot{m}_{\mathrm{pa}} = \sum_i \epsilon_{\mathrm{PA},i} 2\pi r v_{\mathrm{drift},i}\Sigma_{\mathrm{d},i}. \tag{5.17}$$

The mass of the accreted pebbles is then subtracted from the respective dust species and radial cell of the dust disc at the next immediate communication step.

We did not implement the pebble isolation mass explicitly with a prescription (e.g. Lambrechts et al. 2014) in this work. Instead, as dust and gas evolve consistently in this model, the planetary gap opening by a planet (Sect. 5.2.3) can interrupt the pebble flux capturing the process of pebble isolation within the model.

Gas accretion

We followed Piso & Youdin (2014) and Bitsch et al. (2015b) to prescribe the gas accretion rate with the modification by Chambers (2021) to account for the energy released from pebble accretion. Gas accretion generally begins when the energy released from pebble accretion decreases enabling the cooling of the gas envelope. The gas accretion rate in this phase is

$$\begin{aligned}\dot{m}_{\mathrm{cool}} = \max\Bigg[0, 4.375\times10^{-9}\left(\frac{\kappa}{\mathrm{cm^2\ g^{-1}}}\right)^{-1}\left(\frac{\rho_{\mathrm{c}}}{5.5\ \mathrm{g\ cm^{-3}}}\right)^{-1/6}\times \\ \left(\frac{m_{\mathrm{c}}}{M_{\oplus}}\right)^{11/3}\left(\frac{m_{\mathrm{env}}}{M_{\oplus}}\right)^{-1}\left(\frac{T}{81\mathrm{K}}\right)^{-1/2} M_{\oplus}\mathrm{yr}^{-1} - 15\dot{m}_{\mathrm{pa}}\Bigg]\end{aligned} \tag{5.18}$$

with the opacity of the gas envelope κ and the density of the core $\rho_c = 5.5$ g cm^{-3}. We note that the solid mass accreted from planetesimal accretion is negligible compared to pebble accretion in our simulations. We followed Brouwers et al. (2021) for the grain size near the Bondi radius of the gas envelope to calculate its Rosseland mean opacity. Assuming the Epstein regime, the incoming solids converge to the size

$$R = \frac{\rho_g v_{th} v_{frag}}{g_B \rho_\bullet}, \tag{5.19}$$

with the midplane gas density ρ_g, the thermal velocity v_{th}, the gravity at the Bondi radius g_B and the monomer density $\rho_\bullet = 1.67$ g cm^{-3}. The Rosseland mean opacity is given by

$$\kappa = \frac{3 Q_{eff} \rho_d}{4 \rho_\bullet R \rho_g} \tag{5.20}$$

with the midplane dust density ρ_d. The extinction efficiency is $Q_{eff} = \min(0.6\pi R_s/\lambda_{peak}, 2)$ with the peak wavelength of the emission given by

$$\lambda_{peak} = \frac{0.29 \text{ cm}}{T/K}, \tag{5.21}$$

where the temperature T is assumed to be the local disc midplane temperature.

When the gas envelope m_{env} exceeds the solid core mass m_c, gas accretion enters the runway phase following the treatment by Bitsch et al. (2015b). The gas accretion rate in this phase is determined by the gas stream flowing towards the planet (Tanigawa & Tanaka 2016), which is

$$\dot{m}_{runaway} = 0.29 \Sigma_g r^2 \Omega_K \left(\frac{m}{M_\odot} \right)^{4/3} \hat{h}_g^{-2} \tag{5.22}$$

with the planet mass m. The accreted gas is then subtracted from the gas disc assuming the half-width of the accretion zone equals twice the Hill radius of the planet.

Physical radius

As the planetesimals or planets grow by many orders of magnitude in mass, the physical radius R_p is evaluated correspondingly. For mass m less than 0.1 Earth mass, we assumed an internal density ρ_s of 1.5 g cm^{-3}, which is the same when the planetesimals are formed. For m above 0.1 $M_\oplus$ but less than 5 $M_\oplus$, we followed Seager et al. (2007) for the mass-radius relationship of rocky planets, which is

$$\log\left(\frac{R_p}{3.3 R_\oplus}\right) = -0.209 + \frac{1}{3}\log\left(\frac{m}{5.5 M_\oplus}\right) - 0.08\left(\frac{m}{5.5 M_\oplus}\right)^{0.4} \tag{5.23}$$

with the radius of Earth $R_\oplus$. For m above 5 $M_\oplus$, we followed the mass-radius relationship applied in Matsumura et al. (2017), which is

$$R_p = 1.65 \sqrt{\frac{m}{5 M_\oplus}} R_\oplus. \tag{5.24}$$

5.2.3 Planetary gap opening

For all planetesimals and planets, the non-dimensional gap opening factor (Kanagawa et al. 2015b) was evaluated, which is given by

$$K = \left(\frac{m}{M_\odot}\right)^2 \hat{h}_{\rm g}^{-5} \alpha^{-1}. \tag{5.25}$$

Since the treatment in Sect. 5.2.1 to attain a target gas profile does not change the actual turbulence experienced by the dust and we only consider the torque exerted on the gas disc, planetary gap opening was applied through the modified α'-parameter. When $K > 0.25$, we impose a planetary gap to the gas disc by dividing α' by the ratio of the perturbed surface density to the unperturbed one $\Sigma_{\rm g}/\Sigma_{\rm g,0}$. In other words, the planetary gap is imposed when the change caused by the corresponding body is more than about 1% of the unperturbed surface gas density.

The effects on α' were multiplied when more than one planet can open a gap, that is, for all gap opening planets i

$$\alpha' = \frac{\alpha}{F \cdot \prod_i \left(\Sigma_{\rm g}/\Sigma_{\rm g,0}\right)_i}, \tag{5.26}$$

with the function to impose the initial disc gap F (see Eq. (5.9)).

We note that some small but short-period chaotic movements of massive planets can prevent the disc from converging to a quasi-steady state and the speed of code is significantly reduced. Therefore, we allowed $\alpha'(r)$ to reach the target value exponentially on a relaxation timescale of $250 \times (10^{-3}/\alpha)$ years, which is below the viscous evolution timescales of the disc in the adopted radial domain of the simulations.

We adopted the empirical formula by Duffell (2020) for the gap profile, which is

$$\frac{\Sigma_{\rm g}}{\Sigma_{\rm g,0}} = \left(1 + \frac{0.45}{3\pi} \frac{\tilde{q}^2(r)}{\alpha \hat{h}_{\rm g}^5} \delta(\tilde{q}(r))\right)^{-1} \tag{5.27}$$

with $\hat{h}_{\rm g}$ evaluated at the planet's location. The radial profile function $\tilde{q}(r)$ is defined by

$$\tilde{q}(r) \equiv \frac{q}{\left\{1 + D^3 \left[(r/r_{\rm p})^{1/6} - 1\right]^6\right\}^{1/3}} \tag{5.28}$$

with the mass ratio $q \equiv m/M_\odot$, the planet's radial distance from the star $r_{\rm p}$ and the scaling factor $D \equiv 7\hat{h}_{\rm g}^{-3/2}\alpha^{-1/4}$. The function $\delta(x)$ is given by

$$\delta(x) = \begin{cases} 1 + (x/q_w)^3, & \text{if } x < q_{\rm NL} \\ \sqrt{q_{\rm NL}/x} + (x/q_w)^3, & \text{if } x \geq q_{\rm NL} \end{cases} \tag{5.29}$$

with the factor $q_{\rm NL} = 1.04\hat{h}_{\rm g}^3$ and the factor $q_w = 34 q_{\rm NL}\sqrt{\alpha/\hat{h}_{\rm g}}$. We note that there is a minor discrepancy in the form of $\delta(x)$ for the case of $x < q_{\rm NL}$ between the text and the Python code presented in Duffell (2020). We confirm that the expression given above by Eq. (5.29) is consistent with the mentioned Python code, which is continuous and more appropriate (private communication, Duffell, 2022).

5.2.4 Gas drag and planet-disc interactions

All bodies experience the combined effects of aerodynamic gas drag and the planet-disc interactions. For low-mass planet without gap opening, the treatment for gas drag and planet-disc interaction are identical to that presented in Lau et al. (2022) and summarised below.

We adopt the aerodynamic gas drag by Adachi et al. (1976), which is

$$\boldsymbol{a}_{\mathrm{drag}} = -\left(\frac{3C_{\mathrm{D}}\rho}{8R_{\mathrm{p}}\rho_{\mathrm{s}}}\right) v_{\mathrm{rel}}\boldsymbol{v}_{\mathrm{rel}} \tag{5.30}$$

with the drag coefficient C_{D} and, the relative velocity between the planetesimal and the gas $\boldsymbol{v}_{\mathrm{rel}}$. The gas flow is assumed to be laminar and cylindrical, where the magnitude is given by $r\Omega_{\mathrm{K}}(1-|\eta|)$. As the planetesimals in this work are well larger than a kilometre in size, the large Reynolds number case is generally applicable, that is, $C_{\mathrm{D}} = 0.5$ (Whipple 1972). The gas density ρ at the planetesimal's position z above the midplane is given by $\rho = \rho_{\mathrm{g}} \exp(-0.5z^2/H_{\mathrm{g}}^2)$.

For type-I damping and migration, we adopted the prescription based on dynamical friction by Ida et al. (2020). The timescales for the isothermal case and finite i, while $i < \hat{h}_{\mathrm{g}}$, (Appendix D of Ida et al. (2020)) were implemented. The evolution timescales of semimajor axis, eccentricity and inclination are defined, respectively, by

$$\tau_a \equiv -\frac{a}{\mathrm{d}a/\mathrm{d}t}, \tau_e \equiv -\frac{e}{\mathrm{d}e/\mathrm{d}t}, \tau_i \equiv -\frac{i}{\mathrm{d}i/\mathrm{d}t}. \tag{5.31}$$

These timescales are given by, with $\hat{e} \equiv e/\hat{h}_{\mathrm{g}}$ and $\hat{i} \equiv i/\hat{h}_{\mathrm{g}}$,

$$\tau_a = \frac{t_{\mathrm{wav}}}{C_{\mathrm{T}}\hat{h}_{\mathrm{g}}^2}\left[1 + \frac{C_{\mathrm{T}}}{C_{\mathrm{M}}}\sqrt{\hat{e}^2 + \hat{i}^2}\right], \tag{5.32}$$

$$\tau_e = 1.282 t_{\mathrm{wav}}\left[1 + \frac{(\hat{e}^2 + \hat{i}^2)^{3/2}}{15}\right], \tag{5.33}$$

$$\tau_i = 1.838 t_{\mathrm{wav}}\left[1 + \frac{(\hat{e}^2 + \hat{i}^2)^{3/2}}{21.5}\right]. \tag{5.34}$$

The characteristic time t_{wav} (Tanaka et al. 2002) is given by

$$t_{\mathrm{wav}} = \left(\frac{M_\odot}{m}\right)\left(\frac{M_\odot}{\Sigma_{\mathrm{g}} r^2}\right)\left(\frac{\hat{h}_{\mathrm{g}}^4}{\Omega_{\mathrm{K}}}\right), \tag{5.35}$$

where Σ_{g} and $\hat{h}_{\mathrm{g}}$ are retrieved from the local radial cell of the disc model. The normalised torques C_{M} and C_{T} are given by

$$C_{\mathrm{M}} = 6(2p_\Sigma - q_T + 2), \tag{5.36}$$

$$C_{\mathrm{T}} = 2.73 + 1.08p_\Sigma + 0.87q_T, \tag{5.37}$$

with $p_\Sigma \equiv -\mathrm{d}\ln\Sigma_{\mathrm{g}}/\mathrm{d}\ln r$ and $q_T \equiv -\mathrm{d}\ln T/\mathrm{d}\ln r$. The three timescales were then applied to the equation of motion

$$\boldsymbol{a} = -\frac{v_{\mathrm{K}}}{2\tau_a}\boldsymbol{e}_\theta - \frac{v_r}{\tau_e}\boldsymbol{e}_r - \frac{v_\theta - v_{\mathrm{K}}}{\tau_e}\boldsymbol{e}_\theta - \frac{v_z}{\tau_i}\boldsymbol{e}_z \tag{5.38}$$

in the cylindrical coordinates (r, θ, z) that the velocity of the embryo $\boldsymbol{v} = (v_r, v_\theta, v_z)$. And, the local Keplerian velocity v_K was evaluated at the instantaneous r of the particle.

As the planet grows and opens a gap in the disc, Kanagawa et al. (2018) suggested that the magnitude of the torque scales linearly with the local surface density providing a smooth transition to the high-mass (type-II) regime of planet migration. Since the dependence of $t_{\mathrm{wa}v}$ on Σ_g as in Eq. (5.35) is retrieved from the local grid cell, the above treatment combined with gap opening (Sect. 5.2.3) can already capture this transition.

We note that planetary gap opening (Sect. 5.2.3) and planet migration are the results of planet-disc interactions, which are physically coupled by the action-reaction pair. However, we have adopted two independent prescriptions for each of them since a prescription for a torque profile which is suitable for a one-dimensional model and a general planet mass is still missing. Further discussions on the adopted treatments are in Sect. 5.4.4.

5.2.5 Numerical setup

The time step for SyMBAp $\tau = 0.2$ yr was used and particles were removed if the heliocentric distance is less than 4 au or greater than 100 au. The additional subroutines for the evolution of the N-body particles were added to SyMBAp as

$$\mathcal{P}^{\tau/2}\mathcal{M}^{\tau/2}\mathcal{N}^{\tau}\mathcal{M}^{\tau/2}\mathcal{P}^{\tau/2}. \tag{5.39}$$

The operator $\mathcal{P}$ handles the effect of pebble accretion, gas accretion and gap opening, $\mathcal{M}$ handles the effect of gas drag and planet-disc interactions, and $\mathcal{N}$ is the second-order symplectic integrator in the original SyMBAp. The operators $\mathcal{P}$ and $\mathcal{M}$ operate in the heliocentric coordinates and $\mathcal{N}$ operates in the democratic heliocentric coordinates so coordinate transformation is required at each step.

Since disc dissipation is not included in this work, all simulations stop at 2 Myr, which is the typical timescale that internal photoevaporation becomes significant to the disc (e.g. Owen et al. 2010, 2011; Picogna et al. 2019; Gárate et al. 2021). We note a numerical difficulty when multiple giant planets are produced, which causes multiple deep planetary gaps in the disc and a small integration time step is required for the disc. Each simulation requires a wall-clock time of 2 to 4 weeks. We tested two values of $\alpha = \{3, 5\} \times 10^{-4}$ and five simulations were conducted for each to evaluate the statistical effect.

5.3 Results

5.3.1 The case of $\alpha = 5 \times 10^{-4}$

Formation and evolution of massive bodies

Figure 5.2 presents one of the simulations with $\alpha = 5 \times 10^{-4}$ with the panels showing the six key timestamps. The solid and dashed lines show the profiles of the gas surface density Σ_g and the dust surface density Σ_d respectively. The dots show the mass m and the semimajor axis r

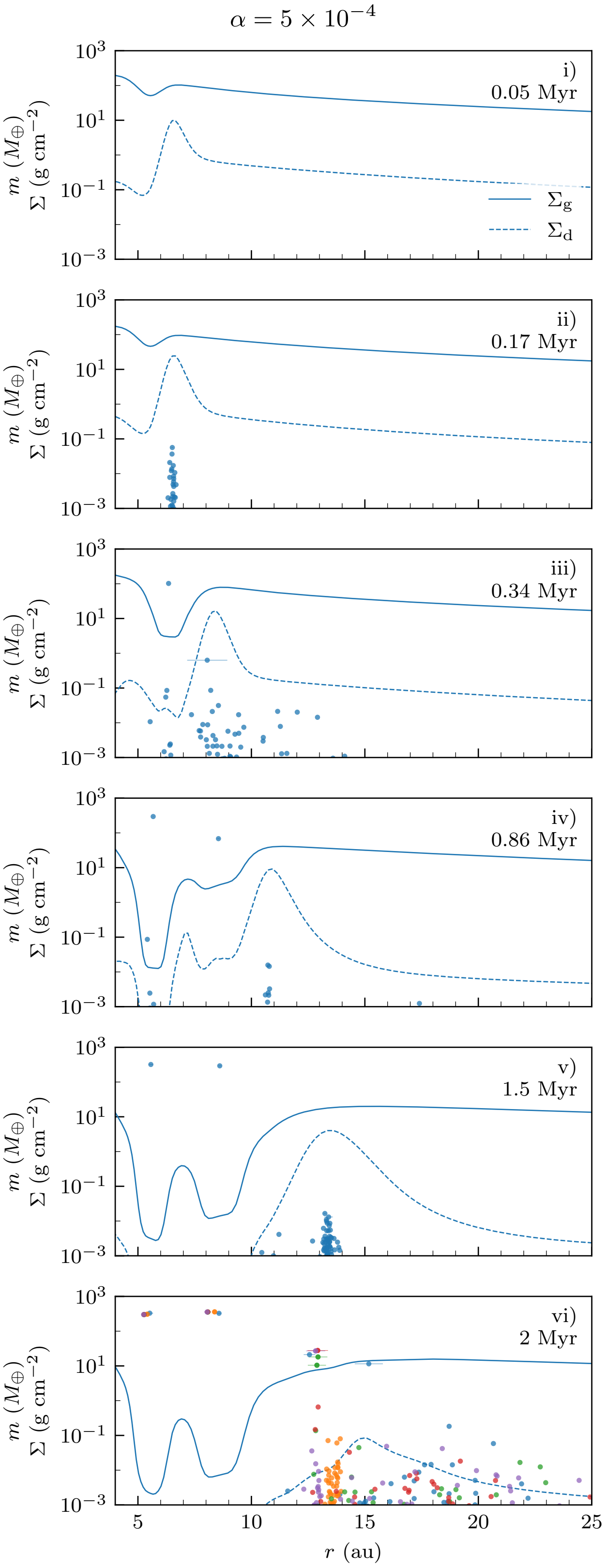

Figure 5.2: Six key timestamps demonstrating sequential planet formation in one of the simulations with $\alpha = 5 \times 10^{-4}$. Each panel shows the radial profiles of the gas surface density Σ_g (solid line), the dust surface density Σ_d (dashed line) and, the mass m and the semimajor axis r of the massive bodies (dot) at the noted time. The final panel also shows the massive bodies from the rest of the simulation set with each colour showing one of the five simulations.

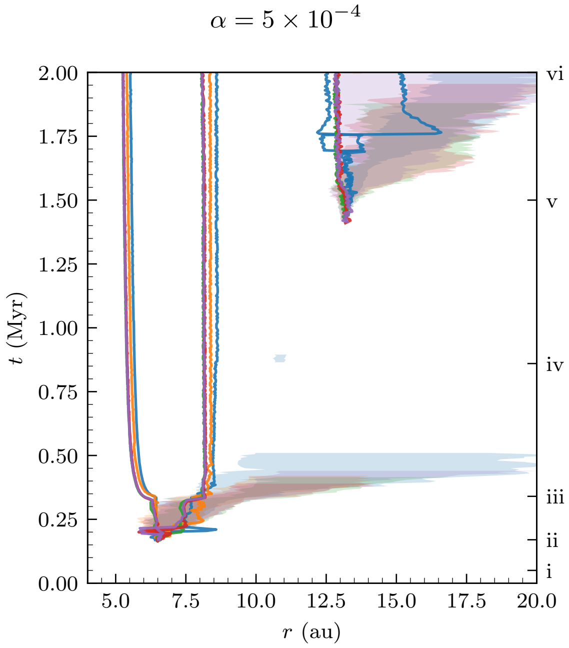

Figure 5.3: Tracks of the massive bodies in the simulation with $\alpha = 5 \times 10^{-4}$. Each colour shows one of the five simulations corresponding to those in the final panel of Fig. 5.2, where the key timestamps are also denoted along the time axis on the right. The solid lines show the semimajor axis of the bodies reached 10 $M_\oplus$ by the end of the simulations. The shaded areas indicate the extents of the lower and upper quartiles of the semimajor axes of all bodies when the total number is above 50.

of the massive bodies, with the error bar indicating the extent of the apoapsis and periapsis for those above 10 $M_\oplus$. The final panel (vi), which presents the end results at 2 Myr, also includes the massive bodies from the rest of the simulation set with each colour showing one of the five simulations.

Figure 5.3 presents the evolution of the semimajor axis of the massive bodies with each colour showing one of the five simulations corresponding to those in the final panel of Fig. 5.2. The solid lines show the ones reaching more than 10 $M_\oplus$ by the end of the simulations. The shaded areas indicate the extents of the lower and upper quartiles of semimajor axes, which is only shown when the total number of bodies is above 50 for a meaningful representation.

At 0.05 Myr (i), the imposed initial substructure has reached the target shape and dust has started to accumulate. At 0.17 Myr (ii), the midplane volumetric dust-to-gas ratio of the disc at about 6.5 au reaches the criteria and planetesimal formation starts. Since these bodies are naturally born in a dust-rich environment, where the dust surface density is more than an order of magnitude higher than the unperturbed case, they can grow rapidly by pebble accretion. The core has also migrated towards the migration trap, which is slightly interior to the peak of the pressure bump, but not further inside as shown by the track in Fig. 5.3.

At 0.34 Myr (iii), the first massive core has entered the runaway gas accretion phase and opened a significant gap in the disc as it becomes a gas giant ($> 100M_\oplus$). The less massive core and planetesimals, which are also formed from the initial pressure bump, are being scattered mainly to wider orbits as shown by the tracks in Fig. 5.3. While most planetesimals have been scattered out of the system, the orbit of the second-most massive planetary core is circularised near 8 to 9 au, and it continues to grow.

At 0.86 Myr (iv), the second core also starts runaway gas accretion but at a much later time relative to the first one. When the second gas giant opens a gap in the disc, the dust near its location follows the sudden change in the gas profile and is pushed away from the forming gas giant to both inner and outer part of the disc. This corresponds to the formation of a small batch of planetesimals near 11 au shown in Fig. 5.3.

At 1.5 Myr (v), the second gas giant also reached approximately one Jupiter mass with another planetary gap fully opened. A new pressure bump is steadily formed at the outer edge of this gap and dust re-accumulates at about 13 to 14 au, which contains a part of the leftover dust from the initial dust trap and the dust drifted from the outer disc. Another generation of planetesimals is formed at this location. A minor instability occurred between two newly formed massive cores at around 1.75 Myr that widens their radial separation.

Due to the late formation of the second generation of planetary cores, which ultimately form a pair of ice giants ($10 - 100M_\oplus$), they remain in the thermal contraction phase of gas accretion at the end of the simulation at 2 Myr (vi). A compact chain of giant planets is produced spanning from 5 to 15 au, with a pair of gas giants formed from the initial pressure bump and a pair of ice giants formed over 1 Myr later from the edge of the planetary gap opened by the outer gas giant. The orbital periods of the inner pair are in near 2:1 commensurability and those of the outer pair are in near 4:3 commensurability.

Across the five random simulations, the final panel of Fig. 5.2 and Fig. 5.3 show very similar results for the gas giant pair formed in the first generation. For the next generation of planet formation, further stochasticity presents. Two (blue and green) simulations produce a pair of ice

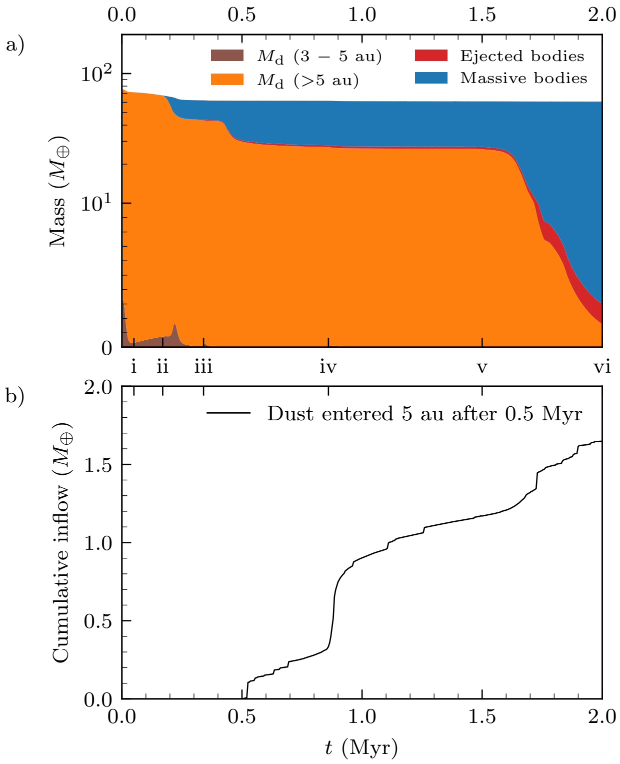

Figure 5.4: Evolution of the solid mass in the simulation with $\alpha = 5 \times 10^{-4}$ that corresponds to the one presented by the colour blue in Fig. 5.2 & 5.3. The six timestamps in Fig. 5.2 are also denoted on the time axis. a) Solid mass budget. The solid mass is divided into four categories: the dust mass M_d inside and outside of 5 au, solids bound in massive bodies and ejected massive bodies. It shows a high planet formation efficiency that the majority of solid mass (85% of the initial dust mass beyond 5 au) are converted into massive bodies. b) Cumulative inflow of dust entered 5 au after 0.5 Myr. A total of about 1.6 $M_\oplus$ of inflow to the inner disc is recorded over the next 1.5 Myr up to the end of the simulation.

giants and another two (red and purple) produce only one ice giant. One simulation (orange) shows no ice giant at 2 Myr but a swarm of still-growing planetesimals and planet embryos.

Dust mass budget

Figure 5.4a shows the solid mass budget throughout the simulation presented by the colour blue in Fig. 5.2 & 5.3. The solid mass is divided into four categories, which are the dust mass M_d inside and outside of 5 au, solids bound in massive bodies, and massive bodies ejected out of the simulation domain. The six timestamps in Fig. 5.2 are also denoted here on the time axis.

After the initial substructure is imposed, the dust mass between 3 au and 5 au (inner disc) decreases sharply due to the inward drift of dust, while the dust supply from 5 au and beyond (outer disc) is stopped at the pressure bump. At 0.05 Myr (i), the pressure bump is saturated with dust and the dust mass in the inner disc increases due to leakage by turbulent diffusion. Planetesimals start to form and grow by pebble accretion at 0.17 Myr (ii), which start converting dust into massive bodies. The conversion is paused when the first core starts to perturb the disc and stops pebble accretion.

Shortly after 0.2 Myr, there is a spike in the dust mass inside of 5 au. This is caused by the gap opening in a dust rich location as the first planetary core reaches the mass of 10 $M_{\oplus}$. Similarly, another spike occurs at about 0.34 Myr (iii) when the first core enters the runaway gas accretion phase but it is much smaller as dust is already depleted around the planet. Pebble accretion resumes for the second core at about 0.4 Myr after its orbit has been circularised, which also causes the change in the dust mass.

Planetesimal formation occurs again at 1.5 Myr (v) and pebble accretion continues to convert the remaining dust to massive bodies. The final (vi) masses of the four categories show that the majority of solids, or 85% of the initial dust mass beyond 5 au, are eventually incorporated into massive bodies.

Figure 5.4b shows the cumulative inflow of dust that crossed 5 au after 0.5 Myr, which is the time when the first gas giant has reached approximately one Jupiter mass. The subsequent dust inflow to the inner Solar System is, on average, 0.5 to 1 $M_{\oplus}\mathrm{Myr}^{-1}$ or, in total, about 1.6 $M_{\oplus}$ including two significant episodic inflows to the inner disc.

The first one occurs shortly at about 0.86 Myr (iv) as the second planetary core enters the runaway gas accretion phase and opens a gap in the disc. The dust near its location follows the sudden change in the gas disc and is pushed by the forming gas giant to both inner and outer part of the disc, which is also shown in the profiles of the surface densities (Fig. 5.2 iv). The second one corresponds to a small instability occurs between the two newly formed massive cores at around 1.75 Myr and perturbs the disc (Fig. 5.3).

5.3.2 The case of $\alpha = 3 \times 10^{-4}$

Figure 5.5 presents the tracks of the massive bodies for the set of simulations with $\alpha = 3 \times 10^{-4}$ in the manner of Fig. 5.3. Figure 5.6 presents the end results to the final panel of Fig. 5.2. The radial profiles of the surface densities are also shown for the whole set of simulations. Compared to the case of $\alpha = 5 \times 10^{-4}$ in Sect. 5.3.1, a larger variation across the simulations is shown. For all simulations, planetesimal formation occurs at about 0.25 Myr, which is about 0.1 Myr later than the case of $\alpha = 5 \times 10^{-4}$.

In the simulations denoted by the colour red in Fig. 5.5, a massive core is scattered through the migration trap by another core and is lost to the inner simulation boundary. Later at about 0.6 Myr, the next generation of planetesimals are formed resulting in two massive cores. Similarly, in the simulations denoted by the colour green, only one core is formed from the initial pressure bump and two is formed from the subsequent generation.

In the simulations denoted by the colour blue and purple, two cores are formed from the initial bump. The second generation of planet formation occurs at about 1.75 Myr for the former one, while only a concentrated dust ring presents at the outer edge of the planetary gap for the latter one at the end of the simulation. And, the simulation denoted by the colour orange forms three gas giants from the initial pressure bump and no further planet formation occurs before the simulation ends.

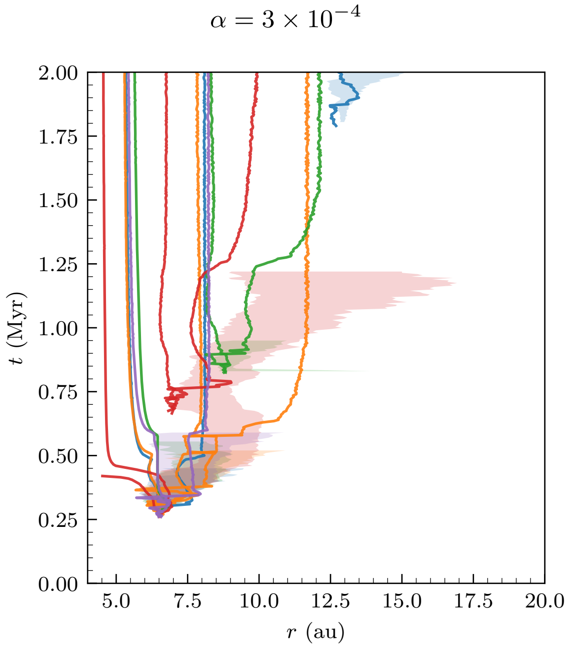

Figure 5.5: Tracks of the massive bodies in the simulations with $\alpha = 3 \times 10^{-4}$ presented in the same manner as in Fig. 5.3.

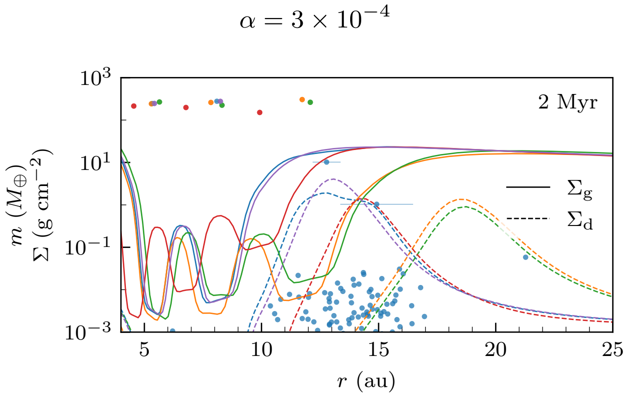

Figure 5.6: Results of the set of five simulations with $\alpha = 3 \times 10^{-4}$. Similar to the final panel of Fig. 5.2 except the surface density profiles are shown for all simulations.

Figure 5.6 summarises the final architecture of the planets where three out of the five simulations form three gas giants and the remaining two (blue and purple) form two. Also, a significant dust ring remains respectively for all simulations external to their outermost gas giant.

5.4 Discussions

5.4.1 Sequential planet formation

The results presented in Sect. 5.3 demonstrate a complete scenario of sequential planet formation. In the case of $\alpha = 5 \times 10^{-4}$ (Sect. 5.3.1), two gas giants are formed from the initial disc substructure. As the outer gas giant has reached its final mass and a steady planetary gap is opened, dust re-accumulates at a later time near the new pressure bump triggering the next generation of planet formation. The case of $\alpha = 3 \times 10^{-4}$ shows similar trend despite of the greater degree of stochasticity.

Comparing the results with the 'inside-out' planet formation scenario by Chatterjee & Tan (2013) for Kepler systems, we note that gas giant that has reached its final mass is more likely to trigger the next generation of planet formation. For low-mass planets that cannot open a significant gap in the disc ($\lesssim 100 M_\oplus$), dust leakage from the pressure bump at the outer edge of the gap is significant and requires a large supply from the outer disc to reach the conditions for planetesimal formation. Even if planetesimals may form, they are under greater gravitational influence of the planets as the width of the gap scales with $m^{1/2}$ (Kanagawa et al. 2016; Duffell 2020) while the Hill radius scales with $m^{1/3}$. In this case, the perturbation from the planet is more likely to prevent the growth of the planetesimals as pebble accretion, particularly when the planet continues to grow, is sensitive to the relative velocity as noted in Lau et al. (2022). These planetesimals will likely be scattered out of the system as well, if the planet enters the runaway gas accretion phase to become a gas giant. Therefore, the outer edge of the planetary gap opened by a steady gas giant is a much more favourable environment for the next generation of planet formation.

Architecture of the resulting systems

In the case of $\alpha = 5 \times 10^{-4}$ (Sect. 5.3.1), the delay in the formation of the second generation of planets directly shortens the time available for their growth. Therefore, they remain at about $10 M_\oplus$ by the end of the simulations. Although disc dissipation is not included in the current model, the sequential planet formation scenario provides the delay in formation time of the ice giants required by the models explaining their masses (e.g. Lee et al. 2014; Ogihara et al. 2020; Raorane et al. 2024). At the end of the simulations, the second generation planetesimals and embryos formed still remain in the system as the ice giants are not able to scatter them. This results in a system with diversity that consists of gas giants, ice giant(s) and small massive bodies.

Since the radial separation of the two generations of planets is determined by the gap width, the resulting system is compact with the four giants planets from 5 to 15 au. The gas giants formed from the initial substructure are also commonly in the 2:1 mean-motion resonance. While a further test with a larger sample size is required, this may justify the compact chain of giant planets adopted in the initial conditions of the Nice model (e.g. Tsiganis et al. 2005; Morbidelli et al. 2005) and the early instability model (e.g. Clement & Kaib 2017; Deienno et al. 2018) from the formation point of view.

Due to the computational cost, only two values of α are tested in this work where a larger degree of stochasticity is presented for the case of $\alpha = 3 \times 10^{-4}$ (Sect. 5.3.2). Other than α, which determines the evolution timescale of the disc, the resulting planetary system should also be sensitive to the initial disc mass $M_{\rm disc}$, the characteristic radius $r_{\rm c}$ and the location of the initial disc substructure. Upon the availability of TriPoD (Pfeil et al. submitted), which is a simplified three-parameter dust coagulation model, a more extensive parameter study shall become computationally feasible to study the diversity of planetary systems.

Dust mass budget

The resulting solid mass budget (Fig. 5.4a) shows a high planet formation efficiency for the presented simulation with $\alpha = 5 \times 10^{-4}$. The common gap opened by the two gas giants is very effective in preventing dust from drifting through. As a result, the remaining dust is retained in the disc for a prolonged period of time and preserved solids for the subsequent planet formation.

After the formation of the first gas giant, the quasi-steady inflow and the episodic inflows result in a total of about 1.6 $M_\oplus$ of outer disc dust flowing into the inner disc over a time period of 1.5 Myr (Fig. 5.4b). The leftover planetesimals formed from the initial disc substructure are also generally scattered outward by the rapid formation of the first gas giant (Fig. 5.3). This indicates the chemical division caused by the first gas giant is robust. While further tests with the correct masses of the giant planets and their time of formation are required, this formation scenario may provide the required rapid formation of Jupiter's core to prevent significant exchange of the non-carbonaceous and carbonaceous reservoirs in the early Solar System (Kruijer et al. 2017).

Stammler et al. (2023) studied the efficiency of dust trapping by planetary gaps corresponding to different planetary masses and values of α. Their results show a dust leakage rate of about $1 M_\oplus \mathrm{Myr}^{-1}$ for a gap created by a Saturn-mass planet with $\alpha = 10^{-4}$. This is broadly consistent with the presented leakage rate of about $0.5 M_\oplus \mathrm{Myr}^{-1}$ with the episodic inflows due to the dynamical instabilities excluded, since the planetary gap prescription used here is about 30% deeper than the one given by Kanagawa et al. (2016) (see Fig. 8 of Duffell (2020)) and the planet is about three times more massive in our case.

The small inflow of dust from the outer disc is likely to be preferentially accreted by a proto-Earth and proto-Venus as pebble accretion is more efficient for bodies with higher mass and dynamically colder orbits. This may explain Earth's chemical abundances relative to Mars and Vesta (Kleine et al. 2023) without causing a significant growth to form super-Earth. This result also suggests against the scenario of significant growth by pebble accretion in the inner Solar System (e.g. Johansen et al. 2021).

5.4.2 Comparison with the Solar System

We note that the results of $\alpha = 5\times10^{-4}$ (Sect. 5.3.1) show a pair of Jupiter-mass giants, instead of one Jupiter- and one Saturn-mass giants. Although the second gas giant entered the runway gas accretion about 1 Myr later than the first one, there is no significant mass difference in the end. This is likely due to the absence of disc dissipation, which results in a high gas surface density throughout the simulation. Further developments of the model to include photoevaporation are required to provide a complete scenario of the formation of the early outer Solar System and planet formation in general. We anticipate that the remaining dust in the protoplanetary disc will form a belt of planetesimals resembling the scenario proposed by Carrera et al. (2017). In this case, these planetesimals will remain dynamically cold while growth by pebble accretion is prohibited due to the depletion of gas and dust. After disc dissipation, the N-body part (SyMBAp) can continue to model the long-term evolution of the system and show if a Nice model-like instability can occur among the giant planets.

The formation of the gas giants in the results is likely too quick compared to the meteoritic record (Kruijer et al. 2017, 2020). We note that the composition and the opacity of the envelope of gas giant, which are critical to the gas accretion rate, are still an active field of research (e.g. Szulágyi et al. 2016; Lambrechts et al. 2019; Schulik et al. 2019; Ormel et al. 2021). And, different gas accretion prescriptions are adopted among recent planet formation models (e.g. Liu et al. 2019; Bitsch et al. 2019; Matsumura et al. 2021; Chambers 2021; Lau et al. 2024b). Further investigations on the different recipes and their consequences are required to match the formation history of the Solar System's giant planets.

While the source of the initial disc substructure is not investigated in this work, the water ice line in the early Solar System has been proposed as a key feature in reproducing the Solar System by multiple works (e.g. Morbidelli et al. 2016, 2022; Brasser & Mojzsis 2020; Charnoz et al. 2021; Chambers 2023). Further investigations are required to determine the criteria at the water ice line in the early Solar System to trigger planet formation, particularly, the change in the surface density required.

5.4.3 Other recent works

Predictions of planet formation at pressure bumps

Xu & Wang (2024) made theoretical predictions on the architecture of the planetary systems assuming efficient planet formation at pressure bumps. They concluded three main pathways: slow core formation, fast core formation but slow gas accretion and, fast core formation and gas accretion.

While Lau et al. (2022) and Jiang & Ormel (2023) show that the high dust concentration at a pressure bump will likely favour rapid growth of core, the slow core formation can be possible if the planetesimals formed are dynamically heated to an extent that pebble accretion is halted but they still remain close to there birthplace.

The case of fast core formation but slow gas accretion is suggested to form a chain of super-Earths or potentially Saturn-mass planets over a prolonged period of time. This case is similar to the scenario proposed by Chatterjee & Tan (2013). As discussed in Sect. 5.4.1, the planetary gap formed by super-Earths may not be able to trap a significant amount of dust and trigger planetesimal formation. And, even if planetesimals could form, they are likely much closer to the core and cannot grow efficiently by pebble accretion.

The case of fast core formation and fast gas accretion is suggested to form a chain of gas giants. This prediction is the closest to the results shown in Sect. 5.3 while two to three gas giants can form from the pressure bump in the presented work. We note that the number of cores that can form from each pressure bump likely depends on the amplitude and the width of the dust trap, while this has not been tested in the presented work. This requires an extensive parameter study and more random simulations per set of parameters.

Although dust trap favours planetesimal formation, we emphasise that insitu planet formation at pressure bumps is unlikely a general solution to the diversity of exoplanetary systems. In particular, for the observed compact planet chains in resonance, a more probable formation scenario is that the cores are formed at a temporary pressure bump which migrate subsequently through the disc. Multiple works have studied the scenario that the inner most planet can be trapped at the disc edge (e.g. Terquem & Papaloizou 2007; Cossou et al. 2013; Brasser et al. 2018; Huang & Ormel 2023) and the subsequent inward-migrating planets can form a resonant chain through convergent inward migration (e.g. Tamayo et al. 2017; Delisle 2017; MacDonald & Dawson 2018; Wong & Lee 2024).

Sandwiched planet formation

With gas and dust hydrodynamics simulations, Pritchard et al. (2024) proposed the ‘sandwiched planet formation’ scenario where planet formation can occur with the dust trapped between two massive planets that each creates a pressure maximum. The authors already noted that formation of the planets and dust fragmentation are not modelled, which may have critical effect to the dust concentration between the planets. Furthermore, from the results presented above (Sect. 5.3), we also note that if planetesimals could form between the planets, they are likely under a great gravitational influence from the massive planets. This will prevent them from growing efficiently by accreting pebbles, or, more likely, scatter them. Nonetheless, their work confirms dust rings can be created by massive planets with hydrodynamics simulations and these are preferred locations of planet formation.

5.4.4 Caveats

Initial disc substructure

In this work, we studied the consequence of a substructure in the disc that can trigger planetesimal formation, with the location motivated by that of Jupiter. Although multiple non-planetary mechanisms are proposed in the field as discussed in Sect. 5.1, the parameter space, including the location, amplitude, width and lifetime, is not explored in this work and requires future investigations. For instance, from some test runs, we note that the amplitude of the substructure needs to be large enough to trap dust effectively and trigger planetesimal formation, although non-axisymmetric features that may aid dust concentration such as vortices (e.g. Barge & Sommeria 1995; Tanga et al. 1996) are not considered. Sequential planet formation also cannot occur if the dust mass remaining is not enough to trigger the next generation of planet formation. We emphasise that the criteria to form planetesimals are not trivial to satisfy in typical disc conditions. This work only focuses on a case where planetesimal formation is possible. However, by combining the unknowns in the shape and location of the initial disc substructure with different disc parameters, we expect the model can produce a variety of planetary systems through a parameter study, where sequential planet formation may not always occur.

Planet migration and gap opening

At the end of Sect. 5.2.4, we note that planetary gap opening and planet migration are treated by independent prescriptions while they are both the results of planet-disc interactions and are physically coupled. Also, multiple works (e.g. Lin & Papaloizou 1986; Armitage & Bonnell 2002; D'Angelo & Lubow 2010) have studied both effects consistently and provided formulae for the torque density profile exerted by a planet on the disc. However, upon applying the formula given by D'Angelo & Lubow (2010) in our 1-D model, we note that the gap opened by a Jupiter-mass planet is much narrower than that described in Duffell (2020), which is also given by Eq. (5.27). Since this gap profile is tested against a set of 2-D hydrodynamical simulations in a general parameter space and is consistent with other works (e.g. Kanagawa et al. 2015b), we have opted to prescribe the gap profile and planet migration separately. We also note that a fixed temperature profile is adopted in this work, which implies that the effect of shock heating (e.g. Zhu et al. 2015; Rafikov 2016) is neglected while its effect is likely more significant in the outer disc where less irradiation from the star is received. Nonetheless, upon the availability of a general torque formula applicable to a 1-D model, this part of the model shall be modified for consistency, especially in the case of having multiple gap-opening planets in the disc.

5.5 Conclusions

This work demonstrates a scenario of sequential giant planet formation that is triggered by an initial disc substructure. We further extended the model in Lau et al. (2022) by including the effects of planetary gas accretion and gap opening. We employed DustPy to model a protoplanetary disc initially with micron-sized dust, and SyMBAp was employed to model the evolution of the planetesimals upon formation.

Consistent with the previous results, planetary cores are formed rapidly from the initial disc substructure, which can then be retained at the migration trap and start gas accretion. The results show multiple (up to three) cores can form and grow into giant planets in each generation. As the first generation of gas giants has formed and opened a steady gap, the new pressure bump at the outer edge of the planetary gap becomes the next location of planet formation.

In the case of the higher value of $\alpha = 5 \times 10^{-4}$, the second generation of planet formation occurs about 1 Myr after the first one, and only ice giants were formed instead of gas giants. This case also shows a high planet formation efficiency where more than 85% of the dust beyond

5 au is converted into massive bodies. As the first generation of gas giants effectively prevent dust from flowing through to reach the inner disc, the retained dust is then available for the next generation of planet formation. In the case of a lower value of $\alpha = 3 \times 10^{-4}$, a larger degree of stochasticity was shown, while the general scenario of sequential giant planet formation remains. In both cases, a compact chain of giant planets are formed at the end of the simulations. While the simulations were stopped at 2 Myr, a natural continuation to the model would be to include the effect of photoevaporation to physically dissipate the disc and stop gas accretion.

Although the formation mechanisms of disc substructure are beyond the scope of this work, further investigations are required to study the possible shape and location produced by physical processes. It is unlikely that any disc substructure can trivially provide the conditions required for planetesimal or planet formation. Also, the parameter space and the number of random simulations in this work are limited by the computational costs. Further code optimisation is required to study the statistical effects and to model the diversity of planetary systems. And, planetary gas accretion is still an active field of research. Further investigations specifically on gas accretion are required to model the formation time of the Solar System's giant planets.

Acknowledgments

We thank T. Kleine, C. Ormel, R. Teague and A. Vazan for the insightful discussions. We acknowledge funding from the European Research Council (ERC) under the European Union's Horizon 2020 research and innovation programme under grant agreement No 714769, under the European Union's Horizon Europe Research and Innovation Programme 101124282 (EARLY-BIRD) and funding by the Deutsche Forschungsgemeinschaft (DFG, German Research Foundation) under grant 325594231 and Germany's Excellence Strategy – EXC-2094 – 390783311. JD was funded by the European Union under the European Union's Horizon Europe Research & Innovation Programme 101040037 (PLANETOIDS). Views and opinions expressed are however those of the authors only and do not necessarily reflect those of the European Union or the European Research Council. Neither the European Union nor the granting authority can be held responsible for them.

Chapter 6

Planetesimal formation during disc dissipation through internal photoevaporation

6.1 Introduction

As discussed in Chapter 2.1, disc dissipation due to photoevaporation rapidly removes the disc and sets the end of the disc lifetime, which also terminates the gas accretion of growing planets. And, in Chapter 5, the late formation of the Solar System's ice giants needs to complete at a specific time window before disc dispersal. If they form too early and continue to accrete gas, runaway gas accretion occurs and gas giants are formed instead. On the other hand, if the cores are not completed before disc dispersal, a rocky super-Earth is formed instead.

Furthermore, the cold classical Kuiper belt objects are likely the direct product of planetesimal formation as discussed in Chapter 2.3. And, Carrera et al. (2017) showed that the enhanced dust-to-gas ratio required by the streaming instability can be achieved at the outer edge of the cavity opened by photoevaporation. While further modelling is required, applying this formation scenario to the cold classicals can explain why they did not grow significantly by pebble accretion in a dust-rich environment.

The planet formation models in the previous chapters did not consider disc dissipation and cannot physically terminate the growth of the ice giants. In this ongoing work, the X-ray photoevaporation by the central star is considered as it has been suggested to dominate the mass loss rate of discs (Ercolano et al. 2009). The prescription for the mass loss rate of the gas by Picogna et al. (2019) and the prescription for dust mass loss through entrainment by Gárate et al. (2021) are adopted. These components are added to the planet formation by Lau et al. (2024a) as presented previously in Chapter 5 while some modifications are made to gas accretion. The new model is described in the next section and the preliminary results are presented in Sect. 6.3.

6.2 Method

The method in this work is developed upon the model in Lau et al. (2022) and Lau et al. (2024a) (Chapter 4 & 5). In this model, the dust and gas evolution code DustPy v1.0.5 (Stammler & Birnstiel 2022), and the symplectic N-body integrator SyMBAp v1.6 (Lau & Lee 2023), a parallelised version of the Symplectic Massive Body Algorithm (SyMBA; Duncan et al. 1998), are coupled. In this work, the gas accretion and gap opening components are modified and a new component to include the effect of internal photoevaporation is added. The changes to the method described previously in Chapter 5.2 are detailed below.

6.2.1 Gas accretion

As noted in Sect. 5.4.2, planetary gas accretion is still an active field of research and the the uncertainty lies in the envelope opacity. To better understand the consequence, we have opted to treat the envelope opacity as a free parameter that can also encapsulate the general efficiency of accretion. Furthermore, the models by Bitsch et al. (2015b) and Chambers (2021) have neglected the limit on accretion imposed by the cooling of the envelope in the runaway accretion phase. This is likely the cause of the rapid growth in this phase as noted in Sect. 5.4.2. Physically, the gas accretion should be limited by both the cooling of the envelope and the supply of gas in either phase.

In the existing prescriptions, the cooling-limited rate of gas accretion in the thermal contraction phase adopted by Bitsch et al. (2015b) based on Piso & Youdin (2014) with the modification for pebble accretion by Chambers (2021) is still valid. While in the runaway gas accretion phase, the Kelvin-Helmholtz timescale imposes a limit on the collapse rate of the envelope as shown by Ikoma et al. (2000). On the gas supply, the prescription by Tanigawa & Watanabe (2002) based on the gas flow to the planet applies. This is further restricted by the overall disc accretion rate as Lubow & D'Angelo (2006) suggested that the gas accretion rate is limited to about 80% of which. To summarize, the cooling-limited accretion rate in the thermal contraction phase is

$$\begin{aligned} \dot{m}_{\mathrm{cool,cont}} = \max\Bigg[0, 4.375 \times 10^{-9} \left(\frac{\kappa}{\mathrm{cm^2\ g^{-1}}}\right)^{-1} \left(\frac{\rho_{\mathrm{c}}}{5.5\ \mathrm{g\ cm^{-3}}}\right)^{-1/6} \times \\ \left(\frac{m_{\mathrm{c}}}{M_{\oplus}}\right)^{11/3} \left(\frac{m_{\mathrm{env}}}{M_{\oplus}}\right)^{-1} \left(\frac{T}{81\mathrm{K}}\right)^{-1/2} M_{\oplus}\mathrm{yr}^{-1} - 15\dot{m}_{\mathrm{pa}}\Bigg] \end{aligned} \quad (6.1)$$

with the envelope opacity κ, the density of the core $\rho_{\mathrm{c}} = 5.5\ \mathrm{g\ cm^{-3}}$, the mass of the core m_{c} the mass of the envelope m_{env}, the local disc temperature T and the pebble accretion rate $\dot{m}_{\mathrm{pa}}$. And, that in the runaway phase is

$$\dot{m}_{\mathrm{cool,run}} = \frac{m}{\tau_{\mathrm{KH}}} \quad (6.2)$$

with the the Kelvin-Helmholtz contraction timescale

$$\tau_{\mathrm{KH}} = 10^9 \left(\frac{m}{M_{\oplus}}\right)^{-3} \left(\frac{\kappa}{1\ \mathrm{cm^2\ g^{-1}}}\right) \mathrm{yr}, \quad (6.3)$$

where the planet mass is m and the indices follow the adoption of Ida & Lin (2004). And, the gas supply limits include the flow limit

$$\dot{m}_{\rm flow} = 0.29\Sigma_{\rm g} r^2 \Omega_{\rm K} \left(\frac{m}{M_\odot}\right)^{4/3} \hat{h}_{\rm g}^{-2} \tag{6.4}$$

with the local disc surface density $\Sigma_{\rm g}$, the Keplerian orbital frequency $\Omega_{\rm K}$ and the local reduced scale height $\hat{h}_{\rm g}$, and the disc accretion limit

$$\dot{m}_{\rm acc} = 0.8\dot{M}_{\rm disc} \tag{6.5}$$

with the local disc accretion rate $\dot{M}_{\rm disc}$. The actual gas accretion rate of a planet is then, in the thermal contraction rate for $m_{{\rm en}v} < m_{\rm c}$,

$$\dot{m}_{\rm cont} = \min\left(\dot{m}_{\rm cool,cont}, \dot{m}_{\rm flow}, \dot{m}_{\rm acc}\right) \tag{6.6}$$

and, in the runway gas accretion phase for $m_{\rm c} \geq m_{{\rm en}v}$,

$$\dot{m}_{\rm run} = \min\left(\dot{m}_{\rm run,cont}, \dot{m}_{\rm flow}, \dot{m}_{\rm acc}\right) \tag{6.7}$$

We note that the asymptotic mass proposed by Dobbs-Dixon et al. (2007) based on termination of growth due to gap opening does not require explicit implementation in our model. This effect is already captured when a gap is opened in this disc that limits the gas flow to the planet.

6.2.2 Gap opening

Previously in Lau et al. (2022) and Lau et al. (2024a) (Chapter 4 & 5), the initial gap and the planetary gap are imposed to the gas by modifying the viscosity α-parameter. In this work, the disc dissipation is modelled, where the gas surface density shall attain a low value and this implementation shall cause an unrealistically high gas velocity with a deep planetary gap. Therefore, we imposed the initial gap and the planetary gap through the radial gas flux due to a torque profile instead. From Lin & Papaloizou (1986) and Trilling et al. (1998), the advection-diffusion equation under the influence of an axis-symmetrical torque deposition is

$$\frac{\partial \Sigma_{\rm g}}{\partial t} = \frac{3}{r}\frac{\partial}{\partial r}\left[r^{1/2}\frac{\partial}{\partial r}(\nu\Sigma_{\rm g} r^{1/2}) - \frac{2\Lambda\Sigma_{\rm g}}{3\Omega_{\rm K}}\right] \tag{6.8}$$

where ν is the α-viscosity and Λ is the angular momentum injection rate. As noted in Lau et al. (2024a) (Chapter 5), there are other works (e.g. Lin & Papaloizou 1986; Armitage & Bonnell 2002; D'Angelo & Lubow 2010) provided formulae for the torque density profile exerted by a planet on the disc, however, applying the formula given by D'Angelo & Lubow (2010) did not produced a gap profile in the one-dimensional model.

Therefore, in this work, an equivalent profile for Λ is derived by assuming a steady state with the target surface density profile and the accretion rate is not changed by the imposed profile. Equation (6.8) can be rewritten as

$$\frac{\partial \Sigma_{\rm g}}{\partial t} = \frac{3}{r}\frac{\partial}{\partial r}\left[r\Sigma_{\rm g}(v_\nu + v_\Lambda)\right] \tag{6.9}$$

with the accretion velocity

$$v_\nu = -\frac{3\nu}{r}\frac{\partial \log}{\partial \log r}\left(\Sigma_\mathrm{g} r^{1/2}\nu\right) \tag{6.10}$$

and the additional velocity due to the torque injection

$$v_\Lambda = \frac{2\Lambda}{\Omega_\mathrm{K} r}. \tag{6.11}$$

The condition that the disc accretion is not impeded by the planetary gap can be expressed as

$$\Sigma_\mathrm{g,eq}(v_{\nu,\mathrm{eq}} + v_\Lambda) = \Sigma_\mathrm{g,0} v_{\nu,0}, \tag{6.12}$$

where $\Sigma_\mathrm{g,eq}$ and $v_{\nu,\mathrm{eq}}$ are the gas surface density and accretion velocity at the steady state with the imposed gap, $\Sigma_\mathrm{g,0}$ is the unperturbed gas surface density and $v_{\nu,0}$ is the unperturbed accretion velocity. With the assumption of a constant disc accretion rate, $\partial(\Sigma_\mathrm{g,0}\nu)/\partial r = 0$. And, with the target surface density profile defined by

$$f(r) \equiv \frac{\Sigma_\mathrm{g,eq}}{\Sigma_\mathrm{g,0}}, \tag{6.13}$$

from Eq. (6.10),

$$\begin{align} v_{\nu,\mathrm{eq}} &= -\frac{3\nu}{r}\frac{\partial \log}{\partial \log r}\left(f\Sigma_\mathrm{g,0} r^{1/2}\nu\right) \tag{6.14}\\ &= -\frac{3\nu}{r}\left(\frac{\partial \log f}{\partial \log r} + \frac{1}{2}\right), \tag{6.15}\end{align}$$

and,

$$v_{\nu,0} = -\frac{3\nu}{2r}. \tag{6.16}$$

Then, from the steady state accretion condition given by Eq. (6.12), the additional velocity can be evaluated by

$$\begin{align} v_\Lambda =& \frac{v_{\nu,0}}{f(r)} - v_{\nu,\mathrm{eq}} \tag{6.17}\\ =& -\frac{3\nu}{r}\left(\frac{1}{2f} - \frac{\partial \log f}{\partial \log r} - \frac{1}{2}\right). \tag{6.18}\end{align}$$

To implement this in DustPy, an external source is applied and calculated with v_Λ. For the profile f, we applied the same initial gap profile and the planetary gap profile by Duffell (2020) as described in Chapter 5.

6.2.3 Internal photoevaporation

Mass loss in gas

Picogna et al. (2019) employed the three-dimensional gas photoionization and dust radiative transfer code MOCASSIN (Ercolano et al. 2003, 2005, 2008b) to study the mass loss of a disc that is under an X-ray and extreme ultra-violet spectrum of irradiation (Ercolano et al. 2008a) by the central star. Both the case of a primordial disc and the case of a transition disc with a large cavity are studied. In the former case, the total mass loss rate $-\dot{M}_{\mathrm{g,pr}}$ is given by

$$\log\left(-\frac{\dot{M}_{\mathrm{g,pr}}}{M_{\odot}\ \mathrm{yr}^{-1}}\right) = A_{\mathrm{L}} \exp\left\{\frac{[\ln(\log L_{\mathrm{X}}) - B_{\mathrm{L}}]^2}{C_{\mathrm{L}}}\right\} + D_{\mathrm{L}} \tag{6.19}$$

with the X-ray luminosity of the star L_{X}. The fitting parameters are $A_{\mathrm{L}} = -2.7326$, $B_{\mathrm{L}} = 3.3307$, $C_{\mathrm{L}} = -2.9868 \times 10^{-3}$ and $D_{\mathrm{L}} = -7.2580$. The radial profile of the loss rate is

$$-\dot{\Sigma}_{\mathrm{g,pr}} = \frac{\dot{M}_{\mathrm{g,pr}}}{2\pi r_{\mathrm{au}}^2} M_{\odot}\mathrm{au}^{-2}\mathrm{yr}^{-1} \times \sum_{k=1}^{6} k a_k \log^{k-1} r_{\mathrm{au}}, \tag{6.20}$$

where the radial mass loss factor is

$$\dot{M}_{\mathrm{r}} = \dot{M}_{\mathrm{g,pr}} 10^n \tag{6.21}$$

with the index

$$n = \sum_{k=0}^{6} a_k \log^k r_{\mathrm{au}} \tag{6.22}$$

and $r_{\mathrm{au}} \equiv r/\mathrm{au}$. The fitting parameters are $a_0 = -2.8562$, $a_1 = 5.7248$, $a_2 = -11.4721$, $a_3 = 16.3587$, $a_4 = -12.1214$, $a_5 = 4.3130$ and $a_6 = -0.5885$. In the latter case of a transition disc, the inner edge of the outer disc is directly illuminated by the central star. The radial profile of the loss rate is then

$$-\dot{\Sigma}_{\mathrm{g,tr}} = \frac{b_0 b_1^x x^{b_2-1}(x \ln b_1 + b_2)}{r_{\mathrm{au}}} M_{\odot}\mathrm{au}^{-2}\mathrm{yr}^{-1} \tag{6.23}$$

with the fitting parameters $b_0 = 0.11843$, $b_1 = 0.99695$ and $b_2 = 0.48835$. And, the distance from the outer edge of the cavity is

$$x \equiv \frac{r - r_{\mathrm{cavity}}}{\mathrm{au}}. \tag{6.24}$$

We followed the implementation by Gárate et al. (2021) that the cavity is considered open when $r_{\mathrm{cavity}} \geq 7.5\mathrm{au}$.

Mass loss in dust

Based on the results of the two-dimensional hydrodynamical gas model by Franz et al. (2020), Gárate et al. (2021) implemented the criteria that only small dust particles of at most 10 μm and is at least three scale height H_{g} above the midplane are entrained in the photoevaporative wind.

For the implementation in DustPy, the mass loss rate for the dust species i that has size $a < 10\,\mu$m is

$$-\dot{\Sigma}_{\mathrm{d},i} = \epsilon_{\mathrm{ent,i}}\dot{\Sigma}_{\mathrm{g}} \tag{6.25}$$

with the gas mass loss rate $\dot{\Sigma}_{\mathrm{g}}$. And, the dust-to-gas ratio of the dust species above $3H_{\mathrm{g}}$ is

$$\epsilon_{\mathrm{ent},i} = \frac{\int_{3H_{\mathrm{g}}}^{\infty} \rho_{\mathrm{d},i}(z)\,\mathrm{d}z}{\int_{3H_{\mathrm{g}}}^{\infty} \rho_{\mathrm{g}}(z)\,\mathrm{d}z}. \tag{6.26}$$

The dust density of the species i is

$$\rho_{\mathrm{d},i}(z) = \rho_{\mathrm{d},i}(z = 0)\exp\left(-\frac{z^2}{2H_{\mathrm{d},i}^2}\right) \tag{6.27}$$

with the dust scale height $H_{\mathrm{d},i}$ and the gas density is

$$\rho_{\mathrm{g}}(z) = \rho_{\mathrm{g}}(z = 0)\exp\left(-\frac{z^2}{2H_{\mathrm{g}}^2}\right). \tag{6.28}$$

The midplane densities and the scale heights are evaluated by DustPy for each radial grid cell.

Parameters

As a test for to the new model, the next section presents the preliminary results of a one-Myr simulation, where the Solar-mass star has a relatively strong X-ray luminosity $L_{\mathrm{X}} = 10^{30}$ erg s^{-1}. The disc is initially 0.025 $M_{\odot}$ in mass with the characteristic radius R_{c} of 50 au and the α viscosity parameter of 5×10^{-4}. The initial dust mass is set by the Solar metallicity and the fragmentation velocity is 5 m s^{-1}. The initial Gaussian disc gap is centred at 5.5 au with the amplitude of 1.5 and the width of 0.5 au.

For planetesimal formation, the small-scale diffusion parameter δ is set at 5×10^{-6} and the formation efficiency ζ is set at 10^{-3}. And, only the dust with a Stokes number greater than 10^{-3} can participate in planetesimal formation. For gas accretion, a constant envelope opacity κ of 0.05 cm^2 g^{-1} is adopted.

6.3 Preliminary results

Figure 6.1 presents the time sequence at 0.1 Myr intervals of the simulation as described in Sect. 6.2.3. In each panel, the eccentricity e and the semimajor axis r of the massive particles, and, the radial profile of the dust and gas densities are shown at the denoted times. Planetesimal of less than an Earth mass is denoted with a grey dot. And, planet above an Earth mass is denoted by a dark grey circle with the radius proportional to the cube root of its mass.

After 0.1 Myr since the start of the simulation, the initial gap has started to trap dust drifting from the outer disc while the criterion for planetesimal formation is not reached yet. At 0.2

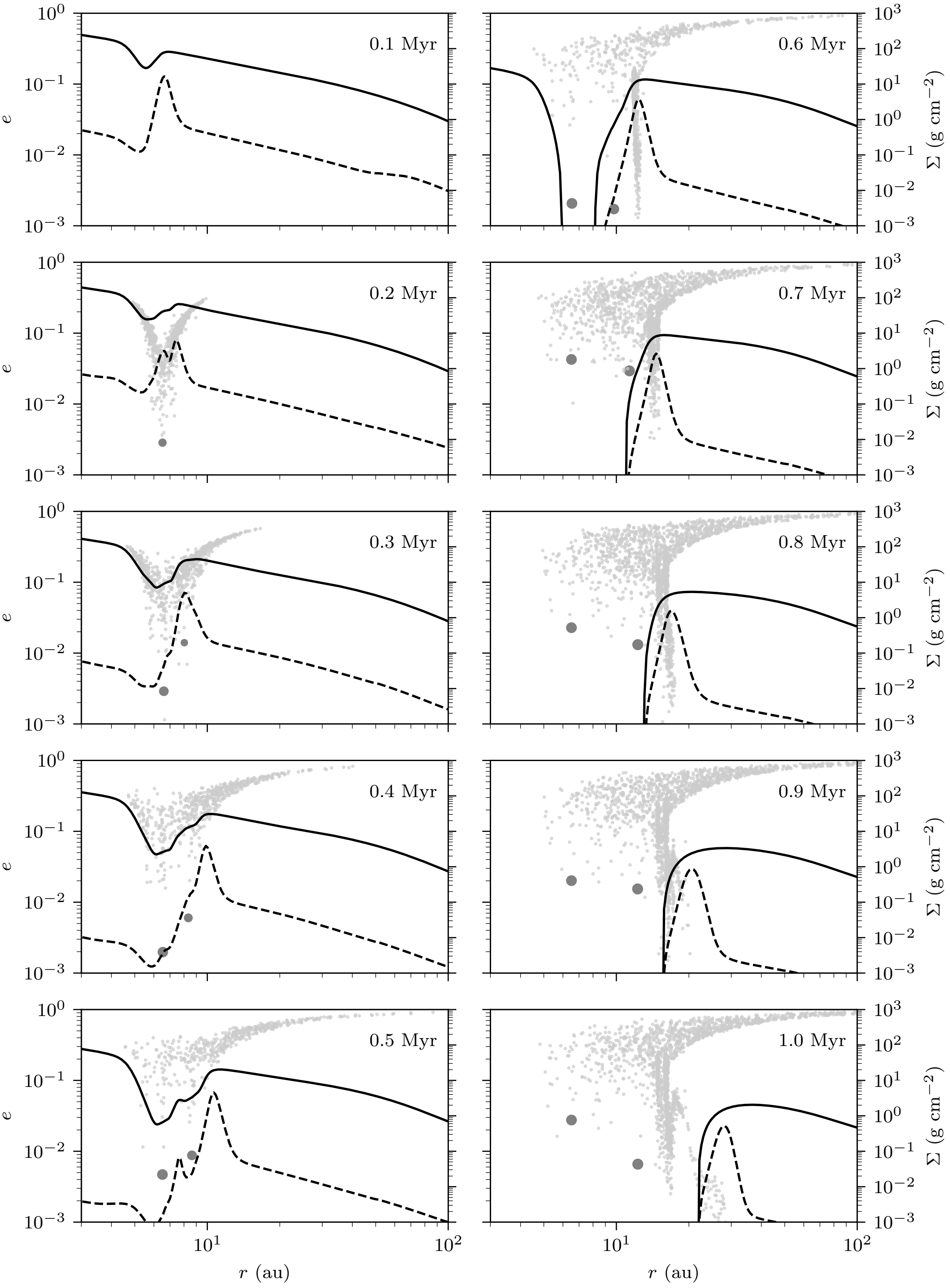

Figure 6.1: Time sequence of the simulation described in Sect. 6.2.3. The eccentricity e and the semimajor axis r of the massive particles are shown by the grey dots for those less than an Earth-mass and, otherwise, by the dark-grey circles with the radius proportional to the cube root of the mass. The gas and dust surface densities are shown by the solid and dashed lines respectively. The results are further described in the text.

Myr, planetesimals have been formed and a massive core has quickly formed through pebble accretion at about 6.5 au and started gas accretion. Due to the gravitational interactions, the smaller planetesimals are being scattered from their initial locations. At 0.3 Myr, a second core has formed at about 8 au as its eccentricity is damped by the disc and pebble accretion resumes. Next, at 0.4 Myr, the first planet has just entered the runaway gas accretion phase and opened a significant gap in the disc. The second planet has also perturbed the disc and the dust-rich region moved further outwards, which allowed gas accretion to start. At 0.5 Myr, the second planet has also entered the runaway gas accretion phase.

A cavity started to open between 6 to 8 au in the disc at 0.6 Myr, this cleared the gas around the first planet and stopped its growth at about 80 $M_{\oplus}$. Meanwhile, planetesimal formation started again outside of the second planet at about 12 au. Their growth by pebble accretion was inefficient due to the dynamical heating so massive cores could not form. At 0.7 Myr, the inner disc was depleted and the second planet has been migrating outwards due the moving edge of the disc and planetesimal formation continued further outside of it. At 0.8 Myr, the cavity continued to grow and the second planet stopped at about 12 au as migration slowed down with the dispersing gas. It has reached the mass of about 90 $M_{\oplus}$ due to the longer duration in the gas. A clear gap in the planetesimal belt is formed at about 15 au, which is also near the location of 4:3 commensurability in orbital period with the outer planet. From 0.9 to 1 Myr, a small number of planetesimals continued to form as the cavity was expanding. Although the eccentricities of them gradually became lower, the dust surface density was also too low for efficient pebble accretion.

6.4 Discussions

6.4.1 Formation

Prior to the opening of the cavity, internal photoevaporation had little effect on the disc. During this period, the formation of the planets generally agrees with the results of rapid formation of planets from the initial pressure bump as presented in the previous chapters. Meanwhile, the growth rate in the runaway gas accretion phase is slower compared to that in Lau et al. (2024a) (Chapter 5). As a results, the pair of planets only reached approximately the mass of Saturn when the cavity opens.

Due to the strong X-ray luminosity of the star, a cavity started to open at 0.6 Myr and a second generation of planet could not form. The planetesimals formed at the cavity edge were either too close to the planet or formed when the dust surface density is low. This scenario provide a pathway that planetesimals were formed due to an enhanced dust-to-gas ratio, while the actual dust surface density cannot provide a large pebble flux. Also, once a cavity is opened, it expands on the timescale of 10^5 years. This also terminates the pebble flux for the newly formed planetesimals.

6.4.2 Architecture

As the cavity was expanding, the outer planet experienced an episode of outward migration. As the migration timescales was lengthening due to the decreasing gas density, the planet's migration stopped when it is slower than the expansion of the cavity and the planet is left in the cavity. Furthermore, the rest of the planetesimals formed from the initial pressure bump are strongly scattered by the planets, while some planetesimals remained near the planets. There is a distinct class of planetesimals formed when the cavity edge has moved further from the planets at about 20 au, where they are dynamically colder. However, the simulated time is too short for the long-term evolution on the Gyr timescale of the small bodies in the system. Longer simulations are required to study if a two-stage formation of the small-bodies can explain the different classes in the Solar System's Kuiper belt.

6.5 Summary and outlook

The preliminary results show a promising pathway to form planetesimals where the subsequent growth is prohibited, which can support the claim that the cold classicals in the Kuiper belt are direct product of planetesimal formation. Also, the results show at least two classes of small bodies due to different formation history. This can provide a possible explanation for the diversity of the Kuiper belt objects. Meanwhile, only one set of parameters is adopted and further investigations are required for a general picture for of final stage of planet formation.

6.5.1 Parameter space

A large X-ray luminosity was chosen for the purpose of testing the internal photoevaporation component. Due to the early dispersal of the disc and fewer massive planets in the simulation, the computational cost is much cheaper. Meanwhile, it is noted that this is near the lower end of the typical disc life time. Therefore, the adopted value of 10^{30} erg s^{-1} for the X-ray luminosity should the upper end of the parameter space. On the other hand, recent work by Sellek et al. (2022) has suggested that there are discrepancies among the prevailing photoevaporation models. They demonstrated the crucial role of the adopted X-ray spectrum. Therefore, the adopted value would be specific to the model by Picogna et al. (2019).

The planets formed from the initial pressure bump are of Saturn mass, which is mostly determined by the envelope opacity and the lifetime of the disc. For Solar System-like gas giants, the adopted value is likely near the appropriate range and a parameter study should be conducted around this value.

For the small bodies, the primordial Kuiper belt has been suggested to end at about 30 to 40 au. Furthermore, dust can drift inwards far from the outer disc. Therefore, the adopted initial characteristic disc size of 50 au is likely the lower end to reproduce the Kuiper belt.

Finally, after the planetary system is formed, a long-term N-body simulation can further show the subsequent dynamical evolution. This is required in attempting to explain the present architecture of the outer Solar System.

Chapter 7

Summary and Outlook

In the traditional N-body planet formation models, similar to the one presented in Chapter 3, the protoplanetary disc is typically assumed to be smooth and dust evolution is not modelled in detail. With the planetesimals as a part of the initial conditions, such setup cannot consistently model the locations of planetesimal formation in the disc. And, planetary cores in a smooth disc are shown to experience significant inward migration forming hot Jupiters instead of Solar-System like giant planets. This assumption of an initial planetesimal disc also contradicts the observations of meteorite dating that planetesimals formation spanned over millions of years in the Solar System.

Motivated by the recent observations of dust rings in protoplanet discs, Chapter 4 presented a model that consider a disc with an initial substructure as well as the evolution of dust in the disc. The key planet formation processes are also included as in the prevailing planet formation models. This permits the modelling of the location and the time of planetesimal formation. In this case, planetary cores are formed at the pressure bump as the enhanced dust surface density favours both the formation of planetesimals and the growth by pebble accretion. This also provides a solution to the migration problem that cores are retained at the zero-torque location resulted from the change in the slope of the surface density.

As a continuation, Chapter 5 presented an additional component of the model that allows gas accretion and planetary gap opening for massive planets. The results showed that two giant planets can form from the initial pressure bump. And, at the outer edge of the planetary gap, dust is accumulated and the next generation of planetesimal formation can occur. The late formation of the second generation of planetary cores limits the time allowed for gas accretion. This presents the scenario of sequential planet formation and provides a possible pathway to form the Solar System's giant planets.

To terminate planet formation physically, Chapter 6 presented the new internal photoevaporation component of the model. The preliminary results further show a case that planetesimal formation can be triggered by disc dispersal and significant growth by pebble accretion is prevented. While a complete parameter study is required, this shows a promising pathway to explain the formation of the Solar System's Kuiper belt as the final stage of the evolution of the protoplanetary disc.

Through the course of the development of the presented planet formation model, the interplay of different planet formation processes is shown to be critical to the final architecture of the planetary systems. Meanwhile, there are various components of the model that merit further investigations.

7.1 Future works

7.1.1 The initial substructure

The presented works focused on the consequences of an initial pressure bump that can trigger planetesimal formation. However, the required size and amplitude of the pressure bump is not studied, which likely also depends on the local disc condition. In particular, the water ice line in the early Solar System has been suggested to be a critical location for planet formation by multiple works (e.g. Morbidelli et al. 2016, 2022; Brasser & Mojzsis 2020; Charnoz et al. 2021; Chambers 2023) while detailed modelling on planetesimal formation at the water ice line has been studied, for example, by Drążkowska & Alibert (2017) and Lichtenberg et al. (2021). This formation mechanism implies that pebble has been formed and drifting through the water line. A model connecting these two proposals explicitly is required.

On the other hand, the interplay between magneto-hydrodynamical processes and dust evolution has been suggested to induce spontaneous dust traps in the disc (Delage et al. submitted). Test simulations have shown promising results that planetesimals can form from such dust trap and grow rapidly to planetary cores. Further parameter studies shall allow forming a variety of planetary systems.

7.1.2 Code optimisation

Due to the computational cost, the parameter space covered is limited preventing producing a wide range of planetary systems. In particular, the bottleneck lies in modelling the disc especially when multiple gas giants are formed. The time step become limited by the steep slopes of the planetary gaps. This problem is expected to be alleviated when the TriPod algorithm (Pfeil et al. 2024) is implemented for the dust evolution. This shall greatly reduce the amount of computation in simulating the dust evolution.

7.1.3 The inner Solar System

The formation of giant planets in the outer Solar System has been the focus as they are likely the first planets formed. They also have the greatest dynamical influence on the disc and other Solar System bodies. Meanwhile, the terrestrial planets have been suggested to form from a ring of planetesimals (e.g. Lichtenberg et al. 2021; Woo et al. 2023). This scenario can be included in the current model to present a full Solar System model through long-term N-body simulations. With the dust evolution considered, the model can then study if an effective isotopic dichotomy is established in the materials that formed the planets. The formation of the asteroid belt is also possible with this model. On the other hand, it is anticipated that the computation will then be dominated by the N-body gravity among the planetesimals, which may require a GPU-powered N-body code (e.g. GENGA; Grimm & Stadel 2014) or a super particle algorithm (e.g. LIPAD; Levison et al. 2012).

Bibliography

Abod, C. P., Simon, J. B., Li, R., et al. 2019, ApJ, 883, 192
Adachi, I., Hayashi, C., & Nakazawa, K. 1976, PThPh, 56, 1756
Adams, F. C., Lada, C. J., & Shu, F. H. 1987, ApJ, 312, 788
Alexander, R. D., Clarke, C. J., & Pringle, J. E. 2006, Monthly Notices of the Royal Astronomical Society, 369, 229
Andama, G., Ndugu, N., Anguma, S. K., & Jurua, E. 2022, MNRAS, 512, 5278
Andrews, S. M., Huang, J., Pérez, L. M., et al. 2018, ApJL, 869, L41
Armitage, P. J. & Bonnell, I. A. 2002, MNRAS, 330, L11
Artymowicz, P. 1993, ApJ, 419, 155
Bai, X.-N. & Stone, J. M. 2010, ApJ, 722, 1437
Bally, J. & Scoville, N. Z. 1982, ApJ, 255, 497
Barge, P. & Sommeria, J. 1995, A&A;, 295, L1
Bate, M. R., Lubow, S. H., Ogilvie, G. I., & Miller, K. A. 2003, Monthly Notices of the Royal Astronomical Society, 341, 213
Benítez-Llambay, P., Masset, F., Koenigsberger, G., & Szulágyi, J. 2015, Natur, 520, 63
Benítez-Llambay, P. & Pessah, M. E. 2018, ApJ, 855, L28
Birnstiel, T., Dullemond, C. P., & Brauer, F. 2010, A&A, 513, A79
Birnstiel, T., Klahr, H., & Ercolano, B. 2012, A&A, 539, A148
Bitsch, B., Izidoro, A., Johansen, A., et al. 2019, A&A, 623, A88
Bitsch, B., Johansen, A., Lambrechts, M., & Morbidelli, A. 2015a, A&A, 575, A28
Bitsch, B., Lambrechts, M., & Johansen, A. 2015b, A&A, 582
Bitsch, B., Morbidelli, A., Johansen, A., et al. 2018, A&A, 612, A30
Blum, J., Gundlach, B., Krause, M., et al. 2017, MNRAS, 469, S755
Bodenheimer, P. & Pollack, J. B. 1986, Icarus, 67, 391
Boss, A. P. 1997, Sci, 276, 1836
Brasser, R., Matsumura, S., Muto, T., & Ida, S. 2018, ApJL, 864, L8
Brasser, R. & Mojzsis, S. J. 2020, NatAs, 4, 492
Brouwers, M. G., Ormel, C. W., Bonsor, A., & Vazan, A. 2021, A&A, 653
Bryden, G., Lin, D. N. C., & Ida, S. 2000, ApJ, 544, 481
Cameron, A. G. W. 1978, The Moon and the Planets, 18, 5
Carrera, D., Gorti, U., Johansen, A., & Davies, M. B. 2017, ApJ, 839, 16
Carrera, D. & Simon, J. B. 2022, ApJL, 933, L10
Carrera, D., Simon, J. B., Li, R., Kretke, K. A., & Klahr, H. 2021, AJ, 161, 96

Chambers, J. 2021, ApJ, 914, 102

Chambers, J. 2023, ApJ, 944, 127

Charnoz, S., Avice, G., Hyodo, R., Pignatale, F. C., & Chaussidon, M. 2021, A&A, 652, A35

Chatterjee, S. & Tan, J. C. 2013, ApJ, 780, 53

Chrenko, O. & Chametla, R. O. 2023, MNRAS, 524, 2705

Chrenko, O., Chametla, R. O., Nesvorný, D., & Flock, M. 2022, A&A, 666, A63

Cieza, L. A., González-Ruilova, C., Hales, A. S., et al. 2021, MNRAS, 501, 2934

Clarke, C. J. & Pringle, J. E. 1988, MNRAS, 235, 365

Cleeves, L. I., Öberg, K. I., Wilner, D. J., et al. 2016, ApJ, 832, 110

Clement, M. S. & Kaib, N. A. 2017, Icar, 288, 88

Coleman, G. A. L. 2021, MNRAS, 506, 3596

Coleman, G. A. L. & Nelson, R. P. 2014, MNRAS, 445, 479

Coleman, G. A. L. & Nelson, R. P. 2016a, MNRAS, 460, 2779

Coleman, G. A. L. & Nelson, R. P. 2016b, MNRAS, 457, 2480

Cossou, C., Raymond, S. N., Hersant, F., & Pierens, A. 2014, A&A, 569

Cossou, C., Raymond, S. N., & Pierens, A. 2013, A&A, 553, L2

Cresswell, P. & Nelson, R. P. 2008, A&A, 482, 677

Cuzzi, J. N., Dobrovolskis, A. R., & Champney, J. M. 1993, Icar, 106, 102

D'Angelo, G. & Lubow, S. H. 2010, ApJ, 724, 730

Deienno, R., Izidoro, A., Morbidelli, A., et al. 2018, ApJ, 864, 50

Delisle, J.-B. 2017, A&A, 605, A96

Delussu, L., Birnstiel, T., Miotello, A., et al. 2024, A&A, 688, A81

Dipierro, G., Price, D., Laibe, G., et al. 2015, MNRAS, 453, L73

Dobbs-Dixon, I., Li, S. L., & Lin, D. N. C. 2007, ApJ, 660, 791

Dong, R., Li, S., Chiang, E., & Li, H. 2017, ApJ, 843, 127

Drążkowska, J. & Alibert, Y. 2017, A&A, 608, A92

Drążkowska, J., Alibert, Y., & Moore, B. 2016, A&A, 594

Drążkowska, J., Bitsch, B., Lambrechts, M., et al. 2023, in Astronomical Society of the Pacific Conference Series, Vol. 534, Protostars Planets VII, ed. S. Inutsuka, Y. Aikawa, T. Muto, K. Tomida, & M. Tamura, 717

Drążkowska, J., Stammler, S. M., & Birnstiel, T. 2021, A&A, 647, A15

Dubrulle, B., Morfill, G., & Sterzik, M. 1995, Icar, 114, 237

Duffell, P. C. 2020, ApJ, 889, 16

Duffell, P. C., Haiman, Z., MacFadyen, A. I., D'Orazio, D. J., & Farris, B. D. 2014, ApJL, 792, L10

Duffell, P. C. & MacFadyen, A. I. 2013, ApJ, 769, 41

Dullemond, C. P., Birnstiel, T., Huang, J., et al. 2018, ApJ, 869, L46

Dullemond, C. P., Dominik, C., & Natta, A. 2001, ApJ, 560, 957

Dullemond, C. P. & Penzlin, A. B. T. 2018, A&A, 609, A50

Duncan, M. J., Levison, H. F., & Lee, M. H. 1998, AJ, 116, 2067

Dürmann, C. & Kley, W. 2015, A&A, 574, A52

Ercolano, B., Barlow, M. J., & Storey, P. J. 2005, Monthly Notices of the Royal Astronomical Society, 362, 1038

Ercolano, B., Barlow, M. J., Storey, P. J., & Liu, X.-W. 2003, Monthly Notices of the Royal Astronomical Society, 340, 1136
Ercolano, B., Clarke, C. J., & Drake, J. J. 2009, ApJ, 699, 1639
Ercolano, B., Drake, J. J., Raymond, J. C., & Clarke, C. C. 2008a, ApJ, 688, 398
Ercolano, B., Young, P. R., Drake, J. J., & Raymond, J. C. 2008b, ApJS, 175, 534
Eriksson, L. E. J., Mol Lous, M. A. S., Shibata, S., & Helled, R. 2023, MNRAS, 526, 4860
Fendyke, S. M. & Nelson, R. P. 2014, MNRAS, 437, 96
Flock, M., Ruge, J. P., Dzyurkevich, N., et al. 2015, A&A, 574, A68
Fortier, A., Benvenuto, O. G., & Brunini, A. 2007, A&A, 473, 311
Fortier, A., Benvenuto, O. G., & Brunini, A. 2009, A&A, 500, 1249
Franz, R., Picogna, G., Ercolano, B., & Birnstiel, T. 2020, A&A, 635, A53
Fung, J. & Chiang, E. 2016, ApJ, 832, 105
Fung, J., Shi, J.-M., & Chiang, E. 2014, ApJ, 782, 88
Gárate, M., Delage, T. N., Stadler, J., et al. 2021, A&A, 655
Gerbig, K. & Li, R. 2023, ApJ, 949, 81
Goldreich, P. & Tremaine, S. 1979, ApJ, 233, 857
Goldreich, P. & Tremaine, S. 1980, ApJ, 241, 425
Goldreich, P. & Ward, W. R. 1973, ApJ, 183, 1051
Grimm, S. L. & Stadel, J. G. 2014, ApJ, 796, 23
Guilera, O. M., Brunini, A., & Benvenuto, O. G. 2010, A&A, 521, A50
Guilera, O. M., Miller Bertolami, M. M., Masset, F., et al. 2021, MNRAS, 507, 3638
Guilera, O. M., Sándor, Z., Ronco, M. P., Venturini, J., & Bertolami, M. M. M. 2020, A&A, 642, A140
Guillot, T., Ida, S., & Ormel, C. W. 2014, A&A, 572, A72
Gupta, A., Miotello, A., Manara, C. F., et al. 2023, A&A, 670, L8
Güttler, C., Blum, J., Zsom, A., Ormel, C. W., & Dullemond, C. P. 2010, A&A, 513, A56
Hartmann, L., Calvet, N., Gullbring, E., & D'Alessio, P. 1998, ApJ, 495, 385
Hasegawa, Y. & Ida, S. 2013, ApJ, 774, 146
Hasegawa, Y., Okuzumi, S., Flock, M., & Turner, N. J. 2017, ApJ, 845, 31
Hollenbach, D., Johnstone, D., Lizano, S., & Shu, F. 1994, ApJ, 428, 654
Huang, S. & Ormel, C. W. 2023, MNRAS, 522, 828
Ida, S. 1990, Icar, 88, 129
Ida, S., Guillot, T., & Morbidelli, A. 2016, A&A, 591, A72
Ida, S. & Lin, D. N. C. 2004, ApJ, 604, 388
Ida, S. & Makino, J. 1993, Icar, 106, 210
Ida, S., Muto, T., Matsumura, S., & Brasser, R. 2020, MNRAS, 494, 5666
Ida, S., Tanaka, H., Johansen, A., Kanagawa, K. D., & Tanigawa, T. 2018, ApJ, 864, 77
Ikoma, M., Nakazawa, K., & Emori, H. 2000, ApJ, 537, 1013
Jang, H., Liu, B., & Johansen, A. 2022, A&A, 664, A86
Jiang, H. & Ormel, C. W. 2023, MNRAS, 518, 3877
Johansen, A., Klahr, H., & Mee, A. J. 2006, MNRAS, 370, L71
Johansen, A. & Lambrechts, M. 2017, Annu. Rev. Earth Planet. Sci., 45, 359
Johansen, A., Low, M.-M. M., Lacerda, P., & Bizzarro, M. 2015, SciA, 1, e1500109

Johansen, A., Oishi, J. S., Low, M.-M. M., et al. 2007, Natur, 448, 1022

Johansen, A., Ronnet, T., Bizzarro, M., et al. 2021, SciA, 7, eabc0444

Johansen, A. & Youdin, A. 2007, ApJ, 662, 627

Johansen, A., Youdin, A., & Low, M.-M. M. 2009, ApJ, 704, L75

Johansen, A., Youdin, A. N., & Lithwick, Y. 2012, A&A, 537, A125

Kanagawa, K. D., Muto, T., Tanaka, H., et al. 2015a, ApJL, 806, L15

Kanagawa, K. D., Muto, T., Tanaka, H., et al. 2016, Publications of the Astronomical Society of Japan, 68, 43

Kanagawa, K. D., Tanaka, H., Muto, T., & Tanigawa, T. 2017, PASJ, 69

Kanagawa, K. D., Tanaka, H., Muto, T., Tanigawa, T., & Takeuchi, T. 2015b, MNRAS, 448, 994

Kanagawa, K. D., Tanaka, H., & Szuszkiewicz, E. 2018, ApJ, 861, 140

Klahr, H. & Schreiber, A. 2020, ApJ, 901, 54

Klahr, H. & Schreiber, A. 2021, ApJ, 911, 9

Kleine, T., Budde, G., Burkhardt, C., et al. 2020, SSRv, 216, 55

Kleine, T., Steller, T., Burkhardt, C., & Nimmo, F. 2023, Icar, 397, 115519

Kley, W. & Nelson, R. 2012, Annu. Rev. Astron. Astrophys., 50, 211

Kobayashi, H., Ormel, C. W., & Ida, S. 2012, ApJ, 756, 70

Kokubo, E. & Ida, S. 1998, Icar, 131, 171

Kokubo, E. & Ida, S. 2000, Icar, 143, 15

Kokubo, E. & Ida, S. 2002, ApJ, 581, 666

Kretke, K. A. & Levison, H. F. 2014, AJ, 148, 109

Kruijer, T. S., Burkhardt, C., Budde, G., & Kleine, T. 2017, Proc. Natl. Acad. Sci., 114, 6712

Kruijer, T. S., Kleine, T., & Borg, L. E. 2020, NatAs, 4, 32

Kuiper, G. P. 1951, Proc. Natl. Acad. Sci., 37, 1

Lada, C. J. & Wilking, B. A. 1984, ApJ, 287, 610

Lambrechts, M. & Johansen, A. 2012, A&A, 544, A32

Lambrechts, M. & Johansen, A. 2014, A&A, 572, A107

Lambrechts, M., Johansen, A., & Morbidelli, A. 2014, A&A, 572, A35

Lambrechts, M., Lega, E., Nelson, R. P., Crida, A., & Morbidelli, A. 2019, A&A, 630, A82

Lau, T. C. H., Birnstiel, T., Drążkowska, J., & Stammler, S. M. 2024a, A&A, 688, A22

Lau, T. C. H., Drążkowska, J., Stammler, S. M., Birnstiel, T., & Dullemond, C. P. 2022, A&A, 668, A170

Lau, T. C. H. & Lee, M. H. 2023, RNAAS, 7, 74

Lau, T. C. H., Lee, M. H., Brasser, R., & Matsumura, S. 2024b, A&A, 683, A204

Lee, E. J., Chiang, E., & Ormel, C. W. 2014, ApJ, 797, 95

Lenz, C. T., Klahr, H., & Birnstiel, T. 2019, ApJ, 874, 36

Lenz, C. T., Klahr, H., Birnstiel, T., Kretke, K., & Stammler, S. 2020, A&A, 640

Levison, H. F., Duncan, M. J., & Thommes, E. 2012, AJ, 144, 119

Levison, H. F., Kretke, K. A., & Duncan, M. J. 2015, Natur, 524, 322

Li, R., Youdin, A. N., & Simon, J. B. 2019, ApJ, 885, 69

Lichtenberg, T., Drążkowska, J., Schönbächler, M., Golabek, G. J., & Hands, T. O. 2021, Sci, 371, 365

Lin, D. N. C. & Papaloizou, J. 1986, ApJ, 309, 846

Lissauer, J. J. 1987, Icar, 69, 249
Liu, B. & Ormel, C. W. 2018, A&A, 615, A138
Liu, B., Ormel, C. W., & Johansen, A. 2019, A&A, 624, A114
Long, F., Pinilla, P., Herczeg, G. J., et al. 2018, ApJ, 869, 17
Lorek, S. & Johansen, A. 2022, A&A, 666, A108
Lorén-Aguilar, P. & Bate, M. R. 2015, MNRAS, 453, L78
Lubow, S. H. & D'Angelo, G. 2006, ApJ, 641, 526
Luhman, K. L., Allen, P. R., Espaillat, C., Hartmann, L., & Calvet, N. 2009, ApJS, 186, 111
Lüst, R. 1952, ZNatA, 7, 87
Lynden-Bell, D. & Pringle, J. E. 1974, MNRAS, 168, 603
MacDonald, M. G. & Dawson, R. I. 2018, AJ, 156, 228
Masset, F. S. 2017, MNRAS, 472, 4204
Mathis, J. S., Rumpl, W., & Nordsieck, K. H. 1977, ApJ, 217, 425
Matsumura, S., Brasser, R., & Ida, S. 2017, A&A, 607, A67
Matsumura, S., Brasser, R., & Ida, S. 2021, A&A, 650, A116
Miller, E., Marino, S., Stammler, S. M., et al. 2021, MNRAS, 508, 5638
Mizuno, H. 1980, PThPh, 64, 544
Morbidelli, A. 2020, A&A, 638, A1
Morbidelli, A., Baillié, K., Batygin, K., et al. 2022, NatAs, 6, 72
Morbidelli, A., Bitsch, B., Crida, A., et al. 2016, Icar, 267, 368
Morbidelli, A., Levison, H. F., Tsiganis, K., & Gomes, R. 2005, Natur, 435, 462
Muto, T., Takeuchi, T., & Ida, S. 2011, ApJ, 737, 37
Nakagawa, Y., Sekiya, M., & Hayashi, C. 1986, Icarus, 67, 375
Nesvorný, D., Li, R., Youdin, A. N., Simon, J. B., & Grundy, W. M. 2019, NatAs, 3, 808
Ogihara, M., Kunitomo, M., & Hori, Y. 2020, ApJ, 899, 91
Oka, A., Nakamoto, T., & Ida, S. 2011, ApJ, 738, 141
Ormel, C. W. 2017, in Formation, Evolution, and Dynamics of Young Solar Systems (Cham: Springer International Publishing), 197–228
Ormel, C. W. & Cuzzi, J. N. 2007, A&A, 466, 413
Ormel, C. W., Dullemond, C. P., & Spaans, M. 2010, ApJ, 714, L103
Ormel, C. W. & Klahr, H. H. 2010, A&A, 520, A43
Ormel, C. W. & Kobayashi, H. 2012, ApJ, 747, 115
Ormel, C. W. & Liu, B. 2018, A&A, 615, A178
Ormel, C. W., Vazan, A., & Brouwers, M. G. 2021, A&A, 647, A175
Owen, J. E., Ercolano, B., & Clarke, C. J. 2011, MNRAS, 412, 13
Owen, J. E., Ercolano, B., Clarke, C. J., & Alexander, R. D. 2010, MNRAS, 401, 1415
Paardekooper, S.-J., Baruteau, C., Crida, A., & Kley, W. 2010, Monthly Notices of the Royal Astronomical Society, 401, 1950
Paardekooper, S.-J., Baruteau, C., & Kley, W. 2011, MNRAS, 410, 293
Paardekooper, S.-J. & Papaloizou, J. C. B. 2008, A&A, 485, 877
Pfeil, T., Birnstiel, T., & Klahr, H. 2024, A&A
Picogna, G., Ercolano, B., Owen, J. E., & Weber, M. L. 2019, MNRAS, 487, 691
Pinilla, P., Benisty, M., & Birnstiel, T. 2012, A&A, 545, A81

Pinilla, P., Flock, M., Ovelar, M. d. J., & Birnstiel, T. 2016, A&A, 596, A81

Piso, A.-M. A. & Youdin, A. N. 2014, ApJ, 786, 21

Pollack, J. B., Hubickyj, O., Bodenheimer, P., et al. 1996, Icar, 124, 62

Pringle, J. E. 1981, ARA&A;, 19, 137

Pritchard, M., Meru, F., Rowther, S., Armstrong, D., & Randall, K. 2024, MNRAS, 528, 6538

Rafikov, R. R. 2016, ApJ, 831, 122

Raorane, A., Brasser, R., Matsumura, S., et al. 2024, Icarus, 116231

Rice, W. K. M., Armitage, P. J., Wood, K., & Lodato, G. 2006, MNRAS, 373, 1619

Rucska, J. J. & Wadsley, J. W. 2020, MNRAS, 500, 520

Saito, E. & Sirono, S.-i. 2011, ApJ, 728, 20

Sándor, Z. & Regály, Z. 2021, MNRAS, 503, L67

Schäfer, U., Yang, C.-C., & Johansen, A. 2017, A&A, 597, A69

Schoonenberg, D., Ormel, C. W., & Krijt, S. 2018, A&A, 620

Schräpler, R. & Blum, J. 2011, ApJ, 734, 108

Schreiber, A. & Klahr, H. 2018, ApJ, 861, 47

Schulik, M., Johansen, A., Bitsch, B., & Lega, E. 2019, A&A, 632, A118

Seager, S., Kuchner, M., Hier-Majumder, C. A., & Militzer, B. 2007, ApJ, 669, 1279

Sellek, A. D., Clarke, C. J., & Ercolano, B. 2022, Monthly Notices of the Royal Astronomical Society, 514, 535

Shakura, N. I. & Sunyaev, R. A. 1973, A\&A, 24, 337

Shu, F. H., Johnstone, D., & Hollenbach, D. 1993, Icarus, 106, 92

Simon, J. B., Armitage, P. J., Li, R., & Youdin, A. N. 2016, ApJ, 822, 55

Simon, J. B., Armitage, P. J., Youdin, A. N., & Li, R. 2017, ApJ, 847, L12

Squire, J. & Hopkins, P. F. 2020, MNRAS, 498, 1239

Stammler, S. M. & Birnstiel, T. 2022, ApJ, 935, 35

Stammler, S. M., Drążkowska, J., Birnstiel, T., et al. 2019, ApJ, 884, L5

Stammler, S. M., Lichtenberg, T., Drążkowska, J., & Birnstiel, T. 2023, A&A, 670, L5

Szulágyi, J., Masset, F., Lega, E., et al. 2016, MNRAS, 460, 2853

Takahashi, S. Z. & Inutsuka, S.-i. 2014, ApJ, 794, 55

Tamayo, D., Rein, H., Petrovich, C., & Murray, N. 2017, ApJL, 840, L19

Tanaka, H., Takeuchi, T., & Ward, W. R. 2002, ApJ, 565, 1257

Tanaka, H. & Ward, W. R. 2004, ApJ, 602, 388

Tanga, P., Babiano, A., Dubrulle, B., & Provenzale, A. 1996, Icar, 121, 158

Tanigawa, T. & Tanaka, H. 2016, ApJ, 823, 48

Tanigawa, T. & Watanabe, S.-i. 2002, ApJ, 580, 506

Teague, R., Bae, J., Bergin, E. A., Birnstiel, T., & Foreman-Mackey, D. 2018a, ApJ, 860, L12

Teague, R., Bae, J., Birnstiel, T., & Bergin, E. A. 2018b, ApJ, 868, 113

Terquem, C. & Papaloizou, J. C. B. 2007, ApJ, 654, 1110

Testi, L., Natta, A., Shepherd, D. S., & Wilner, D. J. 2003, A&A, 403, 323

Toci, C., Rosotti, G., Lodato, G., Testi, L., & Trapman, L. 2021, MNRAS, 507, 818

Trilling, D. E., Benz, W., Guillot, T., et al. 1998, ApJ, 500, 428

Tsiganis, K., Gomes, R., Morbidelli, A., & Levison, H. F. 2005, Natur, 435, 459

Visser, R. G. & Ormel, C. W. 2016, A&A, 586, A66

Voelkel, O., Klahr, H., Mordasini, C., Emsenhuber, A., & Lenz, C. 2020, A&A, 642, A75
Wada, K., Tanaka, H., Okuzumi, S., et al. 2013, A&A, 559, A62
Ward, W. R. 1997, Icarus, 126, 261
Weidenschilling, S. J. 1977, MNRAS, 180, 57
Whipple, F. L. 1972, in Plasma Planet, ed. A. Elvius, 211
Wilner, D. J., D'Alessio, P., Calvet, N., Claussen, M. J., & Hartmann, L. 2005, ApJ, 626, L109
Wong, K. H. & Lee, M. H. 2024, AJ, 167, 112
Woo, J. M. Y., Morbidelli, A., Grimm, S. L., Stadel, J., & Brasser, R. 2023, Icarus, 396, 115497
Wurm, G., Paraskov, G., & Krauss, O. 2005, Phys. Rev. E, 71, 021304
Xu, W. & Wang, S. 2024, ApJL, 962, L4
Youdin, A. N. & Goodman, J. 2005, ApJ, 620, 459
Youdin, A. N. & Lithwick, Y. 2007, Icar, 192, 588
Zhu, Z., Dong, R., Stone, J. M., & Rafikov, R. R. 2015, ApJ, 813, 88
Zormpas, A., Birnstiel, T., Rosotti, G. P., & Andrews, S. M. 2022, A&A, 661, A66
Zsom, A., Ormel, C. W., Güttler, C., Blum, J., & Dullemond, C. P. 2010, A&A, 513, A57

Acknowledgments

I would extend my gratitude to Prof. Dr Til Birnstiel for his expert guidance throughout this journey of science. Together with Dr Joanna Drążkowska and Dr Sebastian Stammler, our close collaborations have been enjoyable and intellectually stimulating. I look forward to continue working with them.

I must also thank Michael Yeung, Lilian Lee, Luca Delussu, Giovanni Tedeschi, Vignesh Vaikundaraman, Ho Wan Cheng, Emily Wong, Christiane Göppl, Elena Hoemann, Dr Jan-Vincent Harre, Dr Fabian Binkert, Dr Timmy Delage, Dr Thomas Pfeil, Dr Kristina Monsch and Dr Michael Weber as my peers in this journey. A special thanks goes to David Arias for proof reading the thesis from an external point of view.